PHYSICAL REVIEW D **96,** 014011 (2017)

Parton distribution functions, α_s, and heavy-quark masses for LHC Run II

S. Alekhin,[1,2] J. Blümlein,[3] S. Moch,[1] and R. Plačakytė[1]
[1] *II. Institut für Theoretische Physik, Universität Hamburg Luruper Chaussee 149, D–22761 Hamburg, Germany*
[2] *Institute for High Energy Physics, 142281 Protvino, Moscow region, Russia*
[3] *Deutsches Elektronensynchrotron DESY, Platanenallee 6, D–15738 Zeuthen, Germany*

(Received 31 January 2017; published 18 July 2017)

We determine a new set of parton distribution functions (ABMP16), the strong coupling constant α_s and the quark masses m_c, m_b and m_t in a global fit to next-to-next-to-leading order (NNLO) in QCD. The analysis uses the $\overline{\mathrm{MS}}$ scheme for α_s and all quark masses and is performed in the fixed-flavor number scheme for $n_f = 3, 4, 5$. Essential new elements of the fit are the combined data from HERA for inclusive deep-inelastic scattering (DIS), data from the fixed-target experiments NOMAD and CHORUS for neutrino-induced DIS, data from Tevatron and the LHC for the Drell-Yan process and the hadro-production of single-top and top-quark pairs. The theory predictions include new improved approximations at NNLO for the production of heavy quarks in DIS and for the hadro-production of single-top quarks. The description of higher twist effects relevant beyond the leading twist collinear factorization approximation is refined. At NNLO, we obtain the value $\alpha_s^{(n_f=5)}(M_Z) = 0.1147 \pm 0.0008$.

DOI: 10.1103/PhysRevD.96.014011

I. INTRODUCTION

Parton distribution functions (PDFs) are indispensable for theory predictions of scattering processes at hadron colliders. Within standard factorization in quantum chromodynamics (QCD), the PDFs are determined by a comparison of theoretical predictions with hard-scattering data covering a broad range of kinematics in the Bjorken variable x and the momentum scale Q^2. Steady progress both in the accumulation and in the analysis of hard-scattering data by experiments at HERA, Tevatron and the Large Hadron Collider (LHC) as well as improvements of the relevant theoretical predictions to next-to-next-to-leading order (NNLO) in perturbative QCD allows for an accurate description of the parton content of the proton in global fits. Such fits provide the proton composition in terms of the gluon and the individual light-quark flavors u, d and s with a good precision. Simultaneously, they are also able to determine the strong coupling constant α_s and the heavy-quark masses m_c, m_b and m_t to NNLO in QCD. These results serve as input to high precision predictions for benchmark processes in the Standard Model (SM) and cross sections for scattering reactions beyond the SM, measured or being searched for in run II of the LHC.

PDF extractions have been carried out by us in the past, with ABM12 [1] being our previous global fit. The present analysis has evolved out of these efforts and results in the new ABMP16 set. It incorporates a number of intermediate updates [2,3], in particular the ABMP15 [3] fit. Moreover, it makes use of improvements in the theoretical description of the hard-scattering processes for the production of heavy quarks in deep-inelastic scattering (DIS) and for the hadro-production of single-top quarks. However, the primary motivation for ABMP16 comes from the wealth of recently published new data for the measurements of electron-induced DIS from HERA [4] as well as W- and Z-boson production at Tevatron and the LHC. These data have great potential to further constrain light-quark PDFs at large and small values of x, to pin down the gluon PDF and to consolidate determinations of α_s using various sets of DIS data published during the last three decades.

In our analysis, the PDFs and all QCD parameters which are often correlated with the PDFs, i.e., $\alpha_s(M_Z)$ and the heavy-quark masses $m_c(m_c)$, $m_b(m_b)$ and $m_t(m_t)$, are determined in the $\overline{\mathrm{MS}}$ scheme with the number of flavors fixed, $n_f = 3, 4, 5$; see, e.g., [5]. The theoretical accuracy is strictly NNLO in QCD. Other PDF sets currently available are CJ15 [6], CT14 [7], HERAPDF2.0 [4], JR14 [8], MMHT14 [9], and NNPDF3.0 [10], all of them accurate to NNLO in QCD except for CJ15, which has limited the precision to next-to-leading order (NLO). None of these PDFs uses all of the latest data considered in the current ABMP16 analysis. A recent benchmarking of those PDFs performed in [11] has shown that differences in the theoretical predictions obtained by using various PDFs are a consequence of specific theory assumptions or underlying physics models used in the fits of some of these PDFs. Therefore, it is essential to provide a detailed account of the theoretical framework used in the PDF analyses.

The paper is organized as follows. We present in Sec. II the set-up of the analysis. In particular, we discuss the various sets of hard-scattering data and their kinematic range in Sec. II A. The improvements in the theory description are given in Sec. II B and include new approximate NNLO QCD predictions for heavy-quark DIS and for single-top quark hadro-production as well as a refined treatment of the higher twist effects. The results for the ABMP16 PDFs are discussed in Sec. III where the quality of the data description is documented, the improvements in the PDFs are discussed and a detailed comparison with the ABM12 fit and other sets is provided. Correlations of the various fit parameters are discussed and particular attention is paid to the value of the strong coupling constant α_s extracted from the global fit and individually from various sets of DIS data. The sensitivity of the value of α_s to higher twist terms for all sets of DIS data is quantified. Furthermore, we report our results on the $\overline{\mathrm{MS}}$ heavy-quark masses $m_c(m_c)$, $m_b(m_b)$ and $m_t(m_t)$ and compare with other determinations. Finally, in Sec. IV we present several applications. We compare the second Mellin moment of the nonsinglet quark PDFs to recent lattice measurements and we provide cross-section predictions with the ABMP16 PDFs for relevant LHC processes, such as Higgs boson production in gluon-gluon-fusion and hadro-production of top-quark pairs. In addition, with the measured values of the strong coupling constant α_s and the top-quark mass $m_t(m_t)$ as input we can solve the renormalization group equations for all SM couplings including the scalar self-coupling λ of the SM Higgs boson. This allows us to study the running of λ and to assess whether new physics needs to be invoked in order to stabilize the electroweak vacuum at high scales [12,13]. We also discuss the features of the data grids for the fit results in the format of `LHAPDF` library (version 6) [14] and conclude in Sec. V.

II. SET-UP OF THE ANALYSIS

A. Data

The data used in present analysis have been updated in an essential manner with respect to the ones used in our earlier fits ABM12 [1] and ABMP15 [3]. The changes concern inclusive DIS data as well as data on DIS charm- and bottom-quark production, on the Drell-Yan (DY) process, and on the top-quark hadro-production as follows:

(i) The HERA run I inclusive cross-section data on the neutral-current (NC) and charged-current (CC) $e^\pm p$ DIS have been replaced with the final combination of the run I + II results [4]. This input provides improved constraints on the small-x gluon and sea-quark PDFs and significant benefits for the separation of the up- and down-quark PDFs by virtue of the precise CC data.

(ii) The data on production of bottom quark in $e^\pm p$ DIS obtained by the H1 [15] and ZEUS [16] Collaborations are added. These data are particularly useful for the determination of the bottom-quark mass and are also sensitive to the small-x PDFs.

(iii) New data on the charm-quark production in CC neutrino-nucleon DIS collected by the NOMAD [17] and CHORUS [18] experiments are added in order to improve the strange sea determination, cf. Ref. [3] for details.

(iv) The latest data on $W^\pm$- and Z-boson production from LHC and Tevatron are added in order to provide an improved determination of the light-quark PDFs over a wide range of the parton momentum fractions x and to disentangle distributions for quarks and anti-quarks. The data include rapidity distributions for $W^\pm$- and Z-boson production in the forward region at the collision energies of $\sqrt{s} = 7$ and 8 TeV obtained by LHCb [19–21], DØ data on the electron charge asymmetry, which also probes forward kinematics [22], DØ data on the muon charge asymmetry in the central region [23], new CMS rapidity distributions for the $W^\pm$-boson recorded at $\sqrt{s} = 7$ and 8 TeV using the muon decay channel [24,25] and the cross section of $W^\pm$- and Z-boson production at $\sqrt{s} = 13$ TeV in the fiducial volume obtained by ATLAS [26].

(v) A collection of the recent t-quark data from the LHC [27–52] and Tevatron [53] added to the present analysis provides additional constraints on the gluon PDF and allows to perform a consistent determination of the top-quark mass with full account of its correlations with the gluon PDF and the strong coupling α_s.

With the new measurements included in the present study, the theoretical framework has been updated correspondingly to account for the best possible precision and consistency of the PDF fit as discussed in Sec II B. In the following, the DIS, DY, and heavy-quark production data sets used in our fit are described in detail.

1. Inclusive DIS

The recent HERA inclusive NC and CC DIS data set [4] includes a combination of all published H1 and ZEUS measurements performed in the runs I and II of the HERA collider. The data were collected at the proton beam energies $E_p = 920$, 820, 575 and 460 GeV which correspond to the center-of-mass energies $\sqrt{s} = 320$, 300, 251 and 225 GeV, respectively. The combined HERA data [4] cover the range of momentum transfer squared Q^2 up to 50000 GeV^2 and are the most precise measurements of ep DIS over that wide kinematic range. The high-statistics HERA II data used in the new combination improve the accuracy at high Q^2, as compared to the HERA I inclusive combination, in particular for the NC e^-p and the CC e^+p (e^-p) data. The latter impose improved constraints on the valence down-(up-)quark distributions in the proton and in combination with the new DY collider data added to our fit they allow to avoid using the fixed-target DIS data [54–60] collected by the SLAC, BCDMS, and NMC experiments with a deuteron target. Previously, those samples have been employed in the ABM12 fit and our earlier analyses in order to constrain the down-quark distributions at the expense of having to deal also with nuclear effects. Now, with the extended DIS and DY input the experimental uncertainties in the down-quark PDFs do not deteriorate as compared to the ABM12 PDFs even in the absence of deuteron data, while any additional uncertainty caused by the modeling of nuclear effects has been eliminated.

The unprecedented precision achieved for the HERA run $\mathrm{I}+\mathrm{II}$ data facilitates an accurate calibration of the earlier fixed-target DIS experiments' normalization. Therefore, we introduce a normalization factor for each remaining fixed-target data set, SLAC, NMC and BCDMS, and fit these factors simultaneously with the PDF parameters. The fitted values of normalization factors are determined with an uncertainty of $\mathcal{O}(1\%)$, cf. Table I. Such a reevaluation of the normalization is entirely justified for the SLAC and NMC experiments, as it was determined in those experiments in a similar way, using, however, less accurate data sets for calibration. It is also relevant for the BCDMS data [61], which were not subject to an additional re-normalization in our earlier ABM12 and ABMP15 fits based on the HERA I data. Indeed, the BCDMS normalization uncertainty determined in present analysis is much smaller than the one of 3% provided by BCDMS itself. In general, the normalization factors obtained in the present analysis are comparable to unity within the normalization uncertainties quoted by respective experiment. However, for the SLAC-E89a experiment [55] the normalization factor deviates from unity by $\sim 5\%$. Besides, the data description quality achieved for the SLAC-E89a data is significantly worse than for other SLAC experiments. It is also worth noting that the SLAC-89a experiment is kinematically separated from other SLAC measurements. Therefore, having no possibility to clarify the issue of its normalization, we do not use SLAC-E89a data in the final version of the present analysis.

2. DIS charm- and bottom-quark production

In addition to the HERA inclusive combination [4], we include into the fit the semi-inclusive HERA data on NC DIS charm-quark production obtained by a combination of the corresponding H1 and ZEUS results [63]. Those data provide a complementary constraint on the low-x gluon and sea-quark distributions, cf. Ref. [63], and have already been employed in our earlier ABM12 and ABMP15 analyses.

TABLE I. The values of fitted normalization factors for the fixed-target DIS data sets used in the present analysis with the uncertainties quoted in parentheses.

Experiment	Process	Beam energy (GeV)	Reference	Normalization
SLAC-49a	$ep \to eX$	$7 \div 20$	[54,62]	1.001(11)
SLAC-49b	$ep \to eX$	$4.5 \div 18$	[54,62]	1.010(15)
SLAC-87	$ep \to eX$	$8.7 \div 20$	[54,62]	1.012(11)
SLAC-89b	$ep \to eX$	$6.5 \div 19.5$	[56,62]	1.000(11)
BCDMS	$\mu p \to \mu X$	$100 \div 280$	[61]	0.976(7)
NMC	$\mu p \to \mu X$	90	[60]	0.993(13)
		120		1.011(12)
		200		1.022(12)
		280		1.012(12)

The CC DIS charm-quark production, which is mostly relevant for disentangling the strange sea distribution, is routinely measured by detecting di-muons produced in neutrino-nucleon interaction. Two data sets of such kind, obtained by the CCFR and NuTeV experiments [64], were used in our earlier ABM12 and ABMP15 fits. For the present analysis we add the recent precision measurement of di-muon production in ν-Fe DIS performed by the NOMAD experiment [17], which allows to improve the strange sea determination at large x, cf. Ref. [2]. One more new measurement of the CC charm-quark production was performed by the CHORUS Collaboration [18] using an emulsion target. As a benefit of this technique, the charmed hadrons are detected directly by their hadronic decays, therefore the CHORUS data are less sensitive to the details of the charm fragmentation modeling. Likewise, the data on the charmed-hadron production rates from the emulsion experiment FNAL-532 [65] help to constrain the charmed-hadron semileptonic branching ratio, which is required for the analysis of the CCFR, NuTeV, and NOMAD di-muon data, cf. Ref. [2].

Finally, the bottom-quark DIS production cross sections measured by the H1 [15] and ZEUS [16] collaborations are also included into the present analysis. This allows to determine the value of the bottom-quark mass.

3. Drell-Yan process

The data on the hadro-production of $W^{\pm}$- and Z-bosons and the DIS data sets discussed above are mutually complementary in the context of disentangling the light-quark PDFs. In particular, the high statistics data from LHC and Tevatron on $W^{\pm}$-production in the forward region allow to improve the determination of the up- and down-quark distributions down to $x \sim 10^{-4}$, cf. Ref. [3]. For the present analysis we select the most recent and statistically significant data sets on the $W^{\pm}$- and Z-boson production collected by the ATLAS, CMS, and LHCb experiments at the LHC and the DØ experiment at Fermilab, cf. Table II. The updated analysis of ATLAS data [66] collected at $\sqrt{s} = 7$ TeV was released after completion of our fit. These data are in a good agreement with the predictions based on the ABM12 PDFs and therefore should be smoothly accommodated into a future release.

The data on $W^{\pm}$-production in Table II are given in form of pseudo-rapidity distributions for the decay electron or muon. The DØ data on $W^{\pm}$-distributions obtained by unfolding the charged-lepton ones are also available [70]. Since those data are sensitive to the details of the modeling of the $W^{\pm}$-decay and, in particular, to the PDFs used, they

TABLE II. The list of DIS and DY data used in the current analysis with the collider data listed first. The top-quark production data are detailed in Tables III and IV.

Experiment	Beam (E_b) or center-of-mass energy ($\sqrt{s}$)	$\mathcal{L}$ (1/fb)	Process	Kinematic cuts used in the present analysis (cf. orginal references for notations)	Ref.
			DIS		
HERA I + II	$\sqrt{s} = 0.225 \div 0.32$ TeV	0.5	$e^{\pm}p \rightarrow e^{\pm}X$	$2.5 \leq Q^2 \leq 50000$ GeV^2, $2.5 \times 10^{-5} \leq x \leq 0.65$	[4]
			$e^{\pm}p \rightarrow \overset{(-)}{\nu} X$	$200 \leq Q^2 \leq 50000$ GeV^2, $1.3 \times 10^{-2} \leq x \leq 0.40$	
BCDMS	$E_b = 100 \div 280$ GeV		$\mu^+ p \rightarrow \mu^+ X$	$7 < Q^2 < 230$ GeV^2, $0.07 \leq x \leq 0.75$	[61]
NMC	$E_b = 90 \div 280$ GeV		$\mu^+ p \rightarrow \mu^+ X$	$2.5 \leq Q^2 < 65$ GeV^2, $0.009 \leq x < 0.5$	[60]
SLAC-49a	$E_b = 7 \div 20$ GeV		$e^- p \rightarrow e^- X$	$2.5 \leq Q^2 < 8$ GeV^2, $0.1 < x < 0.8$, $W \geq 1.8$ GeV	[54] [62]
SLAC-49b	$E_b = 4.5 \div 18$ GeV		$e^- p \rightarrow e^- X$	$2.5 \leq Q^2 < 20$ GeV^2, $0.1 < x < 0.9$, $W \geq 1.8$ GeV	[54] [62]
SLAC-87	$E_b = 8.7 \div 20$ GeV		$e^- p \rightarrow e^- X$	$2.5 \leq Q^2 < 20$ GeV^2, $0.3 < x < 0.9$, $W \geq 1.8$ GeV	[54] [62]
SLAC-89b	$E_b = 6.5 \div 19.5$ GeV		$e^- p \rightarrow e^- X$	$2.5 \leq Q^2 \leq 19$ GeV^2, $0.17 < x < 0.9$, $W \geq 1.8$ GeV	[56] [62]
			DIS heavy-quark production		
HERA I + II	$\sqrt{s} = 0.32$ TeV		$e^{\pm}p \rightarrow e^{\pm}cX$	$2.5 \leq Q^2 \leq 2000$ GeV^2, $2.5 \times 10^{-5} \leq x \leq 0.05$	[63]
H1	$\sqrt{s} = 0.32$ TeV	0.189	$e^{\pm}p \rightarrow e^{\pm}bX$	$5 \leq Q^2 \leq 2000$ GeV^2, $2 \times 10^{-4} \leq x \leq 0.05$	[15]
ZEUS	$\sqrt{s} = 0.32$ TeV	0.354	$e^{\pm}p \rightarrow e^{\pm}bX$	$6.5 \leq Q^2 \leq 600$ GeV^2, $1.5 \times 10^{-4} \leq x \leq 0.035$	[16]
CCFR	$87 \lesssim E_b \lesssim 333$ GeV		$\overset{(-)}{\nu} N \rightarrow \mu^{\pm}cX$	$1 \leq Q^2 < 170$ GeV^2, $0.015 \leq x \leq 0.33$	[64]
CHORUS	$\langle E_b \rangle \approx 27$ GeV		$\nu N \rightarrow \mu^+ cX$		[18]
NOMAD	$6 \leq E_b \leq 300$ GeV		$\nu N \rightarrow \mu^+ cX$	$1 \leq Q^2 < 20$ GeV^2, $0.02 \lesssim x \leq 0.75$	[17]
NuTeV	$79 \lesssim E_b \lesssim 245$ GeV		$\overset{(-)}{\nu} N \rightarrow \mu^{\pm}cX$	$1 \leq Q^2 < 120$ GeV^2, $0.015 \leq x \leq 0.33$	[64]
			DY		
ATLAS	$\sqrt{s} = 7$ TeV	0.035	$pp \rightarrow W^{\pm}X \rightarrow l^{\pm}\nu X$	$p_T^l > 20$ GeV, $p_T^{\nu} > 25$ GeV, $m_T > 40$ GeV	[67]
			$pp \rightarrow ZX \rightarrow l^+l^-X$	$p_T^l > 20$ GeV, $66 < m_{ll} < 116$ GeV	
	$\sqrt{s} = 13$ TeV	0.081	$pp \rightarrow W^{\pm}X \rightarrow l^{\pm}\nu X$	$p_T^{\nu} > 25$ GeV, $m_T > 50$ GeV	[26]
			$pp \rightarrow ZX \rightarrow l^+l^-X$	$p_T^l > 25$ GeV, $66 < m_{ll} < 116$ GeV	
CMS	$\sqrt{s} = 7$ TeV	4.7	$pp \rightarrow W^{\pm}X \rightarrow \mu^{\pm}\nu X$	$p_T^{\mu} > 25$ GeV	[24]
	$\sqrt{s} = 8$ TeV	18.8	$pp \rightarrow W^{\pm}X \rightarrow \mu^{\pm}\nu X$	$p_T^{\mu} > 25$ GeV	[25]
DØ	$\sqrt{s} = 1.96$ TeV	7.3	$\bar{p}p \rightarrow W^{\pm}X \rightarrow \mu^{\pm}\nu X$	$p_T^{\mu} > 25$ GeV, $\not{E}_T > 25$ GeV	[23]
		9.7	$\bar{p}p \rightarrow W^{\pm}X \rightarrow e^{\pm}\nu X$	$p_T^{e} > 25$ GeV, $\not{E}_T > 25$ GeV	[22]
LHCb	$\sqrt{s} = 7$ TeV	1	$pp \rightarrow W^{\pm}X \rightarrow \mu^{\pm}\nu X$	$p_T^{\mu} > 20$ GeV	[19]
			$pp \rightarrow ZX \rightarrow \mu^+\mu^-X$	$p_T^{\mu} > 20$ GeV, $60 < m_{\mu\mu} < 120$ GeV	
	$\sqrt{s} = 8$ TeV	2	$pp \rightarrow ZX \rightarrow e^+e^-X$	$p_T^{e} > 20$ GeV, $60 < m_{ee} < 120$ GeV	[21]
		2.9	$pp \rightarrow W^{\pm}X \rightarrow \mu^{\pm}\nu X$	$p_T^{\mu} > 20$ GeV	[20]
			$pp \rightarrow ZX \rightarrow \mu^+\mu^-X$	$p_T^{\mu} > 20$ GeV, $60 < m_{\mu\mu} < 120$ GeV	
FNAL-605	$E_b = 800$ GeV		$pCu \rightarrow \mu^+\mu^-X$	$7 \leq M_{\mu\mu} \leq 18$ GeV	[68]
FNAL-866	$E_b = 800$ GeV		$pp \rightarrow \mu^+\mu^-X$ $pD \rightarrow \mu^+\mu^-X$	$4.6 \leq M_{\mu\mu} \leq 12.9$ GeV	[69]

TABLE III. The data on the $t\bar{t}$-production cross section from the LHC used in the present analysis. The errors given are combinations of the statistical and systematic ones. An additional error of 1.4, 3.3, 4.2 and 12 pb due to the beam energy uncertainty applies to all entries for the collision energy of $\sqrt{s} = 5$, 7, 8 and 13 TeV, respectively. The quoted values are rounded for the purpose of a compact presentation.

		Cross section (pb)						
$\sqrt{s}$ (TeV)		5	7		8		13	
Experiment		CMS	ATLAS	CMS	ATLAS	CMS	ATLAS	CMS
Decay mode	dilepton + b-jet(s)		183 ± 6 [36]		243 ± 8 [36]		818 ± 36 [37]	792 ± 43 [38]
	dilepton + jets		181 ± 11 [33]	174 ± 6 [34]		245 ± 9 [34]		746 ± 86 [35]
	lepton + jets			162 ± 14 [39]	260 ± 24 [40]	229 ± 15 [39]		836 ± 133 [41]
	lepton + jets, $b \to \mu\nu X$		165 ± 38 [42]					
	lepton + $\tau \to$ hadrons		183 ± 25 [43]	143 ± 26 [44]		257 ± 25 [51]		
	jets + $\tau \to$ hadrons		194 ± 49 [46]	152 ± 34 [47]				
	all-jets		168 ± 60 [48]	139 ± 28 [49]		276 ± 39 [45]		834^{+123}_{-109} [50]
	eμ	82 ± 23 [52]						

are not included into our analysis in order to avoid a bias due to a mismatch between the PDFs used in the DØ analysis and ours; see also the discussion in Ref. [3].

When available [19–21,25,67], the absolute measurements of the lepton pseudorapidity distributions are used. In other cases [22–24], we employ the lepton charge asymmetries. However, as a cross-check we also compare our predictions with the LHCb [19,20] and CMS [25] data on the lepton charge asymmetry, although the absolute measurements are used in the fit, cf. Sec. III A. The recent ATLAS measurements of the $W^{\pm}$- and Z-boson cross sections in the fiducial volume at $\sqrt{s} = 13$ TeV [26] used in our analysis are separated for the electron- and muon-decay channels taking into account correlations between these measurements. This gives six data points in total for our $\sqrt{s} = 13$ TeV ATLAS data set.

The fixed-target Drell-Yan data provide information on the quark PDFs in the high-x region and allow to separate the sea and valence quark distributions. In the present analysis, two data sets of this kind are employed: the ratio of the proton-proton and proton-deuterium cross sections from the FNAL-866 experiment [69] and the proton-copper data from the FNAL-605 experiment [68]. Both sets have been used in our earlier fits, cf. Ref. [71].

4. Top-quark production

Measurements of top-quark production at the LHC and Tevatron provide a powerful tool for the study of the gluon distribution at large x and of α_s at large renormalization scales. However, due the strong sensitivity to the value of m_t, the accuracy achieved in such a study is essentially limited by the uncertainty in m_t. To take into account this interplay we fit the value of m_t simultaneously with the PDF parameters and α_s, cf. Sec. III. The t-quark data included into the present analysis comprise the $t\bar{t}$-production cross sections measured with various analysis techniques and for different decay modes at the center-of-mass energies $\sqrt{s} = 5$, 7, 8, and 13 TeV by ATLAS and CMS, cf. Table III, and those at $\sqrt{s} = 1.96$ TeV obtained at Tevatron [72]. In addition, single-top production data in the s- and t-channel from Tevatron and in the t-channel from the LHC are considered, cf. Table IV. Single-top production is mediated by the electroweak interactions at leading order and thus not particularly sensitive to α_s and the gluon distribution. Therefore, the latter input dampens the correlation between the gluon PDF, α_s and m_t, which emerges in the analysis of the $t\bar{t}$-data.

Due to specifics of the experimental analyses for the t-quark detection as well as necessary extrapolations in

TABLE IV. The data on single-top production in association with a light quark q or $\bar{b}$-quark from the LHC and Tevatron used in the present analysis. The errors given are combinations of the statistical, systematic, and luminosity ones.

Experiment	ATLAS			CMS			CDF&DØ
$\sqrt{s}$ (TeV)	7	8	13	7	8	13	1.96
Final states	tq	tq	tq	tq	tq	tq	$tq, t\bar{b}$
Reference	[27]	[28]	[29]	[30]	[31]	[32]	[53]
Luminosity (1/fb)	4.59	20.3	3.2	2.73	19.7	2.3	9.7 × 2
Cross section (pb)	68 ± 8	82.6 ± 12.1	247 ± 46	67.2 ± 6.1	83.6 ± 7.7	232 ± 30.9	$3.30^{+0.52}_{-0.40}$ (sum)

phase space, the t-quark production cross sections usually depend on the value of m_t which is taken for the experimental modeling. For the Tevatron $t\bar{t}$-data [72] this effect leads to a change of $\mathcal{O}(\pm 1\sigma)$ in the measured cross section when m_t is varied by ± 2.5 GeV. To take this dependence into account we have selected for the analysis the value of the cross section of Ref. [72] corresponding to $m_t = 170$ Gev, which is close to our result for m_t^{pole}, cf. Sec. III E. The sensitivity of the other t-quark cross section measurements used in our analysis to the value of m_t is much smaller or not documented. Therefore it is not taken into account.

B. Theory

The theoretical description of the hard-scattering processes follows our previous work ABM12 and the subsequent updates [1–3]. We only consider data in the fit, which can be confronted with QCD predictions at least to NNLO accuracy. This allows the analysis to be based on three major types of scattering reactions: DIS, the Drell-Yan process and the hadro-production of top-quarks in various channels; see also the recent review [11]. In this section, we briefly summarize the theory foundations. Special emphasis is given to the DIS heavy-quark production, where we improve the approximation of the NNLO Wilson coefficients, to the single-top production in the s-channel, as well as to the role of power corrections in DIS, where we refine the treatment of higher twist contributions.

1. DIS

Electron- and neutrino-induced DIS data for NC and CC exchange form the backbone of basically all PDF analyses. The theoretical description of these processes uses the operator product expansion (OPE) on the light cone [73–77] for fixed values of the Bjorken variable x and the (spacelike) momentum transfer between the scattered lepton and the nucleon $Q^2 \to \infty$. The cross sections can be expanded in terms of the well-known (unpolarized) DIS structure functions F_i, $i = 1, 2, 3$.[1] By virtue of the OPE the latter can be expressed as a product of (Mellin moments of) the Wilson coefficients $c_{i,k}$ and operator matrix elements (OMEs) of leading twist $\tau = 2$. The local OMEs for forward scattering are determined by two states of equal momentum p as [78,79]

$$\langle p|O_{\mu_1,\ldots\mu_N}|p\rangle. \tag{1}$$

In the three-flavor nonsinglet cases, the renormalization group equation is a scalar differential equation, while in the singlet case, the quark singlet and the gluon OMEs mix and a 2×2 system has to be solved. In Mellin-N space, for all values of $N \geq N_0$ and N, $N_0 \in \mathbb{N}$, the form of these equations is the same and the corresponding anomalous dimensions for all N [80,81] are known to NNLO and even to N^{3}LO for some low moments [82–85] and in the large n_f-limit [86]. By means of an inverse Mellin transform one obtains the OMEs as a function of Bjorken variable x. In latter form, i.e. as a function of x, the OMEs can also be obtained with the help of the standard QCD factorization theorems [87–95], due to the one-particle notion of the twist $\tau = 2$ OME in Eq. (1).

The QCD corrections to coefficient functions of the hard scattering for NC and CC DIS and including mass effects of heavy quarks have been calculated to sufficient accuracy. The massless coefficient functions for the NC longitudinal structure function F_L are known to NNLO [96] and for F_2 to next-to-next-to-next-to-leading order (N^{3}LO) in QCD. The corresponding massive ones have been determined to good approximation at NNLO in [97] and further improvements will be presented below.

For the neutrino-induced DIS as described by the structure functions $F_i^{\nu p + \bar{\nu} p}$, $i = 1, 2, 3$ when considering the sum of ν and $\bar{\nu}$, exact results for the massless coefficient functions are known as well [98,99] to N^{3}LO, while mass effects have been computed exactly to NLO [100–102] and to NNLO in [103–105] in the asymptotic region for $Q^2 \gg m_c^2$ and in [106] completely, i.e., including also those terms beyond the limit $Q^2 \gg m_c^2$. Details on the treatment of CC DIS heavy-quark production in the PDF analysis have been given in [2] and will be summarized below.

All DIS cross sections within the present PDF analysis have been computed with the code `OPENQCDRAD` (version 2.1), which is publicly available [107]. Note that DIS heavy-quark production is treated entirely in fixed-flavor number scheme using $n_f = 3$ (see, e.g., [5]), and the running-mass definition [108] for m_c and m_b is used.

2. Higher twist

In the twist expansion [73–77], the unpolarized structure functions $F_i(x, Q^2)$ for $i = 2, L, T$ take the form

$$F_i(x,Q^2) = F_i^{\tau=2}(x,Q^2) + \sum_{k=1}^{\infty} \left(\frac{Q_0^2}{Q^2}\right)^k H_i^{\tau=2(k+1)}(x,Q^2), \tag{2}$$

with contributions H_i^τ of higher (dynamical) twist and $Q_0^2 \simeq 1$ GeV^2 denotes a typical reference scale. Unlike the case of polarized DIS, there are no twist $\tau = 3$ contributions in Eq. (2) but dynamical higher twist terms for $\tau = 2n$, $n \in \mathbb{N}$, $n \geq 2$. These terms are largely suppressed in the limit of high virtualities Q^2.

However, the experimental data often exhibit a correlation between x and Q^2 due to similar values of the center-of-mass energy $\sqrt{s}$. Furthermore, in the NC DIS the largest

---

[1] The alternative definitions $F_T = 2xF_1$ and $F_L = F_2 - F_T$ are also used throughout the paper.

statistics is localized in the region of lower values of Q^2. It is often difficult to decide from which scale Q^2 onwards a data sample is widely free of higher twist contributions. It has been proposed [109,110] that a cut on the invariant mass of the hadronic system

$$W^2 = M_P^2 + Q^2(1-x)/x, \tag{3}$$

where M_P is the proton mass, might eliminate the higher twist terms. Specifically, the ranges $W^2 = 12.5 \div 15\ \mathrm{GeV}^2$ for $Q^2 > 4\ \mathrm{GeV}^2$ in the nonsinglet case at current experimental resolutions have been suggested. In the singlet case [71], an additional cut of $Q^2 \gtrsim 10\ \mathrm{GeV}^2$ is necessary to effectively remove the higher twist terms in the current DIS world data. These cuts might change as soon as more precise experiments will be performed [111,112]. Moreover, in any attempt to determine dynamical higher twist contributions from DIS precision data it is necessary also to include all other mass effects, i.e., those due to target masses [113] and due to heavy quarks [104,105,114–119].

The higher twist terms $H_i^\tau(x,Q^2)$ for $i = 2, L, T$ can be decomposed like the leading twist ones into process dependent coefficient functions and process independent higher twist OMEs. In the massless case, the connection between both quantities is given by a series of integration variables x_j

$$H_i^{\tau=2k}(x,Q^2) = \sum_n \int_0^1 dx_1 \ldots \int_0^1 dx_{2k}\,\delta\left(x - \sum_{j=1}^{2k-1} x_j\right) \times c_{i;n}^{\tau=2k}\left(x_j, \frac{Q^2}{\mu^2}\right) O^n\left(x_j, \frac{\mu^2}{\mu_0^2}\right), \tag{4}$$

where the sum runs over all contributing operators, using the quasipartonic operator representation; see e.g., [120]. The local operators of higher twist can be constructed systematically near the light cone. They are formed by more external quark and gluon fields than the twist-two operators and potential contributions of lower twist operators if mass scales are present. An example for a local twist-four operator is given by

$$:\bar\psi(x)\gamma_{\mu_1}\partial_{\mu_2}\ldots\partial_{\mu_m}\psi(x)\bar\psi(y)\gamma_{\nu_1}\partial_{\nu_2}\ldots\partial_{\nu_n}\psi(y):. \tag{5}$$

The OMEs which do not belong to the same representation obey different renormalization group equations. This applies as well to the higher twist Wilson coefficients $c_{i;n}^\tau$ for $\tau \geq 4$, which can be calculated perturbatively. It is important to solve these evolution equations individually, since the scaling violations, through which the respective quantity contributes to the structure functions, turn out to be different. As a consequence, the higher twist terms contribute additively to the leading twist term in Eq. (2) and not multiplicatively, which is sometimes assumed in the literature [121].

Among the $(2k-1)$ contributing momentum fractions in Eq. (4) only the value of x can be accessed experimentally. In particular, there is *a priori* no way to determine the functional structure of the OMEs $O^n(x_j, \mu^2/\mu_0^2)$ with respect to the other variables by fitting data, contrary to the possibility in case of the twist-two terms. In the future, one might in principle consider lattice simulations of these terms, although at the moment no method is known to obtain precise x-space predictions in this way. Therefore, rigorous x-space higher twist QCD analyses of the DIS data are currently impossible.

A more realistic scenario for a consistent QCD analysis of dynamical higher twist contributions is encountered when working in Mellin space. Here the OMEs form matrix representations whose dimensions are growing with growing values of the Mellin variable N, which corresponds to the variable x. The growth in the number of contributing operators becomes more and more significant when going to higher twists. Here, the OMEs are given by pure numbers, which can be determined in an analysis of precise experimental data, realistically up to a specific value of N. However, to comply with the accuracy of the present twist-two analyses the corresponding terms would have to be calculated at NNLO, including the massive corrections to the same order. Moreover, to measure the corresponding moments of the OMEs, it is necessary to extrapolate in the small- and large-x regions. The small-x region is damped to some extent and the problematic part is the region of large values of x. Still, such an analysis is possible; see e.g., [122].

On the theoretical side, systematic twist decompositions have been performed, cf. [123,124]. One forms OMEs with these operators between nucleon states. A "partonic" interpretation assumes, that all external lines can be factorized individually. Early theoretical investigations of the structure of higher twist operators and their anomalous dimensions for ϕ^3-theory in $D = 6$ dimensions [125–127] and for QCD [120,128–146] revealed a basic structure of these contributions. The lowest order anomalous dimensions have been calculated in Refs. [120,143,146] as well as the Wilson coefficients, in different operator bases, in Refs. [138–142,144]. More recently, also gluonic operators were considered [145]. A systematic study of the higher twist light-cone distribution amplitudes was given in Ref. [146]. The renormalization of these operators has been worked out in Refs. [147,148]. The evolution of the lowest twist-four moments at leading order has been illustrated, e.g., in Ref. [149]. We note that the higher twist anomalous dimensions and Wilson coefficients are presently available at low orders in QCD only. Estimates of the higher twist effects have been obtained also by studying renormalon corrections to sum rules and DIS structure functions [150–153]; see also Refs. [154,155].

In current x-space analyses, only an effective determination of higher twist contributions is possible. In the flavor nonsinglet case [110], one uses the cuts mentioned above and studies at lower values of Q^2 the deviations from the twist-two prediction determined in the high Q^2 region based on the N^{3}LO corrections in QCD. Here, the higher twist contributions to the structure functions are fitted simply as parameters depending on x and Q^2, i.e. no assumptions are made on the contributing anomalous dimensions or the Wilson coefficients, cf. Refs. [110,156,157]. Other fits of the dynamical higher twist contributions bin by bin in x and Q^2, both in the nonsinglet and the singlet case, have been performed in Refs. [156–166]. In this approach, it is also important to control the interplay of the size of higher twist terms with contributions to the leading twist Wilson coefficients at higher orders in perturbation theory. In the large-x region, the latter can be obtained for nonsinglet DIS from threshold resummation and subsequent expansion, which generates approximate N^{4}LO corrections; see e.g., Refs. [167,168].

In view of these considerations, we use in the current fit an entirely phenomenologically motivated ansatz for the DIS structure functions including higher twist,

$$F_i^{\mathrm{ht}}(x, Q^2) = F_i^{\mathrm{TMC}}(x, Q^2) + \frac{H_i^{\tau=4}(x)}{Q^2}, \quad i = 2, T, \tag{6}$$

where F_i^{TMC} is given by the leading twist structure function of Eq. (2) together with the target mass corrections [113]; see also [71]. The reference scale in Eq. (2) has been chosen $Q_0^2 = 1\ \mathrm{GeV}^2$ and the higher twist terms H_i^τ are taken to be independent of Q^2, i.e. to correspond to the central value of Q^2 in the respective x range being analyzed. The results for H_i^τ will be presented below in Sec. III.

3. DIS heavy-quark production

The cross section for heavy-quark production in DIS for NC exchange by photons of virtuality Q^2 is expressed in terms of the heavy-flavor structure functions $F_k(x, Q^2, m^2)$ with $k = 2, L$. Here, m is the mass of the heavy quark with $m^2 \gg \Lambda^2_{\mathrm{QCD}}$. The structure functions are given as convolutions of PDFs f_i and coefficient functions $c_{k,i}$, see for instance [169],

$$\begin{aligned} F_k(x, Q^2, m^2) = {}& \frac{\alpha_s e_h^2}{4\pi^2} \xi \sum_{i=q,\bar{q},g} \int_x^{z^{\max}} \frac{dz}{z} f_i\left(\frac{x}{z}, \mu_f^2\right) \\ & \times c_{k,i}(\eta(z), \xi, \mu_f^2, \mu_r^2), \end{aligned} \tag{7}$$

where $z^{\max} = 1/(1 + 4m^2/Q^2)$ and e_h is the heavy-quark charge. The kinematic variables are

$$\eta = \frac{s}{4m^2} - 1, \qquad \xi = \frac{Q^2}{m^2}, \tag{8}$$

with the partonic center-of-mass energy $s = Q^2(1/z - 1)$.

The coefficient functions can be expanded in powers of α_s

$$\begin{aligned} c_{k,i}(\eta, \xi, \mu^2) &= \sum_{j=0}^{\infty} (4\pi\alpha_s)^j c_{k,i}^{(j)}(\eta, \xi, \mu^2) \\ &= \sum_{j=0}^{\infty} (4\pi\alpha_s)^j \sum_{l=0}^{j} c_{k,i}^{(j,\ell)}(\eta, \xi) \ln^\ell \frac{\mu^2}{m^2}, \end{aligned} \tag{9}$$

where we have identified the renormalization and factorization scales $\mu = \mu_f = \mu_r$.

The complete QCD corrections to the coefficient functions in Eq. (9) are known at NLO, i.e., $c_{k,i}^{(1,0)}$ and $c_{k,i}^{(1,1)}$, see Refs. [169–171], as well as all scale-dependent terms at NNLO, i.e., $c_{k,i}^{(2,1)}$ and $c_{k,i}^{(2,2)}$, see Refs. [108,118,172]. Since not all complete results for the scale-independent parts $c_{k,i}^{(2,0)}$ at NNLO were available in 2012, approximate predictions for the most important gluon and the quark pure-singlet coefficient functions $c_{2,g}^{(2,0)}$ and $c_{2,q}^{(2,0)}$ covering a wide kinematic range have been provided in Ref. [97]. These NNLO approximations are based on significant partial information about the threshold region $s \simeq 4m^2$, cf. Refs. [97,172], the high-energy regime $s \gg 4m^2$, cf. Ref. [173], as well as the high-scale region $Q^2 \gg m^2$, cf. Refs. [114,119,174,175]. Since then, important new results have appeared [115–118] which are valid in the limit $Q^2 \gg m^2$ and allow for a substantial improvement of the constructions of Ref. [97] as we discuss below.

In the limit $Q^2 \gg m^2$, the heavy-quark coefficient functions are subject to an exact factorization into the respective coefficient functions with massless quarks $c_{k,j}^{\mathrm{light}}$ and heavy-quark OMEs A_{ij}. Schematically we have for $Q^2 \gg m^2$, that is large ξ,

$$\begin{aligned} c_{k,i}(\eta, \xi, \mu^2) &\to c_{k,i}^{\mathrm{asy}}\left(x, \frac{Q^2}{\mu^2}, \frac{m^2}{\mu^2}\right) \\ &= \left[A_{ji}\left(\frac{m^2}{\mu^2}\right) \otimes c_{k,j}^{\mathrm{light}}\left(\frac{Q^2}{\mu^2}\right)\right](x) + \mathcal{O}\left(\frac{m^2}{Q^2}\right), \end{aligned} \tag{10}$$

where we have indicated that the variable η in Eq. (8) factorizes as $\eta \to Q^2/(4m^2)(1/x - 1) + \mathcal{O}(1)$ and $\otimes$ denotes the standard Mellin convolution, cf. Eq. (7).

The factorization in Eq. (10) can be used to compute the asymptotic expressions $c_{k,i}^{\mathrm{asy}}$ of the heavy-quark coefficient functions for $Q^2 \gg m^2$ at NNLO based on knowledge of the anomalous dimensions [80,81] and coefficient functions for DIS with massless quarks [98,176,177] and the results for the massive OMEs [114,119,174,175] up to three loops. In analogy to Eq. (9), the heavy-quark OMEs in Eq. (10) can be expanded in powers of α_s (note the different normalization convention) as

$$\begin{aligned} A_{ij} &= \delta_{ij} + \sum_{k=1}^{\infty}\left(\frac{\alpha_s}{4\pi}\right)^k A_{ij}^{(k)} \\ &= \delta_{ij} + \sum_{k=1}^{\infty}\left(\frac{\alpha_s}{4\pi}\right)^k \sum_{\ell=0}^{k} a_{ij}^{(k,\ell)} \ln^{\ell}\frac{\mu^2}{m^2}, \end{aligned} \tag{11}$$

where the genuinely new k-th order information resides in the expressions $a_{ij}^{(k,0)}$ for which we will use the short-hand $a_{ij}^{(k)} \equiv a_{ij}^{(k,0)}$. Previous information on $a_{ij}^{(3)}$ at three loops included a number of even-integer Mellin moments [119] and the complete n_f-dependence [114,178]. Thus, for the two important OMEs, the heavy-quark gluon $a_{Qg}^{(3)}$ and the heavy-quark pure-singlet one $a_{Qq}^{(3),\mathrm{ps}}$, decomposed in powers of n_f as

$$a_{Qg}^{(3)} = a_{Qg}^{(3)0} + n_f a_{Qg}^{(3)1}, \tag{12}$$

$$a_{Qq}^{(3),\mathrm{ps}} = a_{Qq,\mathrm{ps}}^{(3)0} + n_f a_{Qq,\mathrm{ps}}^{(3)1}, \tag{13}$$

the expressions for $a_{Qg}^{(3)1}$ and $a_{Qq,\mathrm{ps}}^{(3)1}$ are known exactly [114], while approximations based on some fixed Mellin moments [119] had been given in Ref. [97] for $a_{Qg}^{(3)0}$ and $a_{Qq,\mathrm{ps}}^{(3)0}$. The latter quantities carry a significant residual uncertainty in the small-x region, though, a feature commonly encountered when only a limited number of Mellin moments are known; see e.g., [179]. With the complete exact expression for $a_{Qq}^{(3),\mathrm{ps}}$ now being available [115], the previous approximations [97] can be tested. This is shown in Fig. 1 (left), which demonstrates that the uncertainty band estimates of Ref. [97] have been reasonable, particularly in the small-x region.

In addition, the knowledge of the exact result for $a_{Qq,\mathrm{ps}}^{(3)0}$ also offers a possibility for an improvement of $a_{Qg}^{(3)0}$, since the gluon and pure-singlet quark OME are closely related in the small-x limit. In fact, the leading small-x terms proportional to $x^{-1}\ln x$ (denoted by the superscript LLx in the following) are identical up to simple scaling with the QCD color factors C_A/C_F, that is [173],

$$a_{Qq,\mathrm{ps}}^{(3)0,\mathrm{LLx}} = \frac{C_A}{C_F} a_{Qg}^{(3)0,\mathrm{LLx}}. \tag{14}$$

For the sub-leading small-x terms proportional to x^{-1} this ‘Casimir-scaling’ is not exact anymore, but the deviations are numerically small in known cases, see for instance [81]. One can, therefore, improve the approximation for $a_{Qg}^{(3)0}$ based on the finite number of Mellin moments of Ref. [119] by fixing the coefficient of the x^{-1} term of $a_{Qg}^{(3)0}$ with the help of the C_A/C_F relation in Eq. (14) and allowing for an additional variation of ±10% to model the uncertainty in the small-x region. This leads to a much smaller uncertainty band compared to Ref. [97] for the (unknown) exact functional dependence of $a_{Qg}^{(3)0}$ on x, which is bounded by the following two approximations shown in Fig. 1 (right)

$$\begin{aligned} a_{Qg,A}^{(3)0}(x) &= 354.1002\ln^3(1-x) + 479.3838\ln^2(1-x) \\ &\quad - 7856.784\,(2-x) - 6233.530\ln^2 x \\ &\quad + 9416.621\,x^{-1} + 1548.891\,x^{-1}\ln x, \end{aligned} \tag{15}$$

$$\begin{aligned} a_{Qg,B}^{(3)0}(x) &= 226.3840\ln^3(1-x) - 652.2045\ln^2(1-x) \\ &\quad - 2686.387\ln(1-x) - 7714.786\,(2-x) \\ &\quad - 2841.851\ln^2 x + 7721.120\,x^{-1} \\ &\quad + 1548.891\,x^{-1}\ln x. \end{aligned} \tag{16}$$

The result for $a_{Qg,A}^{(3)0}$ in Eq. (15) has been taken over from Ref. [97] since its small-x behavior is close to the result for

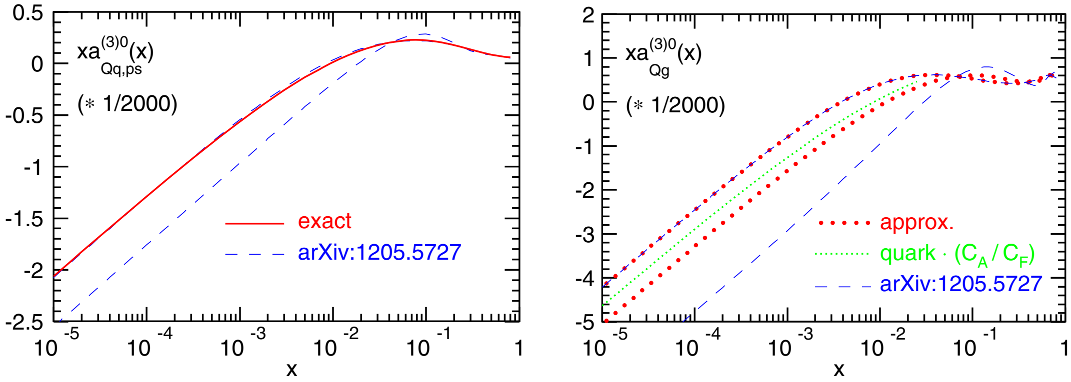

FIG. 1. Left: The exact result for the OME $a_{Qq,\mathrm{ps}}^{(3)0}$ and comparison to previous approximations of Ref. [97]. Right: The new approximations for $a_{Qg}^{(3)0}$ of Eq. (15) and (16) based on the “Casimir-scaled” results for $a_{Qq,\mathrm{ps}}^{(3)0}$ indicated by the thin dotted (green) line and comparison to previous approximations of Ref. [97].

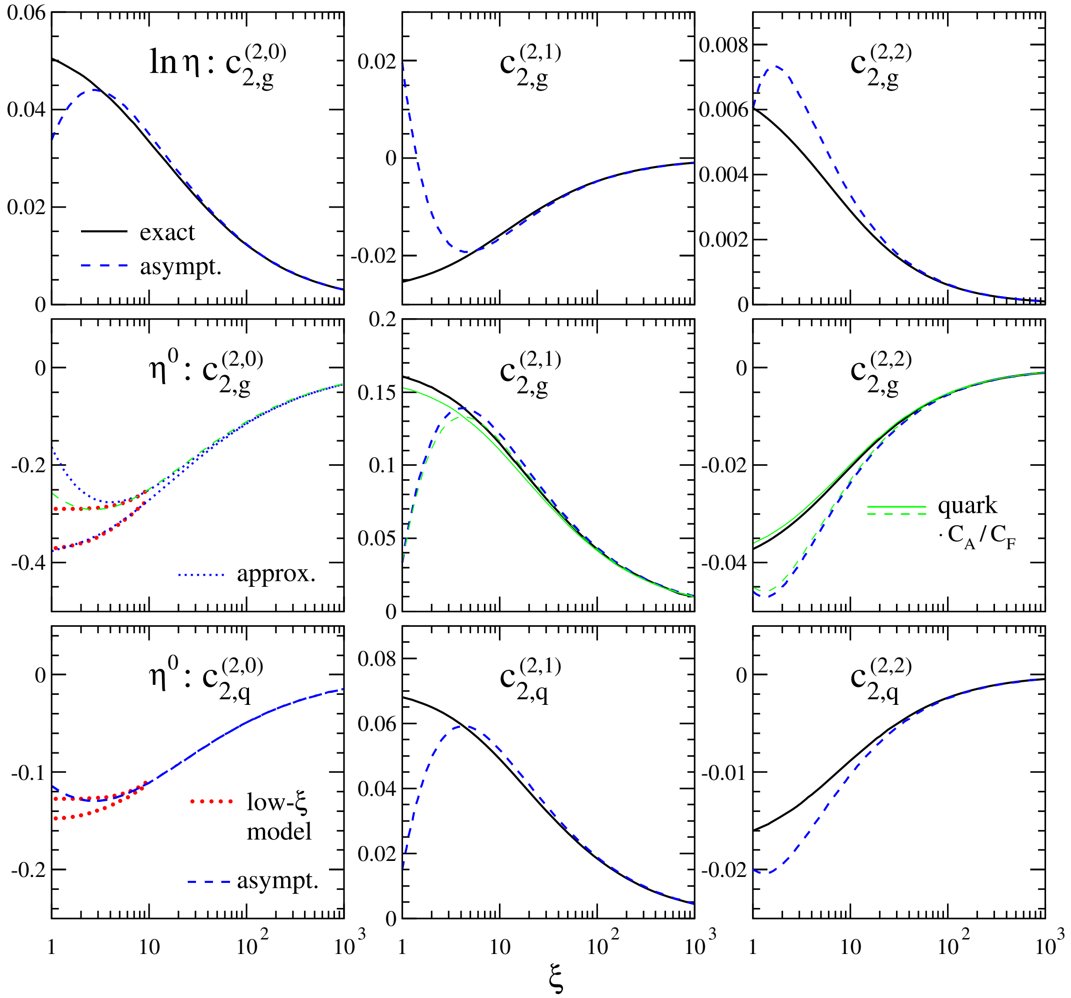

FIG. 2. Top panels: the coefficients of the leading small-x/high-η logarithm for the contributions $c_{2,g}^{(2,\ell)}$, $\ell = 0,\, 1,\, 2$, to the NNLO gluon coefficient function defined in Eq. (9). Middle and bottom panels: the respective next-to-leading η^0 coefficients for $c_{2,g}^{(2)}$ and $c_{2,q}^{(2)}$. The solid (black) lines are the exact all-Q^2 results, the dashed (blue) ones the high-scale asymptotic results $c_{2,g}^{(2)\mathrm{asy}}$ and $c_{2,q}^{(2)\mathrm{asy}}$ defined in Eq. (10); the dotted (red) ones the low-scale extrapolations of Eqs. (A3)–(A6). Also illustrated, by the thin (green) lines in the bottom panels, is the small next-to-leading high-η deviation of $c_{2,g}^{(2)}$ from the "Casimir-scaled" results for $c_{2,q}^{(2)}$.

$a_{Qq,\mathrm{ps}}^{(3)0}$ rescaled by the factor C_A/C_F plus the additionally added shift of 10% as can be seen in Fig. 1 (right) where the previous approximations of Ref. [97] are shown as well. It is obvious from the plot that the new information on the small-x behavior [115] helps to reduce the uncertainty on $a_{Qg}^{(3)0}$ significantly.

Repeating the construction of Ref. [97], we are then in a position to improve the gluon and pure-singlet heavy-quark coefficient functions at NNLO, with details being summarized in Appendix A. In short, two approximations, A and B, are determined for each function, $c_{2,g}^{(2,0)}$ and $c_{2,q}^{(2,0)}$, based on Eqs. (15) and (16) and extrapolations to the region of large-η and low-ξ. These variants A and B, given in Fig. 2 and Eqs. (A1) and (A2), can be considered as the two extremes of the approximation procedure described in Ref. [97]. With these improvements at hand, we can provide new approximate NNLO results for the charm-quark structure functions $F_2(x, Q^2, m^2)$ in Eq. (7). In Fig. 3, we display $F_2(x, Q^2, m^2)$ at NLO and NNLO for charm-quarks at the values of $\xi = 5$ and 10 and for a range of scales μ. We use the $\overline{\mathrm{MS}}$ mass definition with $m_c(m_c) = 1.27$ GeV and the ABM12 PDFs [1] at NNLO. It is clear from Fig. 3 that the residual uncertainty in $F_2(x, Q^2, m^2)$ at NNLO due to the approximations A and B of Eqs. (A1) and (A2) is small and becomes even negligible in most kinematic regimes compared to the residual theoretical uncertainty from truncating the perturbative expansion. The latter is conventionally estimated by a variation of the scale $\mu = \kappa\sqrt{Q^2 + 4m_c^2}$ in the range $1/2 \le \kappa \le 2$ around the nominal scale choice $\kappa = 1$ as indicated by

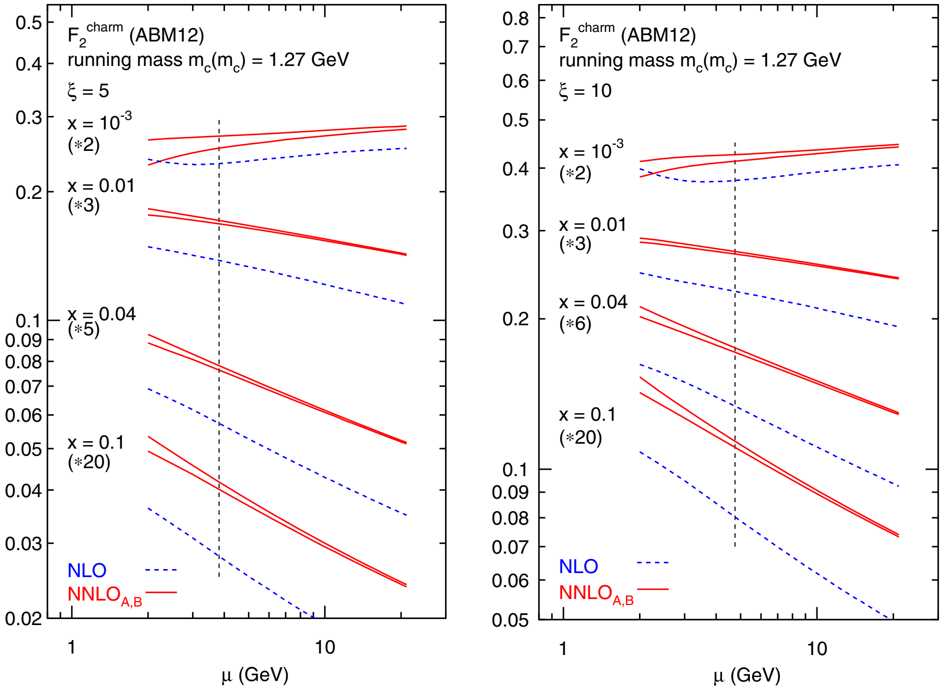

FIG. 3. Scale dependence of the heavy-quark structure function F_2^c for $\mu = \mu_R = \mu_F$ at NLO and at NNLO with the approximations A and B of Eqs. (A1) and (A2) for two values of $\xi = Q^2/m_c^2$. The dashed vertical line denotes the choice $\mu = \sqrt{Q^2 + 4m_c^2}$.

the dashed vertical lines in Fig. 3. Except for very small x and low ξ the scale variation always dominates.

Further theoretical improvements for structure functions of heavy-quark DIS can be expected from the complete three-loop result for the heavy-quark OME A_{Qg} in analogy to Ref. [115] including $a_{Qg}^{(3)0}$, which is in progress. This would narrow down the uncertainty band spanned by the approximations A and B in Eqs. (A1) and (A2) in the small-x region. In addition, a dedicated computation of the next-to-leading terms in the high-energy regime $s \gg 4m^2$ along the lines of Ref. [173] would eliminate the remaining uncertainties from the low-scale extrapolations of Eqs. (A3)–(A6).

The fit of the heavy-quark measurements from HERA with the new NNLO approximation for the heavy-quark structure functions presented here leads to significantly reduced theoretical uncertainties, in particular for the charm-quark mass $m_c(m_c)$ in the $\overline{\mathrm{MS}}$ scheme. Results will be discussed below in Sec. III.

For heavy-quark production in CC DIS one considers at parton level in Born approximation the process

$$s(p) + W^*(q) \to c, \tag{17}$$

where the initial s-quark is taken massless and the final state charm-quark is heavy. The coupling to the W-boson involves the usual parameters of the Cabibbo-Kobayashi-Maskawa (CKM) matrix. The cross section for this process including higher order QCD corrections is expressed in terms of the corresponding heavy-quark CC DIS structure functions F_k, $k = 1, 2, 3$, as

$$F_k(x, Q^2, m^2) = \sum_{i=q,\bar{q},g} \int_\chi^1 \frac{dz}{z} f_i\left(\frac{x}{z}, \mu_f^2\right) \mathcal{C}_{k,i}(z, \xi, \mu_r^2, \mu_f^2), \tag{18}$$

where $\mathcal{C}_{k,i}$ denote the heavy-quark coefficient functions of CC DIS with kinematical variables as defined in Eq. (8). The integration over the parton momentum fraction z in Eq. (18) is limited by $\chi = x/\lambda$ and λ is given by $\lambda = 1/(1 + m^2/Q^2) = \xi/(1 + \xi)$.

For the QCD description of the structure functions F_k in Eq. (18) we aim at NNLO accuracy, which implies to keep for the coefficient functions all terms $\mathcal{C}_{k,i}^{(l)}$ with $l \leq 2$ in the perturbative expansion defined in Eq. (9). At NLO exact expressions for $\mathcal{C}_{k,i}^{(1)}$ are available [100–102]. At NNLO, following the approach already used in Ref. [2], we approximate $\mathcal{C}_{k,i}^{(2)}$ with the respective results in the asymptotic limit $Q^2 \gg m^2$ derived in Refs. [103–105]. Given the relevant kinematic range of the data, the use of these approximate NNLO predictions for $\mathcal{C}_{k,i}^{(2)}$ is well justified and sufficiently accurate for the HERA data [118,180]. In addition, the QCD corrections for CC DIS heavy-quark production are generally small for scale choices $\mu = \sqrt{Q^2 + m^2}$ and the main effect of the NNLO correction is a reduction of the theoretical uncertainties due to variations of μ_r and μ_f. This has been confirmed in a recent computation [106] of the exact NNLO contributions to Eq. (18), i.e., including the complete result for $\mathcal{C}_{k,i}^{(2)}$ with all terms beyond the asymptotic limit $Q^2 \gg m^2$.

4. Drell-Yan process

The QCD predictions for the Drell-Yan process are known to NNLO for fully exclusive kinematics. This is essential, since the differential distributions in the lepton rapidity from the $W^{\pm}$- and Z-boson decay provide important constraints for the flavor separation of the light-quark PDFs. In addition, due to the detector acceptance being limited at collider experiments the data are obtained in a restricted phase space and the $W^{\pm}/Z$-boson event selection criteria typically impose a cut on the lepton's transverse momentum p_T^l.

To take into account such cuts we have used the publicly available code `FEWZ` (version 3.1) [181,182] designed for computation of the fully differential NNLO QCD predictions for the lepton rapidity distributions. The computations are performed in the factorization scheme with $n_f = 5$ flavors. Therefore the 5-flavor PDFs are taken as an input. These PDFs are obtained from the $n_f = 3$ flavor ones using the OMEs of Ref. [183]. A common prescription for the values of the matching scales, m_c and m_b, is applied for the generation of the 4- and 5-flavor PDFs, respectively. Furthermore, to be consistent with the Wilson coefficients for heavy-quark DIS production in Sec. II B 3 we also employ the $\overline{\mathrm{MS}}$ mass definition for the OMEs. `FEWZ` (version 3.1) can estimate PDF uncertainties in the cross sections by sampling over all members of a given PDF set simultaneously. This allows also for a fast and efficient algorithm to compute the NNLO QCD predictions for the current parameters of a new fit using the 1σ variations in the fitted parameters provided by the PDF set members. This approach has been used in the ABM12 [1] and ABMP15 [3] fits previously.[2]

A new feature in the current analysis already discussed in ABMP15 [3] is the change in the parametrization of the light-quark PDFs so that the shape of the iso-spin asymmetry $I(x) = x[\bar{d}(x) - \bar{u}(x)]$ is now model-independent. Previously in the ABM12 fit, a constraint $I(x) \sim x^{0.7}$ has been imposed, which was motivated by Regge-phenomenology arguments valid in the asymptotic limit for $x \to 0$. Details for the explicit onset of such an asymptotic behavior have thus far not been specified in the literature, though, and the fit results of ABMP15 [3] have returned a nonzero iso-spin asymmetry of the light-quark sea $I(x)$ at small values of Bjorken $x \sim 10^{-4}$. A turnover of this trend at even smaller x still allows for a Regge-like shape at $x \sim 10^{-6}$. These findings are corroborated in the present analysis and will be discussed below in Sec. III.

5. Hadro-production of top-quarks

Theory predictions including QCD corrections to NNLO are known exactly for the hadro-production of top-quark pairs and for single-top production in the t- and s-channel to good approximation. The various top-quark production processes determine the top-quark mass and help to constrain the gluon PDF ($t\bar{t}$ data) as well as the light-quark PDFs in the ratio d/u at large x (single-top t-channel data).

In the current analysis, we apply the NNLO QCD predictions for inclusive $t\bar{t}$ cross section [184–187] together with the conversion for the top-quark mass $m_t(\mu_r)$ in the $\overline{\mathrm{MS}}$ scheme as discussed in Refs. [188–190]. The NNLO QCD corrections for single-top production in the t-channel have been obtained in the structure function approximation [191] (see also Ref. [192]), which neglects color suppressed contributions and is sufficient in view of the current experimental precision. The higher order QCD corrections are small so that we can use the factor $k = 0.984$ calculated in [191] for the inclusive cross section for t-channel single-top production to rescale the NLO QCD corrections to NNLO accuracy; see also [193] for further discussions. For the s-channel single-top production the QCD corrections are known to NLO [194,195]. In addition, approximations for the NNLO corrections to the inclusive cross section have been provided in Refs. [196–198] based on soft-gluon resummation and have been applied in Ref. [193].

All necessary theory predictions are computed with the `Hathor` package [189,199] in the $n_f = 5$ flavor factorization scheme. Therefore we take 5-flavor PDFs as an input, similarly to the case of W- and Z-boson production, cf. Sec. II B 4. Consistently with the charm and bottom DIS production we always use the top-quark mass $m_t(\mu_r)$ in the $\overline{\mathrm{MS}}$ scheme. In this renormalization scheme for the mass, the cross sections typically exhibit very good perturbative convergence and scale stability with respect to variation of the renormalization and factorization scales μ_r and μ_f. The fit results for the top-quark mass $m_t(m_t)$ are reported below in Sec. III.

III. RESULTS

A. Quality of data description

The total number of data points (NDP) used in the fit is 2860 and the value of χ^2 per number of data points $\chi^2/NDP = 1.18$ obtained is comparable to the one of the ABM12 fit.[3] As in our previous studies the pulls defined as

---

[2] See the Appendix of Ref. [1] for implementation details of the fast algorithm used for iterated theoretical computations in the PDF fit.

[3] We use the standard definition of χ^2 [200] with the error correlations taken into account in the covariance matrix, when available.

TABLE V. The values of χ^2 obtained in the present analysis for the data on inclusive DIS, the fixed-target DY process, and on heavy-quark production. The collider DY data are listed in Table VI.

Experiment	Process	Reference	NDP	χ^2
DIS				
HERA I + II	$e^\pm p \to e^\pm X$ $e^\pm p \to \overset{(-)}{\nu} X$	[4]	1168	1510
BCDMS	$\mu^+ p \to \mu^+ X$	[61]	351	411
NMC	$\mu^+ p \to \mu^+ X$	[60]	245	343
SLAC-49a	$e^- p \to e^- X$	[54,62]	38	59
SLAC-49b	$e^- p \to e^- X$	[54,62]	154	171
SLAC-87	$e^- p \to e^- X$	[54,62]	109	103
SLAC-89b	$e^- p \to e^- X$	[56,62]	90	79
DIS heavy-quark production				
HERA I + II	$e^\pm p \to e^\pm c X$	[63]	52	62
H1	$e^\pm p \to e^\pm b X$	[15]	12	5
ZEUS	$e^\pm p \to e^\pm b X$	[16]	17	16
CCFR	$\overset{(-)}{\nu} N \to \mu^\pm c X$	[64]	89	62
CHORUS	$\nu N \to \mu^+ c X$	[18]	6	7.6
NOMAD	$\nu N \to \mu^+ c X$	[17]	48	59
NuTeV	$\overset{(-)}{\nu} N \to \mu^\pm c X$	[64]	89	49
DY				
FNAL-605	$pCu \to \mu^+ \mu^- X$	[68]	119	165
FNAL-866	$pp \to \mu^+ \mu^- X$ $pD \to \mu^+ \mu^- X$	[69]	39	53
Top-quark production				
ATLAS, CMS	$pp \to tqX$	[27–32]	10	2.3
CDF&D0	$\bar{p}p \to tbX$ $\bar{p}p \to tqX$	[53]	2	1.1
ATLAS, CMS	$pp \to t\bar{t}X$	[33–52]	23	13
CDF&D0	$\bar{p}p \to t\bar{t}X$	[53]	1	0.2

a relative deviation of the experimental data off the resulting fit predictions do not demonstrate any statistically significant trend and no additional improvements can evidently be achieved by further releasing the PDF shape, cf. Sec. III B. A detailed breakdown of the values of χ^2 for the separate processes and data sets is given in Tables V and VI and discussed in the following.

1. DIS data

The data sets newly included into the present analysis are smoothly accommodated in general, while keeping the quality of the fixed-target BCDMS, NMC and SLAC data included in the earlier ABM12 fit. In particular, this applies to the HERA inclusive DIS data obtained from the combination of the statistics of run I and II [4]. No trend can be observed in the pulls of this sample plotted in Figs. 4–6, although the fluctuations in the central values of the data extend somewhat beyond the published uncertainties. As a result, these fluctuations prevent a statistically ideal description of the inclusive HERA data yielding values of χ^2/NDP slightly bigger than one. However, the fit cannot be improved in any essential way by further relaxing the fitted PDF shape.

We have also checked the combined HERA inclusive data with varying cuts on Q^2. Due to bigger errors in the data at large Q^2 the value of χ^2/NDP is smaller for the variants of the fit with more stringent cuts on Q^2. We find $1350/1092 = 1.24$ and $1225/1007 = 1.22$ for the cuts of $Q^2 > 5\ \text{GeV}^2$ and $Q^2 > 10\ \text{GeV}^2$, respectively. The same conclusion was drawn in a previous QCD analysis [4], however, the values of χ^2 reported in Ref. [4] are somewhat smaller than ours due to the limited number of data sets employed in that analysis.

2. Drell-Yan data

Due to large amount of the DY data from Tevatron and the LHC a precision determination of the light-quark PDFs in a wider kinematic range in x than ever before becomes possible; see also [3]. The quality of the ABMP16 fit for the Drell-Yan data description is summarized in Table VI. Data sets of lower accuracy, which have become obsolete and data sets superseded are not listed there. Instead, we refer to the review [11] for further comparisons concerning the status of Drell-Yan data in PDF fits.

In general, the data sets in Table VI with a total $NDP = 172$ can be smoothly accommodated, although the values of χ^2/NDP obtained for individual data sets are bigger than one in some places. This is the case, for instance, for the CMS data on the muon charge asymmetry collected at the collision energy of $\sqrt{s} = 7$ TeV shown in Fig. 7, which yields a value of $\chi^2/NDP \sim 2$. Similar CMS data for $\sqrt{s} = 8$ TeV, however, are much smoother, cf. the pulls in Figs. 7 and 8, and a good value of χ^2/NDP is achieved in this case. Therefore, the observed fluctuations in the CMS data for $\sqrt{s} = 7$ TeV should rather be attributed to experimental systematic effects than to any shortcomings in the fitted PDFs.

The pulls for the LHCb data on the muon charge asymmetry collected at $\sqrt{s} = 7$ TeV [19] are shown in Fig. 9. They display an irregularity at pseudo-rapidity $\eta_\mu = 3.275$, which is not confirmed by the LHCb data at $\sqrt{s} = 8$ TeV [20]. Moreover, this spike at $\eta_\mu = 3.275$ coincides with fluctuations in the correction for final-state radiation which has been applied to the LHCb data, cf. Fig. 5 in Ref. [3]. The two data points for W^+- and W^--boson production corresponding to this spike contribute about 13 units to the value of χ^2 and, in line with our earlier analysis [3], we discard these two data points from the fitted set. This has only marginal impact on the fit results.

The pulls for the LHCb data on the W-production at $\sqrt{s} = 8$ TeV [20] are displayed in Fig. 10. They exhibit an excess at $\eta_\mu = 2.125$ both in μ^+ and μ^- channels, while the muon charge asymmetry remains smooth. Since these two

TABLE VI. Compilation of precise data on W- and Z-boson production in pp and $p\bar{p}$ collisions and the χ^2 values obtained for these data sets in different PDF analyses using their individual definitions of χ^2. The NNLO fit results are quoted as a default, while the NLO values are given for the CJ15 [6] and `HERAFitter` [201] PDFs. Missing table entries indicate that the respective data sets have not been used in the analysis.

Experiment	ATLAS		CMS		DØ		LHCb		
$\sqrt{s}$ (TeV)	7	13	7	8	1.96		7	8	
Final states	$W^+ \to l^+\nu$ $W^- \to l^-\nu$ $Z \to l^+l^-$	$W^+ \to l^+\nu$ $W^- \to l^-\nu$ $Z \to l^+l^-$	$W^+ \to \mu^+\nu$ $W^- \to \mu^-\nu$ (asym)	$W^+ \to \mu^+\nu$ $W^- \to \mu^-\nu$	$W^+ \to \mu^+\nu$ $W^- \to \mu^-\nu$ (asym)	$W^+ \to e^+\nu$ $W^- \to e^-\nu$ (asym)	$W^+ \to \mu^+\nu$ $W^- \to \mu^-\nu$ $Z \to \mu^+\mu^-$	$Z \to e^+e^-$	$W^+ \to \mu^+\nu$ $W^- \to \mu^-\nu$ $Z \to \mu^+\mu^-$
Cut on the lepton P_T	$P_T^l > 20$ GeV	$P_T^e > 25$ GeV	$P_T^\mu > 25$ GeV	$P_T^\mu > 25$ GeV	$P_T^\mu > 25$ GeV	$P_T^e > 25$ GeV	$P_T^\mu > 20$ GeV	$P_T^e > 20$ GeV	$P_T^\mu > 20$ GeV
Luminosity (1/fb)	0.035	0.081	4.7	18.8	7.3	9.7	1	2	2.9
Reference	[67]	[26]	[24]	[25]	[23]	[22]	[19]	[21]	[20]
NDP	30	6	11	22	10	13	31	17	32
χ^2 Present analysis[a]	31.0	9.2	22.4	16.5	17.6	19.0	45.1	21.7	40.0
CJ15 [6]	...	...	...	...	20	29	...	...	...
CT14 [7]	42	...	...[b]	...	...	34.7	...	...	...
JR14 [8]	...	...	...	...	...	...	...	...	...
`HERAFitter` [201]	...	...	...	...	13	19	...	...	...
MMHT14 [9]	39	...	...	...	21	...	...	...	...
NNPDF3.0 [10]	35.4	...	18.9	...	...	...	...	...	...

[a] The ABM12 [1] analysis has used older data sets from CMS and LHCb.

[b] For the statistically less significant data with the cut of $P_T^\mu > 35$ GeV the value of $\chi^2 = 12.1$ was obtained.

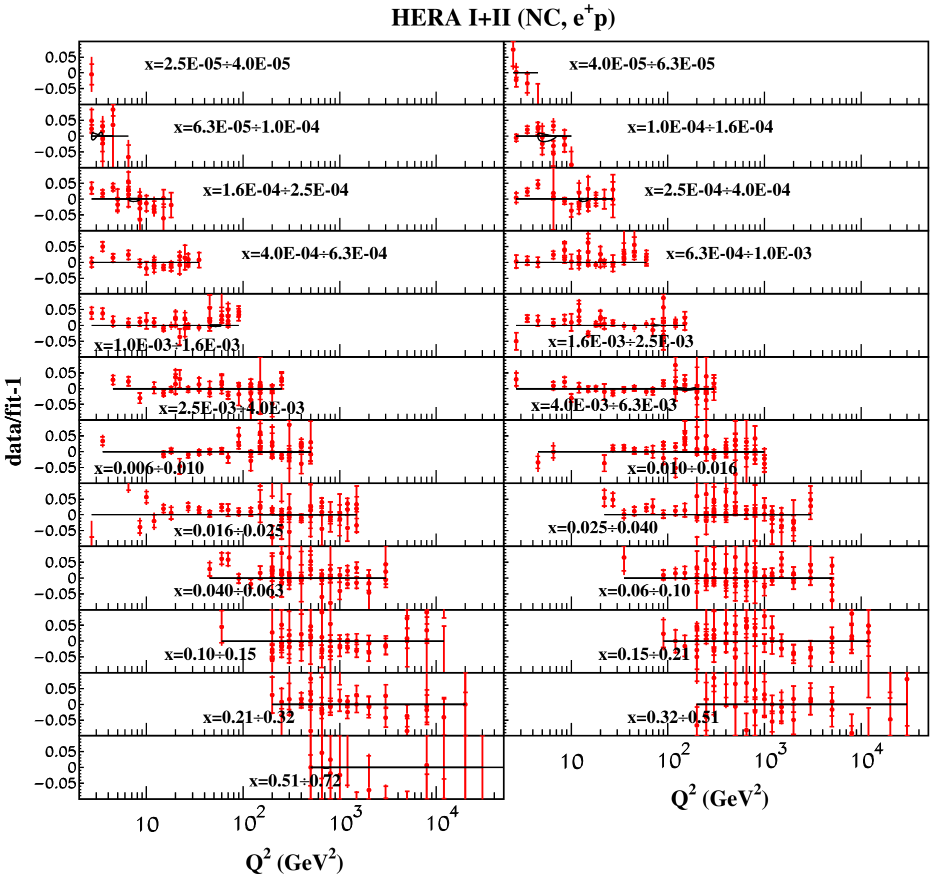

FIG. 4. The pulls versus the momentum transfer Q^2 for the final HERA NC e^+p inclusive DIS data [4] in bins of Bjorken x with respect to the present NNLO fit.

points also give a quite sizeable contribution to the value of χ^2, about 14 units, we discard them from the fitted set. Similar to the spike in LHCb data at $\sqrt{s} = 7$ TeV, we find again only a marginal impact of this filtering procedure on the results.

The LHCb data on the electron charge asymmetry collected at $\sqrt{s} = 8$ TeV [202] are in broad agreement with the NNLO QCD predictions based on our ABMP16 PDFs as demonstrated in Fig. 11. However, significant fluctuations occur in some places, in particular for the pseudo-rapidity bin at $\eta_e = 4$, which is the biggest one available in this sample. The uncertainties in the data are dominated by the systematic ones, which are strongly correlated. This prevents us from achieving a reasonable value of χ^2 in the fit. Moreover, the electron data also demonstrate a different trend as compared to the muon ones. As a consequence, we do not include the LHCb electron set from $\sqrt{s} = 8$ TeV into the fit until these issues are resolved.

In contrast, the $\sqrt{s} = 8$ TeV LHCb data on the Z-boson production and decay in the electron mode [21] are generally in a good agreement with the fit and also with the ones for the muon decay mode [20] as shown in Fig. 12. The muon channel data are somewhat enhanced at small rapidity, similar to the LHCb W-boson sample at $\sqrt{s} = 8$ TeV. However, this enhancement is statistically not significant due to the limited accuracy of the Z-boson data [20]. The pulls for the first LHCb Z-boson data obtained at the collision energy of $\sqrt{s} = 13$ TeV are given in Fig. 12. These data are also broadly in agreement with the present fit and with our earlier predictions based on the ABM12 and ABMP15 PDFs. However, the Z-boson data collected for the electron decay mode are subject to more significant fluctuations and for this data set we achieve only a value of $\chi^2/NDP \simeq 2$ taking the ABMP16 PDFs. This confirms a tendency, that the description of the electron LHCb W- and Z-boson data is inferior to the muon ones. The uncertainties in the existing LHCb data at $\sqrt{s} = 13$ TeV are still quite big as compared to the earlier data sets at lower collision energies and to the PDF uncertainties in the current theoretical predictions, cf. Fig. 12. This puts a limitation on a potential impact of these data on the PDF extraction and, therefore, we do not include them into the fit.

Finally, we briefly discuss cross section ratios for the production of $W^\pm$- and Z-bosons integrated over the fiducial volume. The recent ATLAS data on those ratios at the collision energy at $\sqrt{s} = 13$ TeV [26] is shown in

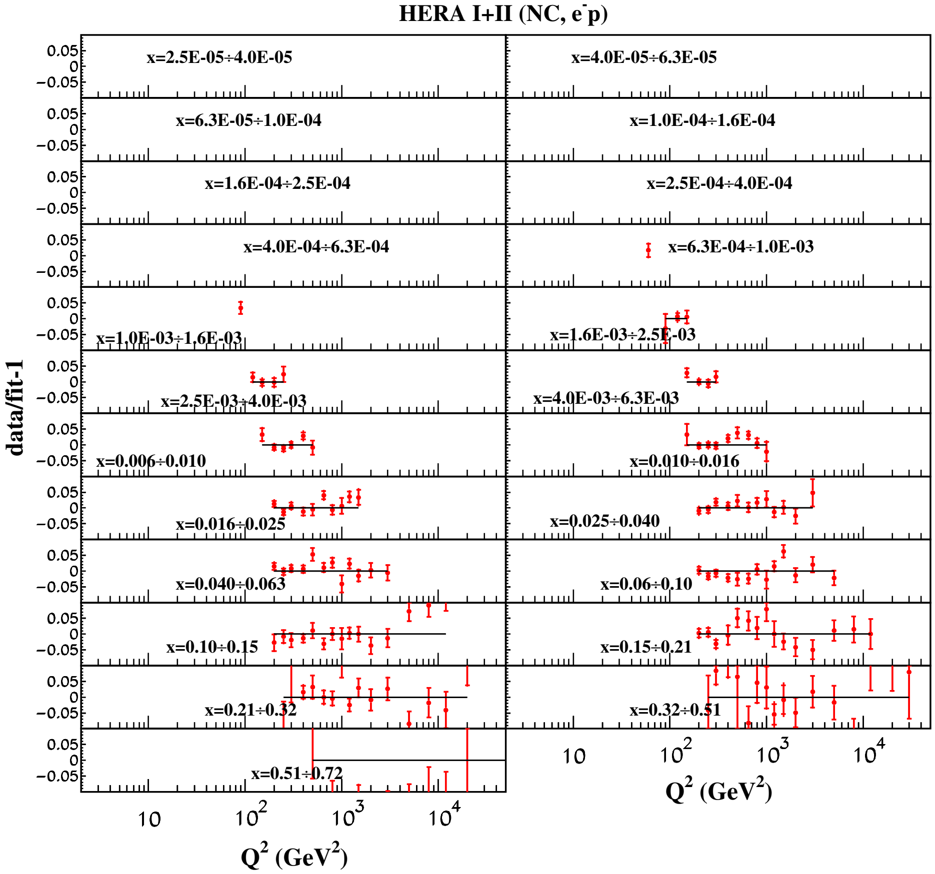

FIG. 5. The same as in Fig. 4 for the NC e^-p inclusive DIS data [4].

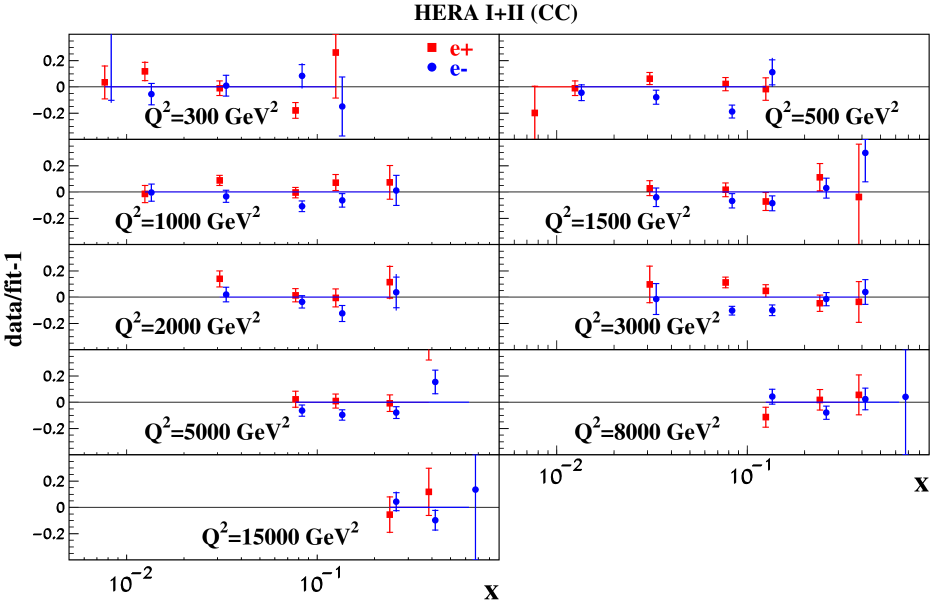

FIG. 6. The same as in Fig. 4 for the CC e^+p (squares) and e^-p (circles) inclusive DIS data [4] versus Bjorken x in bins of the momentum transfer Q^2.

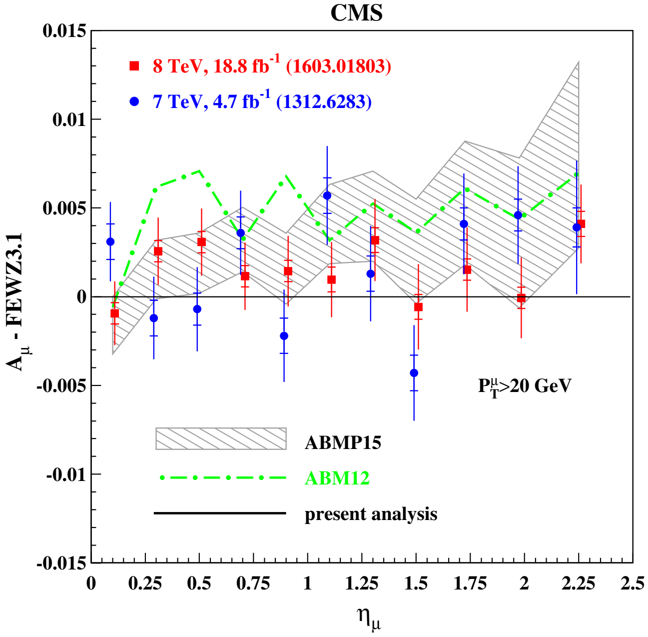

FIG. 7. The pulls for the CMS data on the muon charge asymmetry A_μ in inclusive $pp \to W^\pm + X \to \mu^\pm\nu + X$ production at $\sqrt{s} = 7$ TeV [24] (circles) and 8 TeV [25] (squares) with the muon transverse momentum $P_T^\mu > 20$ GeV and as a function of the muon pseudo-rapidity η_μ with respect to our fit. The ABM12 [1] central predictions for the CMS data at $\sqrt{s} = 8$ TeV [25] obtained with `FEWZ` (version 3.1) [181,182] (dotted dashes) and the uncertainty band for the ABMP15 ones [3] (hatched) with respect to our fit are given for comparison.

Fig. 13. Our earlier ABM12 predictions somewhat overshoot the data, whereas the agreement with the more recent ABMP15 PDFs is better. For the present analysis a good agreement within the uncertainties is achieved as quantified in Fig. 13.

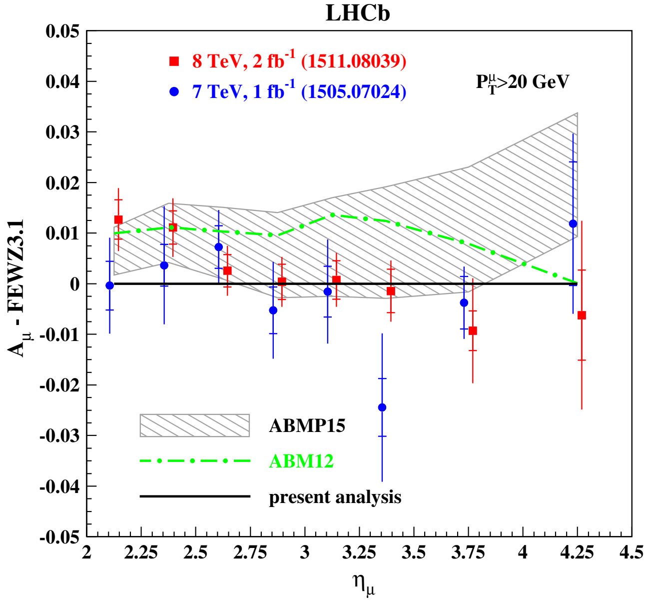

FIG. 9. The same as in Fig. 7 for the LHCb data on the muon charge asymmetry A_μ in inclusive $pp \to W^\pm + X \to \mu^\pm\nu + X$ production at $\sqrt{s} = 7$ TeV [19] (circles) and 8 TeV [20] (squares). The data at $\eta_\mu = 3.275$ and $\sqrt{s} = 7$ TeV are not used in the fit.

3. Data on heavy-quark production

The theoretical framework of Sec. II B 3 provides an excellent description of the data on c- and bottom-quark production in the NC electron-proton DIS collected by the H1 and ZEUS experiments at HERA in the range of Q^2 available, cf. Figs. 14, 15. The same applies to the charm-quark production in CC neutrino-nucleon DIS measured in the fixed-target experiments. In particular, the NOMAD [17] and CHORUS [18] data, which were earlier smoothly included into an updated version [2] of the ABM12 fit are

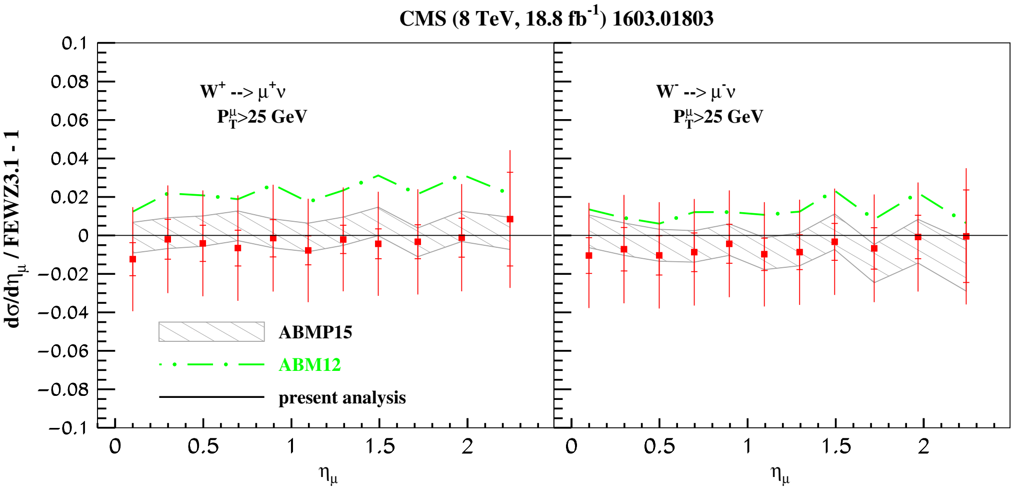

FIG. 8. The same as Fig. 7 for the CMS data on the cross section of inclusive W-boson production at 8 TeV [25].

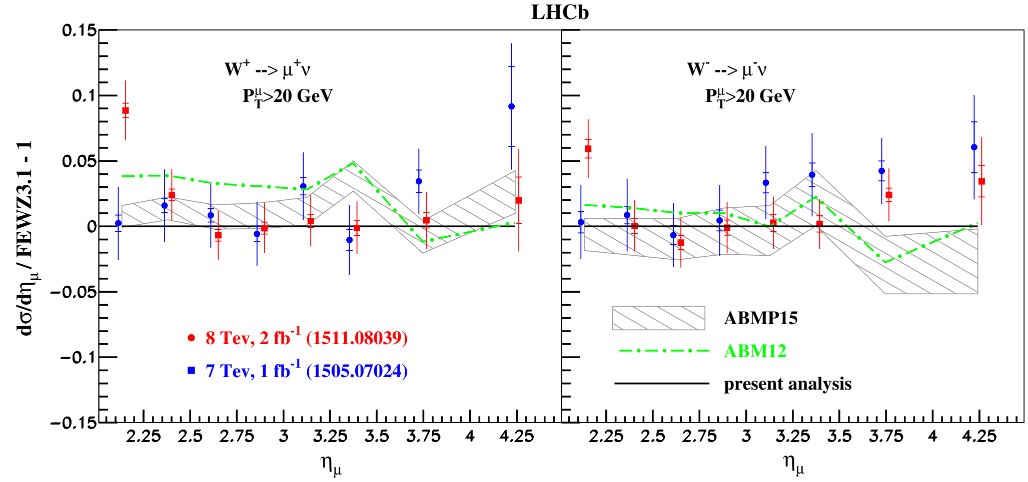

FIG. 10. The same as in Fig. 7 for LHCb data on the cross section of inclusive W-boson production in the pp collision (left: $pp \to W^+ + X \to \mu^+\nu + X$, right: $pp \to W^- + X \to \mu^-\nu + X$) at $\sqrt{s} = 7$ TeV [19] (circles) and $\sqrt{s} = 8$ TeV [20] (squares) with the muon transverse momentum $P_T^\mu > 20$ GeV and as a function of the muon pseudo-rapidity η_μ with respect to our fit. The points with the lowest $\eta_\mu = 2.125$ at $\sqrt{s} = 8$ TeV are not used in the fit.

also well described by the present PDFs, cf. Table V. Finally, the newly included Tevatron and LHC data on $t\bar{t}$ and single-t production are in good agreement with the fit, cf. Figs. 16, 17.

B. PDF improvement

In the present analysis, we parametrize PDFs in the scheme with $n_f = 3$ light flavors at a starting scale $\mu_0 = 3$ GeV of the QCD evolution by the following form

$$xq_v(x,\mu_0^2) = \frac{2\delta_{qu} + \delta_{qd}}{N_q^v}(1-x)^{b_{qv}} x^{a_{qv}P_{qv}(x)} \tag{19}$$

for the valence quark distributions q_v, where $q = u$, d and $\delta_{qq'}$ denotes the Kronecker symbol,

$$xq_s(x,\mu_0^2) = x\bar{q}_s(x,\mu_0^2) = A_{qs}(1-x)^{b_{qs}} x^{a_{qs}P_{qs}(x)} \tag{20}$$

for the sea quark distributions, where $q = u$, d, s, and

$$xg(x,\mu_0^2) = A_g(1-x)^{b_g} x^{a_g P_g(x)} \tag{21}$$

for gluons. While the small- and large-x PDF asymptotic is defined by the exponents a and b, respectively, the functions $P_p(x)$ take a general form

$$P_p(x) = (1 + \gamma_{-1,p}\ln x)(1 + \gamma_{1,p}x + \gamma_{2,p}x^2 + \gamma_{3,p}x^3), \tag{22}$$

where $p = qv, qs, g$. This allows for flexibility of the PDFs in the entire range of x. As is common practice the PDFs

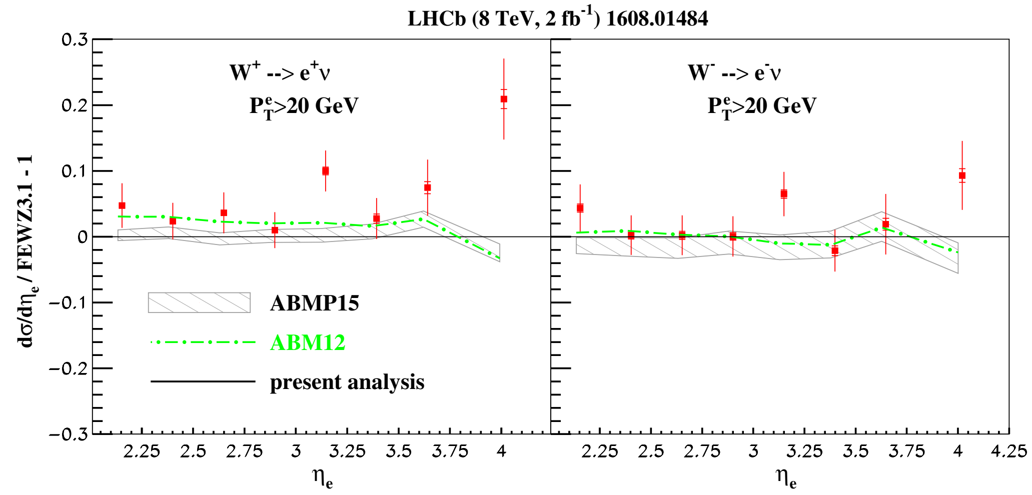

FIG. 11. The same as Fig. 10 for the LHCb data on the cross section of inclusive $pp \to W^+ + X \to e^+\nu + X$ (left) and $pp \to W^- + X \to e^-\nu + X$ (right) production at 8 TeV [202].

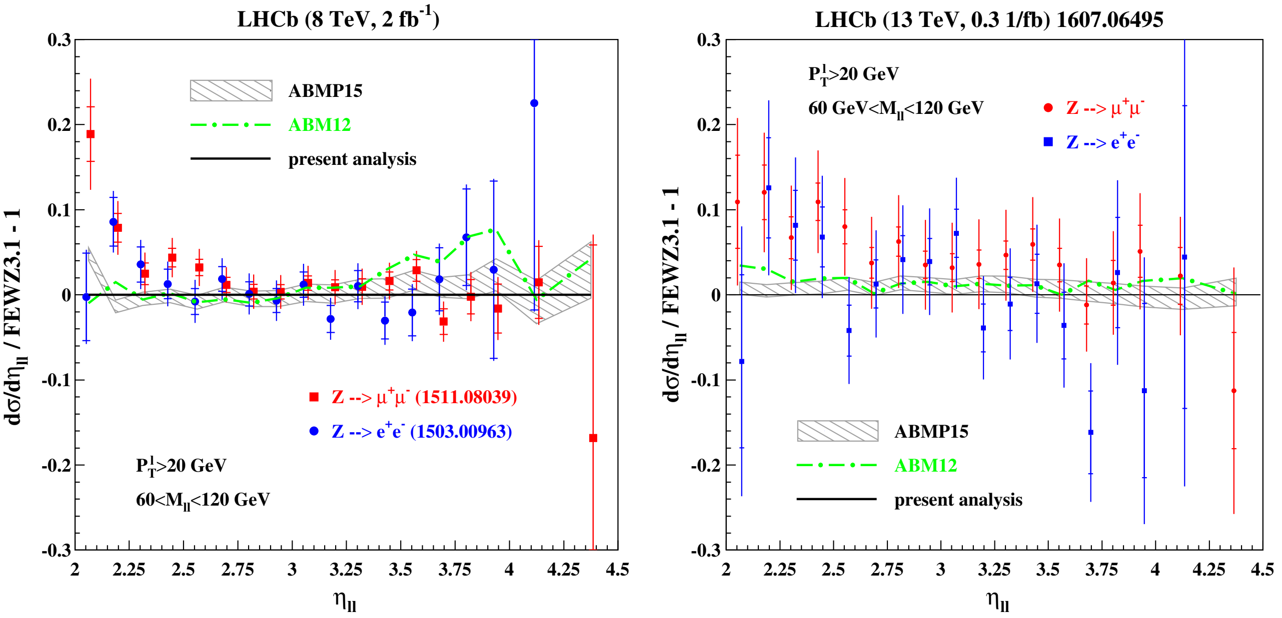

FIG. 12. Left panel: The same as in Fig. 10 for the LHCb data on the inclusive $pp \to Z + X \to l^+l^- + X$ production at $\sqrt{s} = 8$ TeV for the muon [20] (circles) and electron [21] (squares) decay modes with the lepton transverse momentum $P_T^l > 20$ GeV, the lepton pair mass 60 GeV $< M_{ll} <$ 120 GeV and as a function of the lepton pair pseudo-rapidity η_{ll}. Right panel: The same for the LHCb data on the inclusive $pp \to Z + X \to l + l^- + X$ production at $\sqrt{s} = 13$ TeV [203].

Eqs. (19)–(22) are taken as a boundary condition for the QCD evolution equations, which define the PDFs in the whole kinematical region of the data analyzed. The parameters N_q^v and A_g are determined from the sum rules for fermion number and momentum conservation, respectively, and A_{qs}, a_{qs}, b_{qs}, γ_{qs} are fitted to the data. The functional form in Eqs. (19)–(22) provides sufficient flexibility over the entire x range with respect to the combined data within the ABMP16 analysis. We have checked that the quality of the fit does not improve when

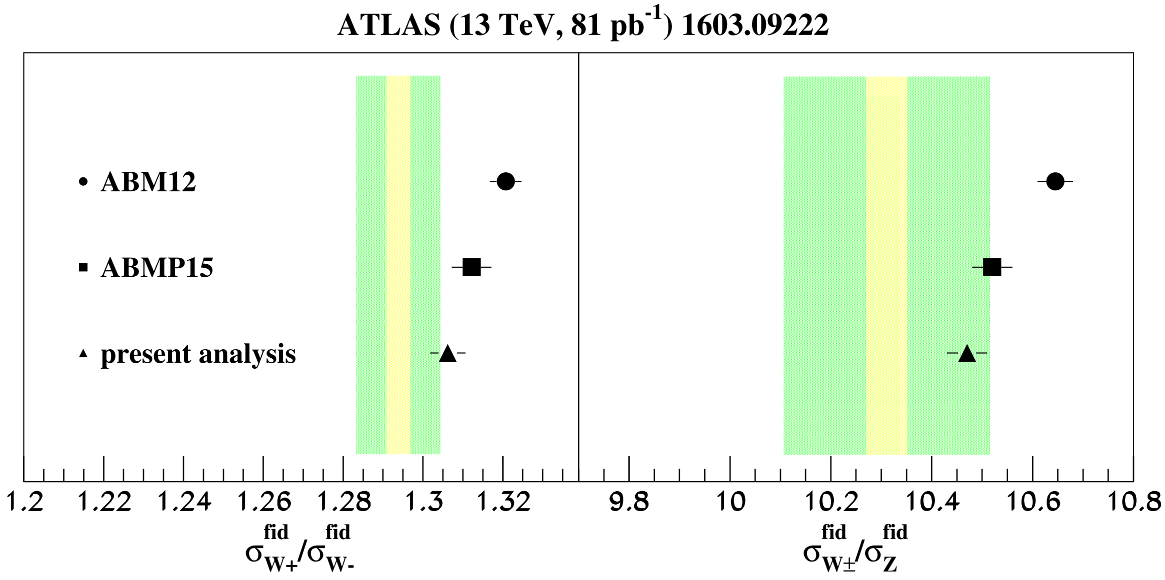

FIG. 13. Cross section ratios for the production of $W^\pm$- and Z-bosons in the fiducial volume, $\sigma_{W^+}/\sigma_{W^-}$ (left) and $\sigma_{W^\pm}/\sigma_Z$ (right), in comparison to ATLAS data [26] at $\sqrt{s} = 13$ TeV together with their 1σ PDF uncertainties using the results of our NNLO fit (triangles) as well as ABM12 [1] (circles) and ABMP15 [3] (squares). The inner (yellow) band denotes the statistical uncertainty of the ATLAS data [26] and the outer (green) one the combined uncertainty due to statistics and systematics. The ABM12 predictions are larger than the ones presented in Ref. [26] due to different programs used, `FEWZ` (version 3.1) [181,182] and `DYNNLO` (version 1.5) [204,205], respectively.

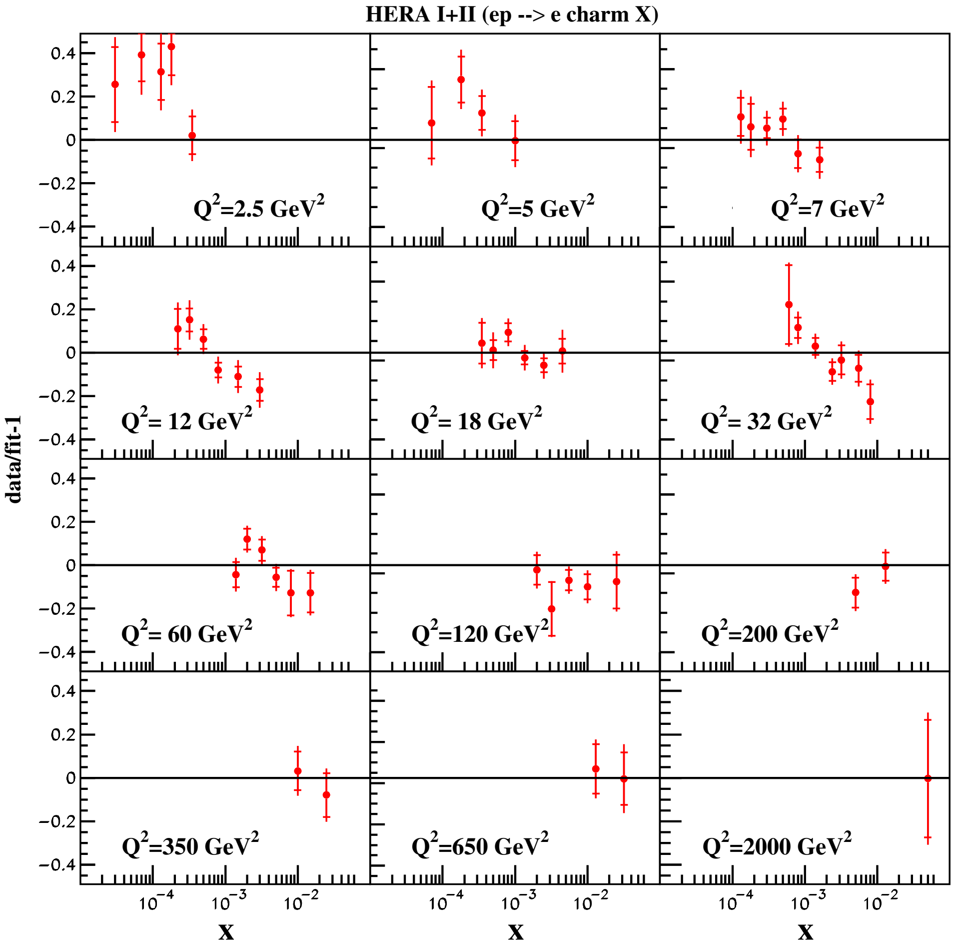

FIG. 14. The same as in Fig. 4 for the NC DIS inclusive charm-quark production data [63] versus Bjorken x in bins of the momentum transfer Q^2.

allowing for additional terms in Eq. (22). The parameter values obtained with their 1σ uncertainties corresponding to the statistical and systematic errors in the data are given in Table VII. The respective correlations are listed in Appendix B.

A representative comparison of the PDFs obtained in the present analysis with our earlier ABM12 and ABMP15 parametrizations demonstrates the recent improvements and is given in Figs. 18 and 19.[4] In particular, the DY data added to the fit extend the range of x values probed and, being complementary to the DIS sample used, help to disentangle quark distributions at small and large x. This mainly improves the accuracy of the down-quark distribution, which is commonly determined from a combination of the data on DIS off proton and deuteron targets. As detailed in Sec. II A, the down- and up-quark distributions in the present analysis are separated by using a combination of data on electron-proton DIS together with those on $W^{\pm}$- and Z-production in (anti)proton-proton collisions. In consequence, the deuteron data from DIS fixed-target experiments are not used anymore, which eliminates any errors related to the modeling of nuclear effects in deuterium in the ABMP16 analysis.

The d/u ratio obtained in this way is comparable with our earlier ABM12 determination within uncertainties. At $x \lesssim 0.4$ its accuracy is improved due to the impact of the DY LHC data in the central-rapidity region while it is comparable to the one obtained in the ABM12 analysis for $x \gtrsim 0.4$. The central values of the d/u ratio obtained in both cases basically agree within the errors. This proves that the nuclear corrections on the basis of the Kulagin-Petti model [207,208] employed in the ABM12 analysis provide a consistent treatment [209]. The enhanced statistical potential of the DY data also appears in disentangling the light-quark PDFs at small x. The parametrization Eq. (20) allows for nonzero values of the sea iso-spin asymmetry $I(x) = x[\bar{d}(x) - \bar{u}(x)]$ at small x, in contrast to the ABM12 one, which was based on the Regge-like asymptotic of $I(x) \sim x^{0.7}$. By releasing the Regge-like constraint on $I(x)$ we find that negative values at $x \sim 10^{-4}$ are preferred

---

[4] The plots are generated in the `xFitter` framework [206] using our PDFs grids in the format of the `LHAPDF` library (version 6) [14], cf. Sec. IV D.

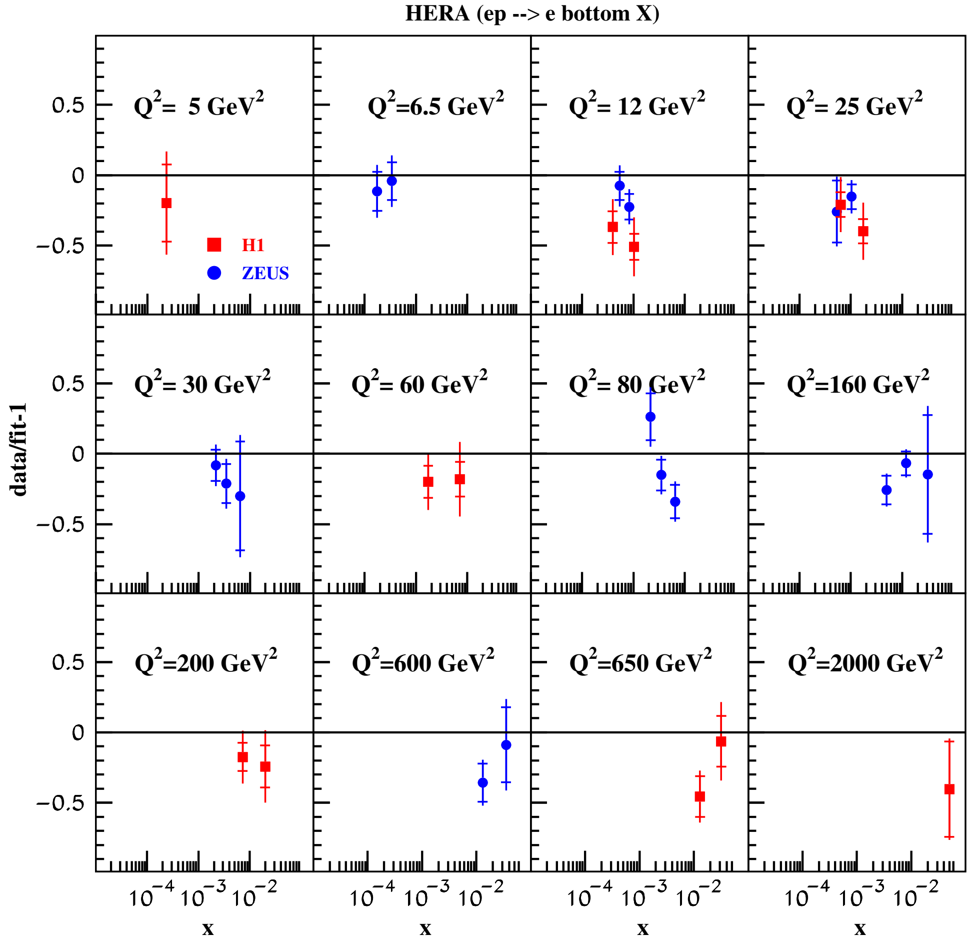

FIG. 15. The same as Fig. 14 for the NC DIS inclusive bottom-quark production data from the H1 [15] (squares) and ZEUS [16] (circles) Collaborations at HERA.

by the data, while a turnover in its shape is observed at $x \lesssim 10^{-4}$. Therefore $I(x)$ may still be comparable with zero at smaller values $x \sim 10^{-6}$.

The strange sea distribution is traditionally determined by data on charm production in the neutrino-induced DIS. In the present analysis, we extend this sample with the measurements performed by the NOMAD and CHORUS experiments, cf. Table II. This allows to improve the accuracy of the strange sea in a wide range of x, particularly due to the NOMAD data, which probe the range of $x \approx 0.02 \div 0.75$. The newly added data on the $W^\pm$- and Z-boson production also help to disentangle the strange sea because of their particular contribution to the NC and CC processes. This improvement concerns mainly the small-x region, which is poorly constrained by the existing fixed-target DIS data. As a result we obtain a continuous improvement in the accuracy of the strange sea at small-x from the ABM12 to the ABMP15 PDFs and further to the present analysis due to the gradual increase in the statistical significance of the DY data sample used in those fits. Furthermore, the central value of the small-x strange sea distribution is larger compared to the ABM12 one and comes into agreement with the ATLAS results based on a QCD analysis of their own data on the $W^\pm$- and Z-production in combination with the HERA inclusive DIS ones [66,210]. However, at $x \gtrsim 0.01$ we still observe a suppression of the strange sea as compared to the non-strange one by factor of ~0.5. This finding is in contrast to the results [66,210] which claim SU(3) universality of the light-quark PDFs over a wide range of x. The difference of our analysis with Refs. [66,210] is evidently correlated with the difference in the obtained iso-spin asymmetries $I(x)$. For the ATLAS determination $I(x)$ is negative at $x \sim 0.1$, while in our case $I(x)$ is positive as suggested by the fixed-target DY data of the Fermilab E-866 experiment [69] included into the fit. Therefore, a consolidation of our results with those of ATLAS would require a critical appraisal of the E-866 results. This issue can be also reconciled in the future by measuring the associated $W + c$ production in proton-proton collisions at the LHC. The existing ATLAS [211] and CMS [212] data somewhat overshoot the theory predictions at NLO in QCD based on our PDFs [2]. However, the discrepancy is well within the experimental uncertainties and, moreover,

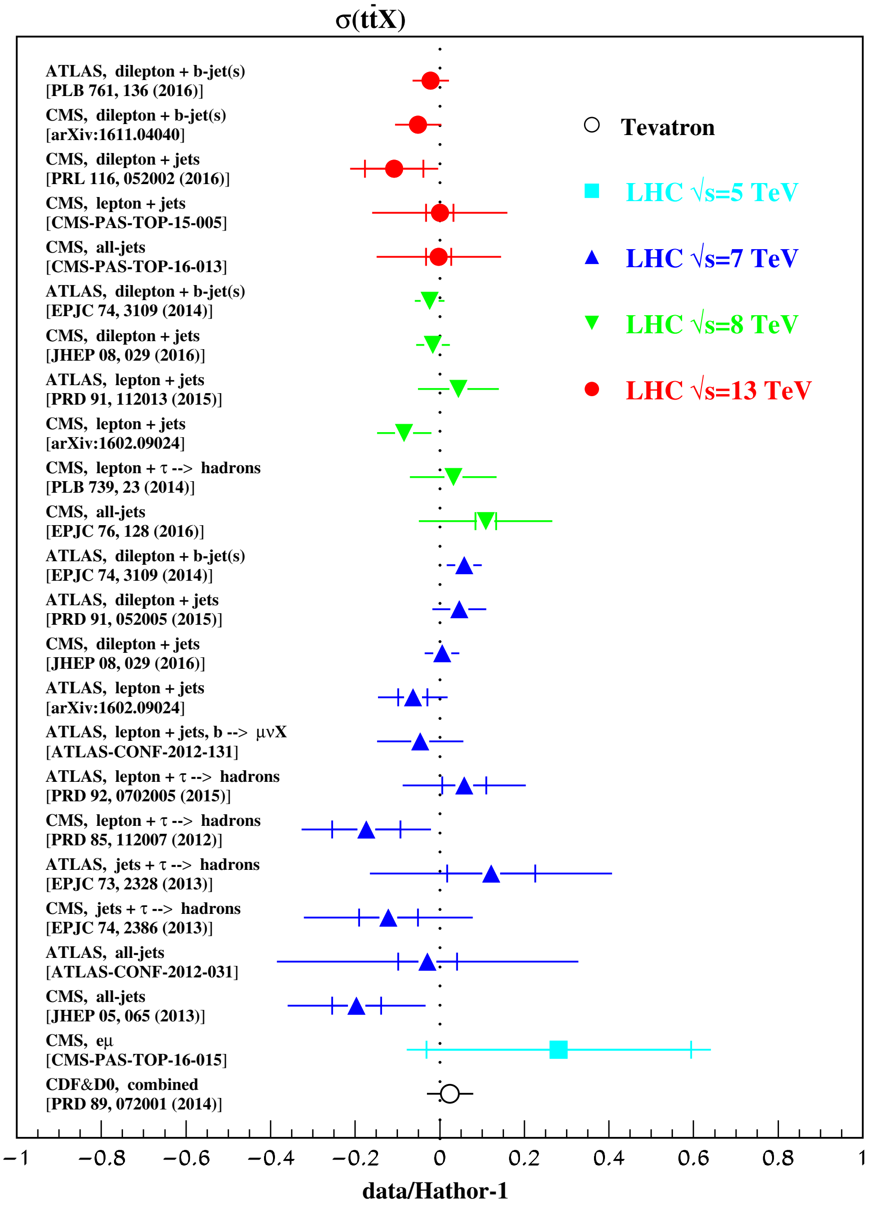

FIG. 16. The pulls for data on top-quark pair production from the Tevatron (CDF and DØ Collaborations) at $\sqrt{s} = 1.96$ TeV and the LHC (ATLAS and CMS Collaboration) at $\sqrt{s} = 5$, 7, 8 and 13 TeV with respect to our NNLO fit. The NNLO QCD predictions have been obtained with `Hathor` [189].

might vanish once QCD corrections at NNLO accuracy become available.

The data of Tables III and IV on hadronic t-quark production employed in the present analysis provide additional constraints on the PDFs, in particular on the gluon distribution at large x. Due to this new input the latter increases at $x \gtrsim 0.1$ by 10–20%, depending on the factorization scale, which is well within its uncertainty, cf. Fig. 20. Here, the data on $t\bar{t}$-production play a major role since the production process is mostly driven by initial state gluons.

It is well known that the uncertainty in the gluon distribution decreases as the factorization scale increases. This happens because the large-scale gluon PDF receives also sizable contributions from the quark PDFs during the QCD evolution in the singlet sector due to the splitting function P_{gq}. In this way, the large-x/large-scale gluon PDF benefits from an accurate determination of large-x quark PDFs. The latter, in turn, are well constrained by the DIS and DY data used in the present analysis. This peculiar feature is illustrated in Fig. 21. We compare the response of the gluon distribution when evolved to a large scale of $\mu = 20$ TeV to a model suppression of the gluon and up-quark PDFs by factor of $(1 - x)$ at the initial scale of the evolution. Indeed, as Fig. 21 shows, the sensitivity of the large-scale gluon PDF to its modification at the initial scale

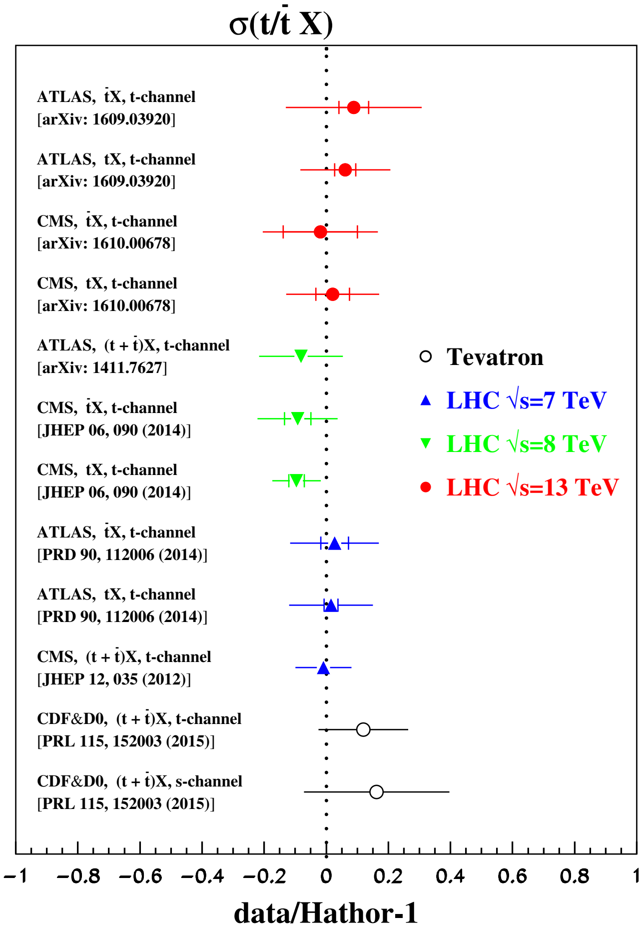

FIG. 17. The same as Fig. 16 for data on single-top production in the s- and t-channel for final states with t- and $\bar{t}$-quarks. The approximate NNLO QCD predictions have been computed with `Hathor` [199] as described in Sec. II B.

is marginal. If, however, the up-quark distribution is modified by the factor $(1-x)$ at the initial scale, this suppression is basically reproduced by the gluon PDF at $\mu = 20$ TeV. The large-scale sea-quark distributions are also sensitive to modifications of the quark PDFs at small scales, although to a lesser extent. In this case, the effect originates from a two-step process in the singlet sector during evolution due to the splitting function P_{qg} acting on the modified gluon PDF. Such an interplay is especially pronounced at big scales which are currently explored in searches for potential new effects beyond the Standard Model.

A comparison of the PDFs determined in the present analysis with other available PDF sets at the scale of the Z-boson mass squared, M_Z^2, is presented in Figs. 22–25. The discrepancies observed appear mainly due to differences in the data sets and in the theoretical framework used, in particular for the description of the heavy-quark NC DIS production, cf. Ref. [11]. Firstly, the up- and down-quark distributions in the present analysis exhibit an improved precision as a result of employing the latest DY and DIS data samples. Consequently, these distributions have typically smaller uncertainties compared to other PDFs, which do not yet use all currently available DY and DIS data. In part, due to this improvement, as we discuss above, the ABMP16 gluon distribution, now also constrained by the t-quark data from LHC, has overall smaller uncertainties as compared with other PDFs, although their central values are typically bigger(smaller) than ours at $x \gtrsim 0.1 (\lesssim 0.1)$. The sea-quark iso-spin asymmetry $I(x)$ is in a good agreement with the CT14 and NNPDF3.0 PDFs, the latter having largest uncertainties at low x. In contrast, for the MMHT14 and JR14 PDFs the same distribution is vanishing, i.e., $I(x) \simeq 0$, at low x due to possible restrictions in the chosen parametrization. Also the HERAPDF2.0 result for $x(\bar{d}-\bar{u})$ indicates a different shape at $x \gtrsim 0.01$ due to the fact that only HERA data are used in fitting those PDFs. However, the difference is covered by the large uncertainty in this distribution. Finally, the improved s-quark distribution due to the latest precise NOMAD [17] and CHORUS [18] data is generally in good agreement with all PDFs with the exception of HERAPDF2.0 which, as mentioned before, is determined solely from HERA data which constrain strange sea quarks only weakly.

C. Higher twist

We parametrize the coefficients $H_i^{\tau=4}$ for $i = 2, T$ of the higher twist (HT) terms in the DIS nucleon structure functions F_i in Eq. (6) as follows

$$H_i^{\tau=4}(x) = x^{\alpha_i} S_i(x), \quad i = 2, T, \tag{23}$$

TABLE VII. The fitted PDF parameters Eqs. (19)–(22) and their 1σ errors due to statistical and systematic uncertainties in the data.

	a	b	γ_{-1}	γ_1	γ_2	γ_3	A
u_v	0.623 ± 0.033	3.443 ± 0.064		-0.22 ± 0.33	-2.88 ± 0.46	2.67 ± 0.80	
d_v	0.372 ± 0.068	4.47 ± 0.55		-3.20 ± 0.77	-0.61 ± 1.96	0 ± 0.001[a]	
u_s	-0.415 ± 0.031	7.75 ± 0.39	0.0373 ± 0.0032	4.44 ± 0.95			0.0703 ± 0.0081
d_s	-0.17 ± 0.011	8.41 ± 0.34		13.3 ± 1.7			0.1408 ± 0.0076
s_s	-0.344 ± 0.019	6.52 ± 0.27					0.0594 ± 0.0042
g	-0.1534 ± 0.0094	6.42 ± 0.83		-11.8 ± 3.7			

[a] This parameter is poorly determined from the fit. Therefore its variation is constrained within the range $\gamma_{3,d} \in [-0.001, 0.001]$.

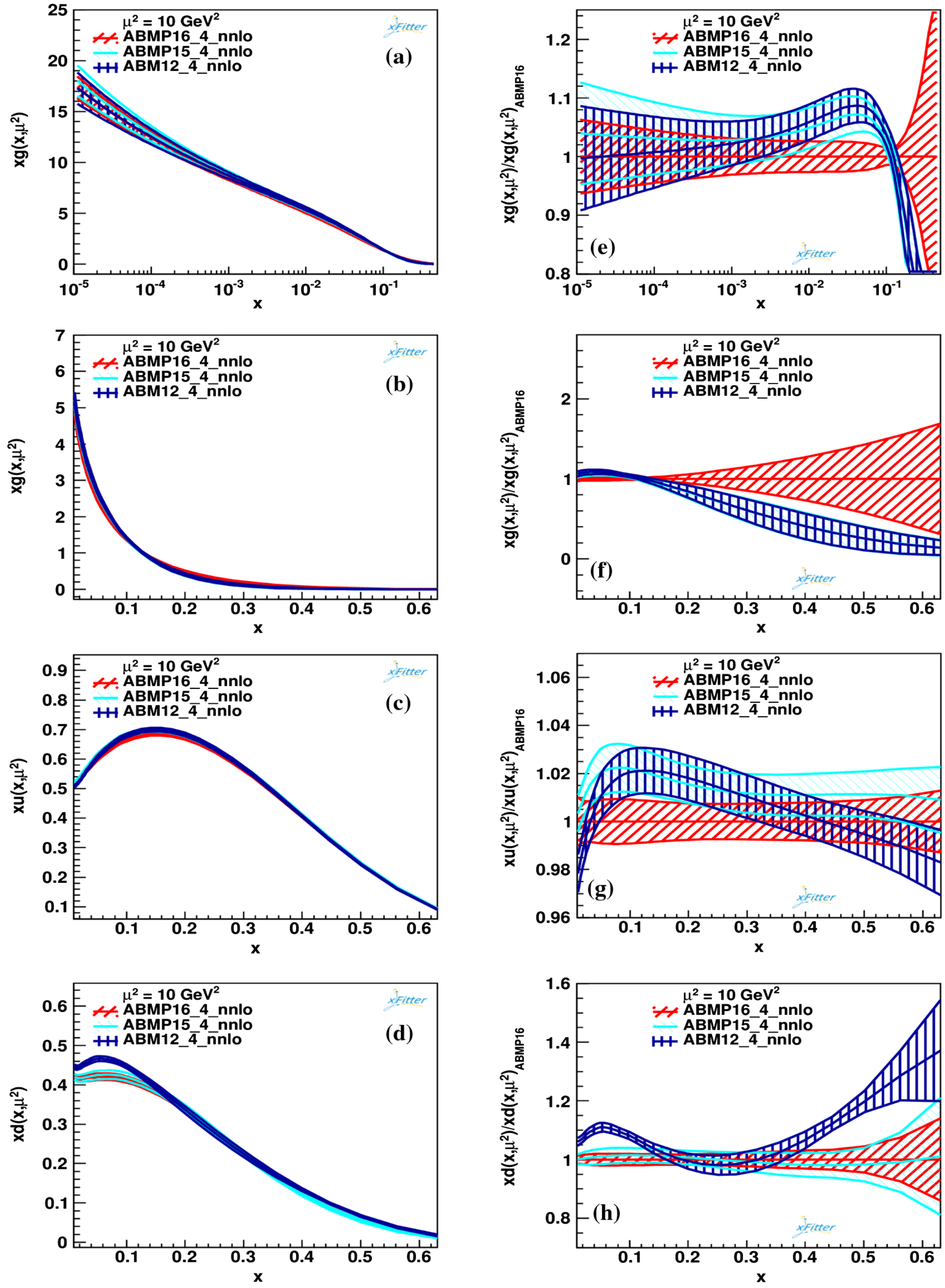

FIG. 18. The distributions of $n_f = 4$ flavor gluons $xg(x,\mu^2)$ (a: logarithmic x scale, b: linear x scale), up-quarks $xu(x,\mu^2) = x[u_v(x,\mu^2) + u_s(x,\mu^2)]$ (c) and down-quarks $xd(x,\mu^2) = x[d_v(x,\mu^2) + d_s(x,\mu^2)]$ (d) with their 1σ uncertainties at the factorization scale $\mu^2 = 10$ GeV^2 versus x for NNLO ABMP16 (right-tilted hatched), ABMP15 [3] (left-tilted hatched) and ABM12 [1] (vertical hatched) PDFs in the $n_f = 4$ flavor scheme. The same distributions normalized to the central ABMP16 values are given for comparison (e–h).

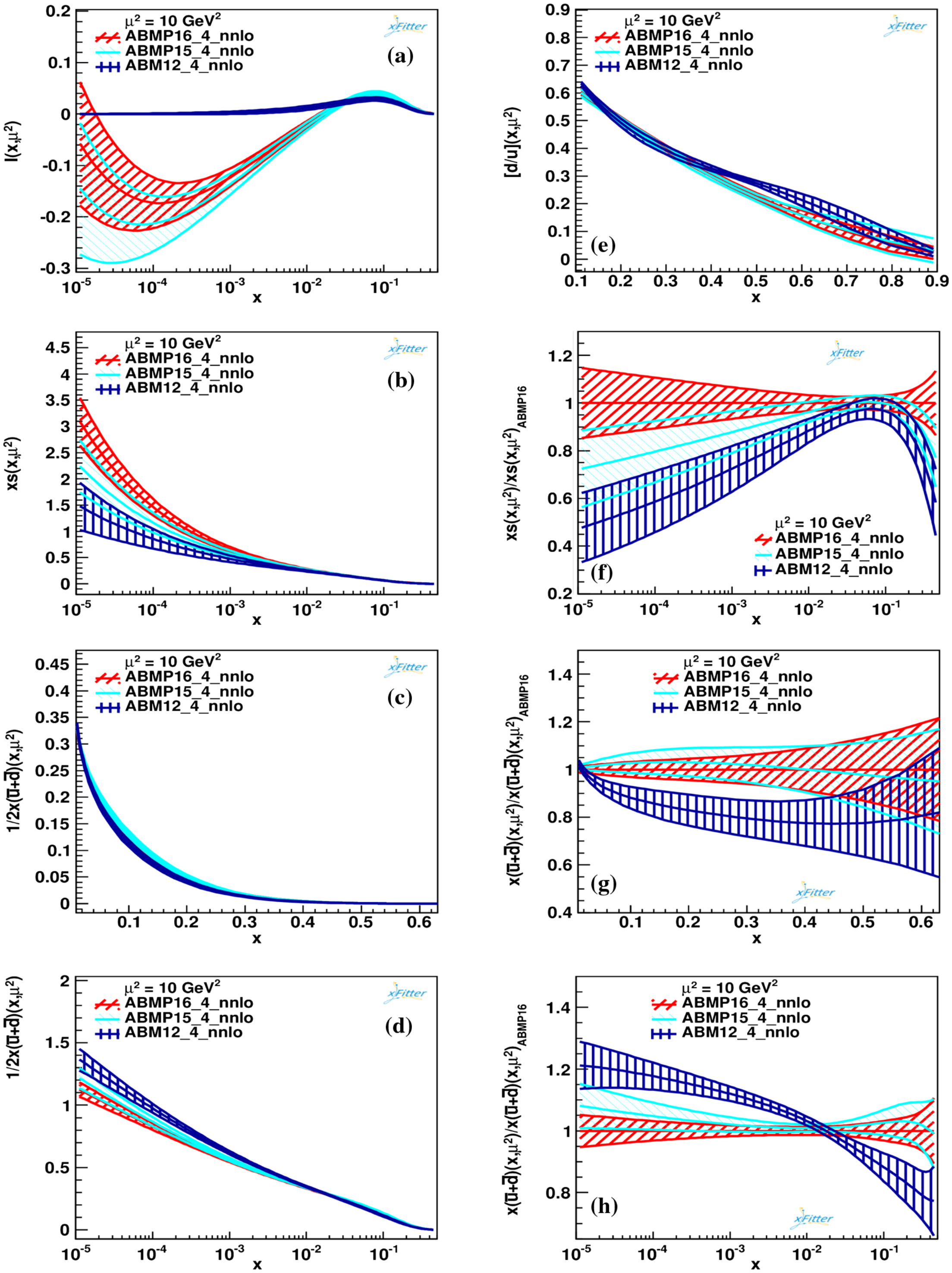

FIG. 19. The same as in Fig. 18 for the sea-quark iso-spin asymmetry $I(x,\mu^2) = x[\bar{d}_s(x,\mu^2) - \bar{u}_s(x,\mu^2)]$ (a), symmetrized strange sea $s(x,\mu^2) = [s_s(x,\mu^2) + \bar{s}_s(x,\mu^2)]/2$ (b), the nonstrange sea $[x(\bar{u}+\bar{d})/2](x,\mu^2) = x[\bar{u}_s(x,\mu^2) + \bar{d}_s(x,\mu^2)]/2$ (c: linear x scale, d: logarithmic x scale), and the ratio $[d/u](x,\mu^2) = [d_v(x,\mu^2) + d_s(x,\mu^2)]/[u_v(x,\mu^2) + u_s(x,\mu^2)]$ (e). The distributions of strange sea $s(x,\mu^2)$ (f) and the nonstrange sea $[x(\bar{d}+\bar{u})/2](x,\mu^2)$ (g: linear x scale, h: logarithmic x scale) normalized to the central ABMP16 values are given for comparison.

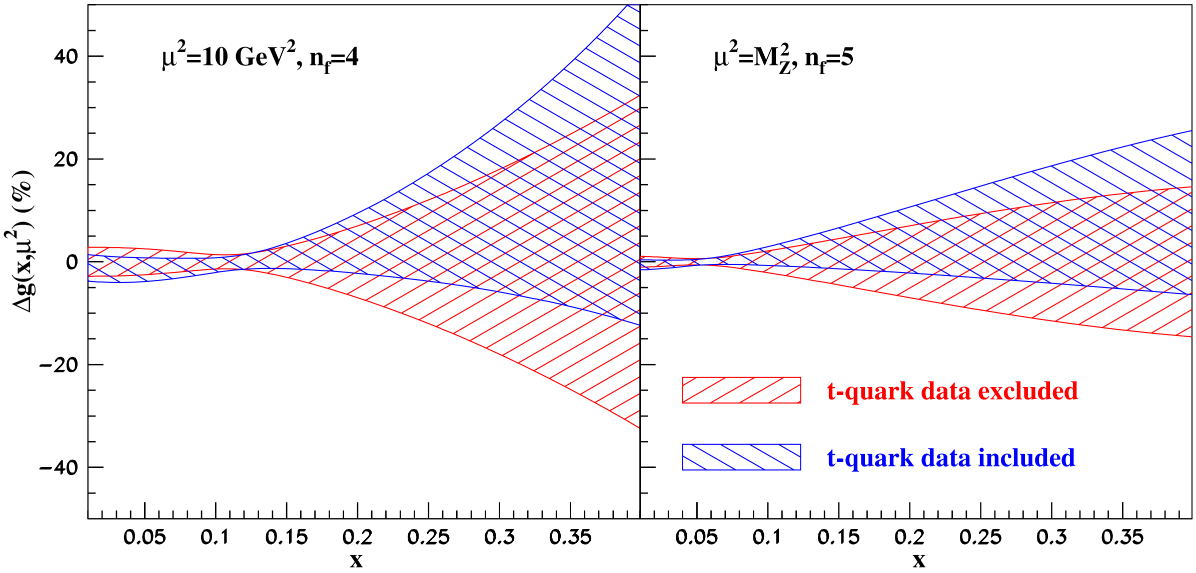

FIG. 20. The 1σ relative uncertainty for the $n_f = 4$ flavor gluon distribution at the factorization scale $\mu^2 = 10\ \mathrm{GeV}^2$ (left panel) and for the $n_f = 5$ flavor gluon distribution at the factorization scale $\mu^2 = M_Z^2$ (right panel). The nominal fit of the present analysis (left-tilted hatched) is compared to a variant where the t-quark data of Tables III and IV has been excluded (right-tilted hatched).

where $S_i(x)$ are the cubic splines defined at the knots $\{[x_k, H_i^{\tau=4}(x_k)]\colon k = 1, 7\}$ and $\{x_k\} = (0, 0.1, 0.3, 0.5, 0.7, 0.9, 1)$. The constraint $H_i^{\tau=4}(1) = 0$ is imposed due to poor coverage of the region of $x \to 1$ by the existing data. The remaining knot values $H_i^{\tau=4}(x_k)$ for $k = 1, \ldots, 6$ are taken as fit parameters and the result of the fit with Eq. (23) is presented in Table VIII and Fig. 26.

A particular benefit of the present analysis is the possibility to study the small-x shape of the HT terms due to the improved statistical significance of the inclusive HERA run I + II data. With this input we find a sizeable deviation of $H_T^{\tau=4}$ from 0 at small x. The small-x shape of $H_i^{\tau=4}$ is controlled by the combination of the NMC and HERA data. Both data sets prefer a negative value of $H_T^{\tau=4}$ at small x, as we find in the variants of our analysis when either the NMC or the HERA data set is dropped. A similar check for the HERA run I data [213] demonstrates that the small-x value of $H_T^{\tau=4}$ is significantly bigger than the one preferred by the HERA run I + II data, although both are comparable within the uncertainties. Nonetheless, for this

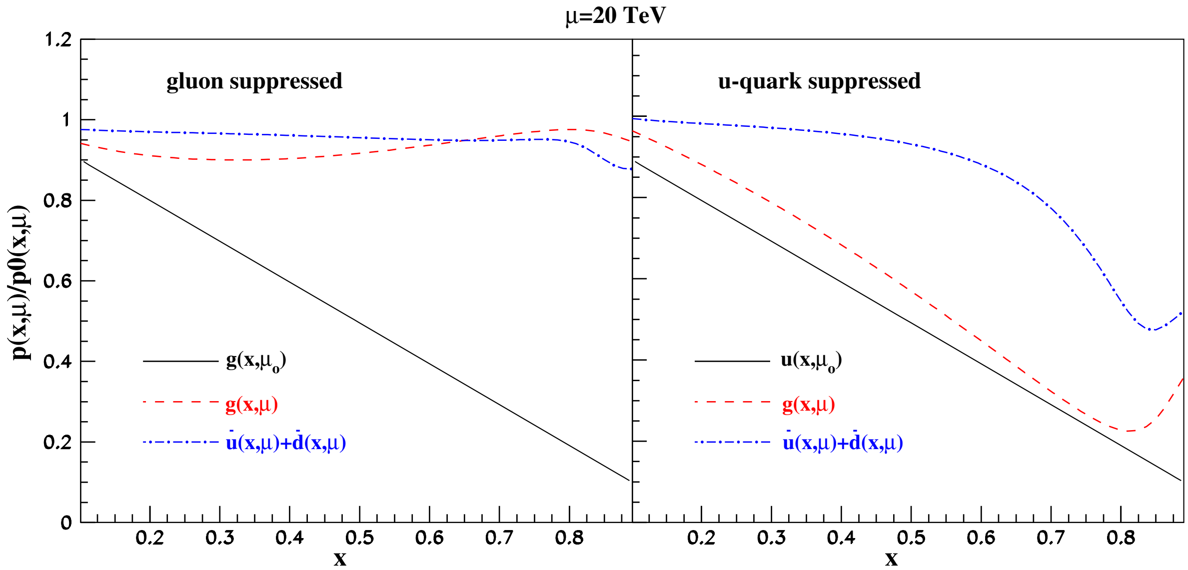

FIG. 21. A response of the gluon (dashes) and nonstrange sea (dashed dots) distributions evolved from the factorization scale $\mu_0 = 3$ GeV to $\mu = 20$ TeV to the suppression of the initial gluon distribution $g(x, \mu_0)$ (left panel) and up-quark distribution $u(x, \mu_0)$ (right panel) by a factor of $(1 - x)$ (solid lines) given as a ratio of PDFs $p(x, \mu)$ and $p0(x, \mu)$ with and without suppression, respectively.

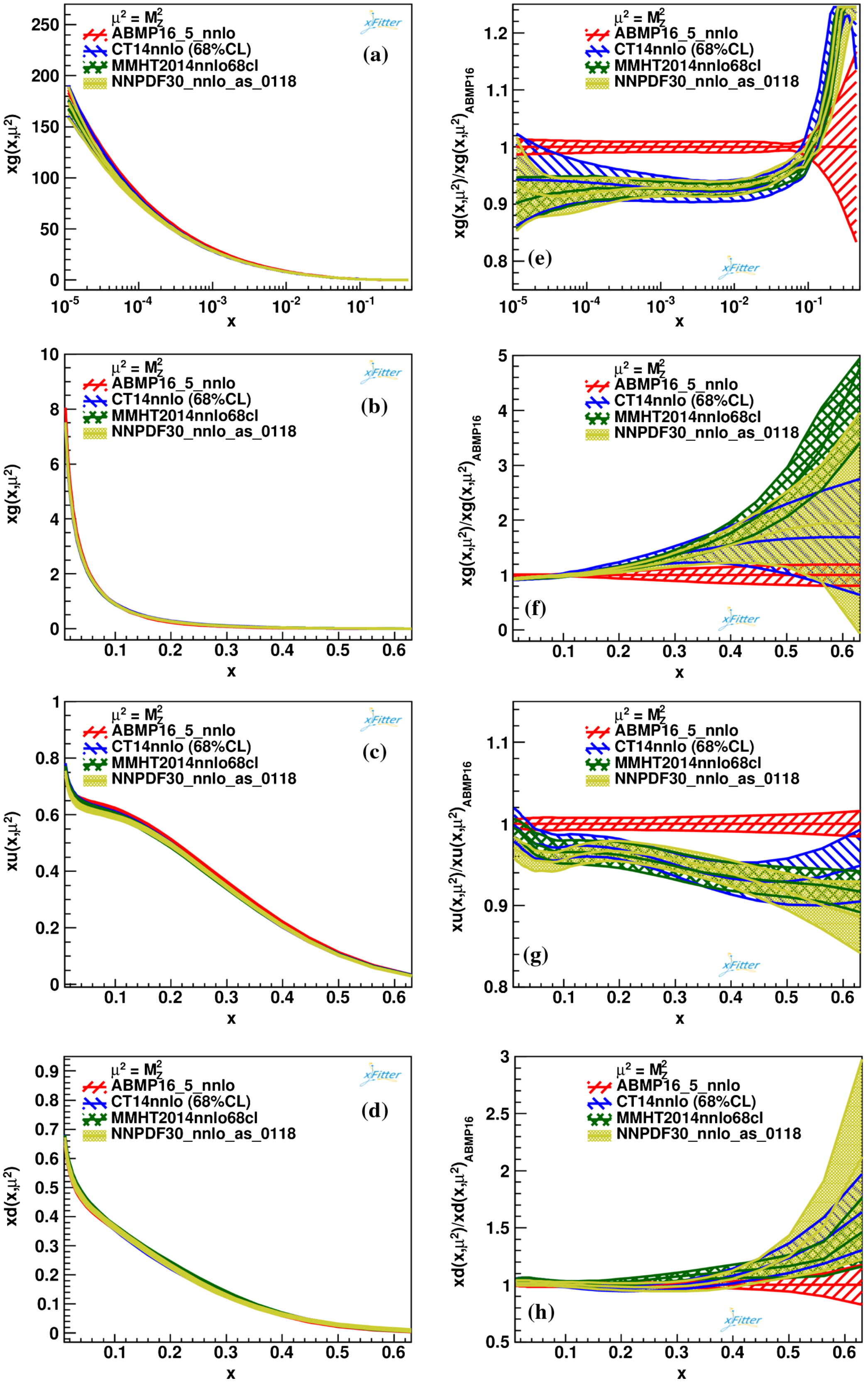

FIG. 22. The same as in Fig. 18 for the absolute values of the $n_f = 5$ flavor ABMP16 (right-tilted hatched), CT14 [7] (left-tilted hatched), MMHT14 [9] (left-right tilted hatched) and NNPDF3.0 [10] (shaded area) PDFs at the factorization scale $\mu^2 = M_Z^2$.

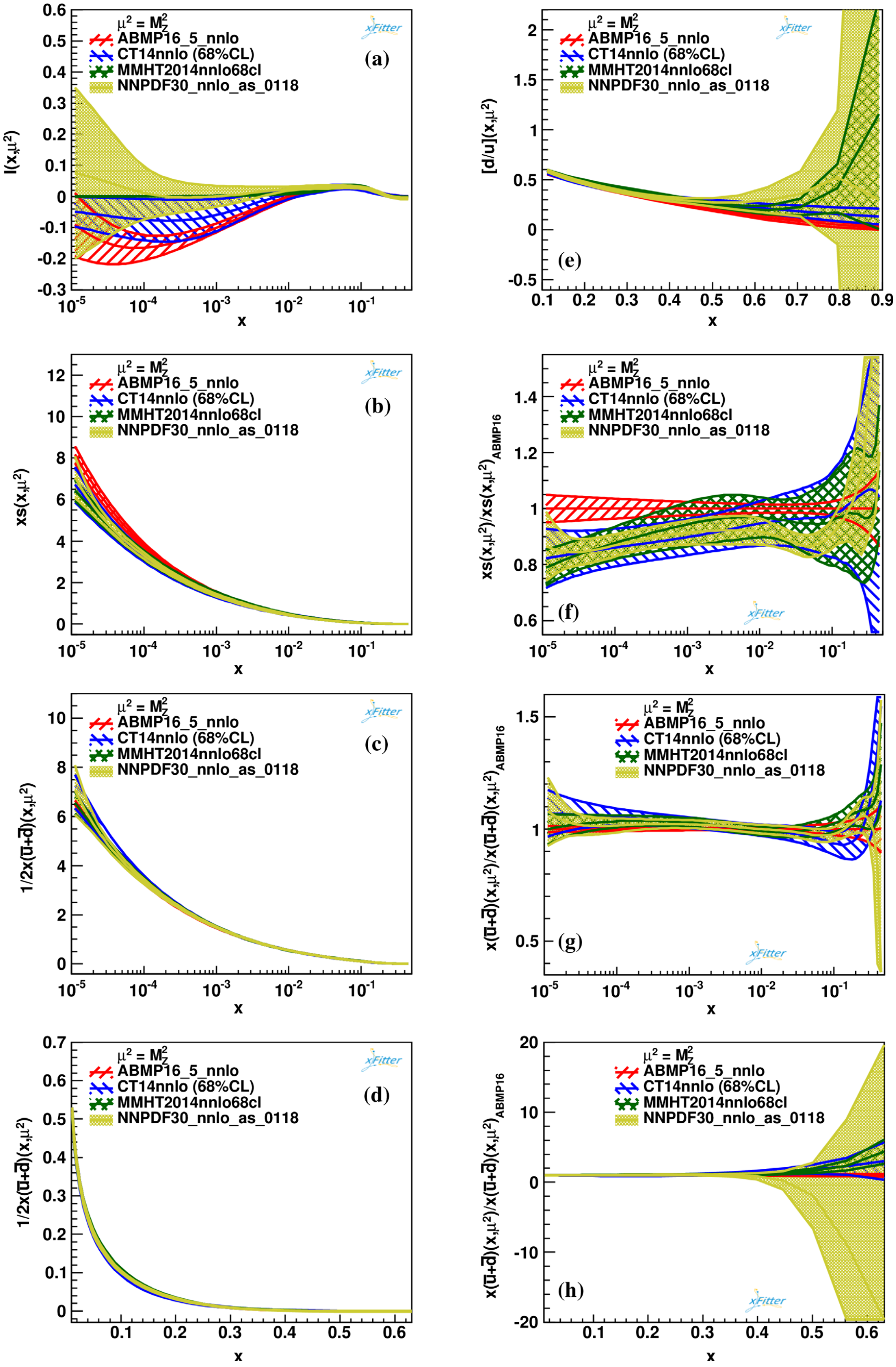

FIG. 23. The same as in Fig. 19 for the absolute values of the $n_f = 5$ flavor ABMP16 (right-tilted hatched), CT14 [7] (left-tilted hatched), MMHT14 [9] (left-right tilted hatched) and NNPDF3.0 [10] (shaded area) PDFs at the factorization scale $\mu^2 = M_Z^2$.

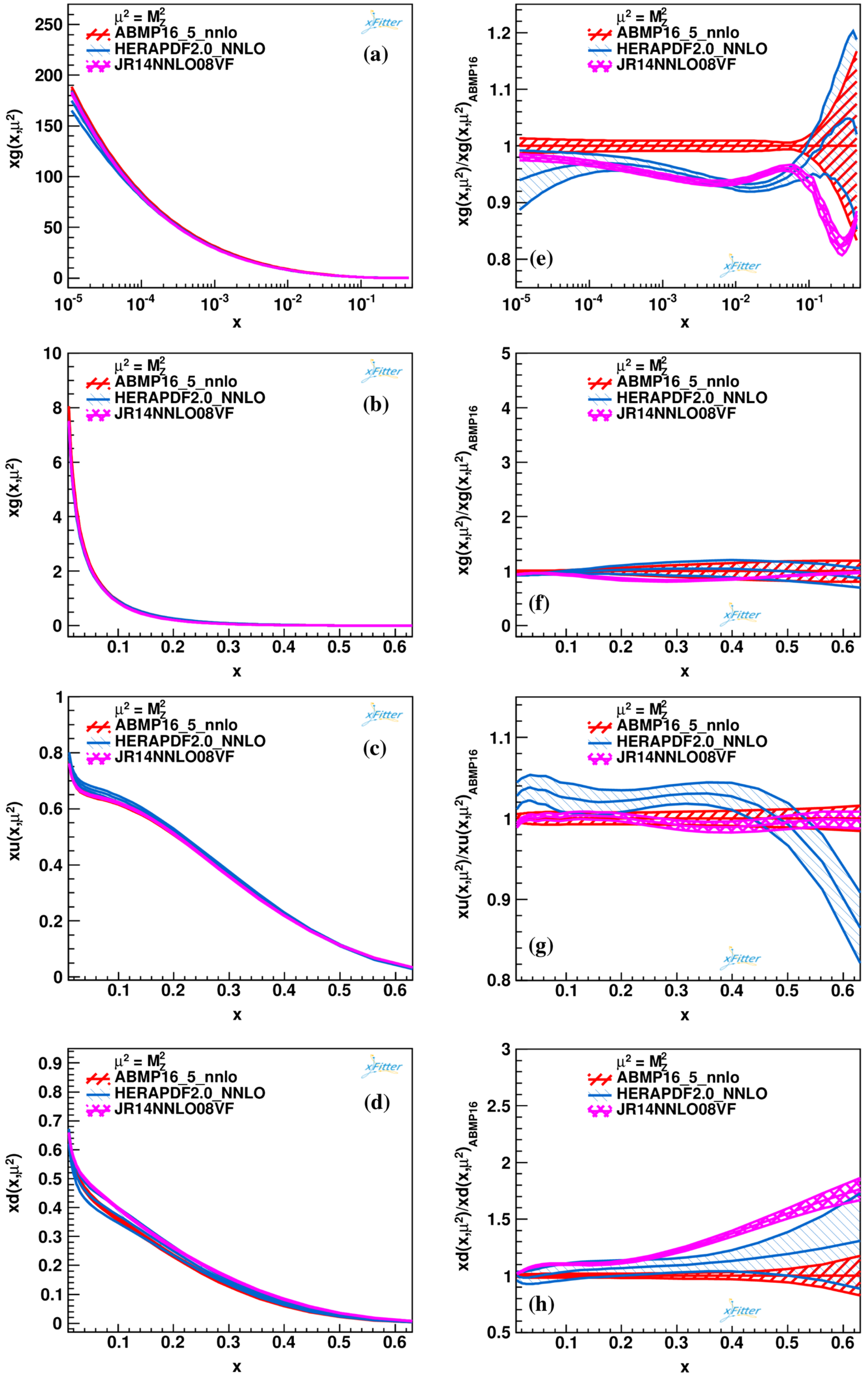

FIG. 24. The same as in Fig. 18 for the absolute values of the $n_f = 5$ flavor ABMP16 (right-tilted hatched), HERAPDF2.0 [4] (left-tilted hatched) and JR14 [8] (left-right tilted hatched) PDFs at the factorization scale $\mu^2 = M_Z^2$.

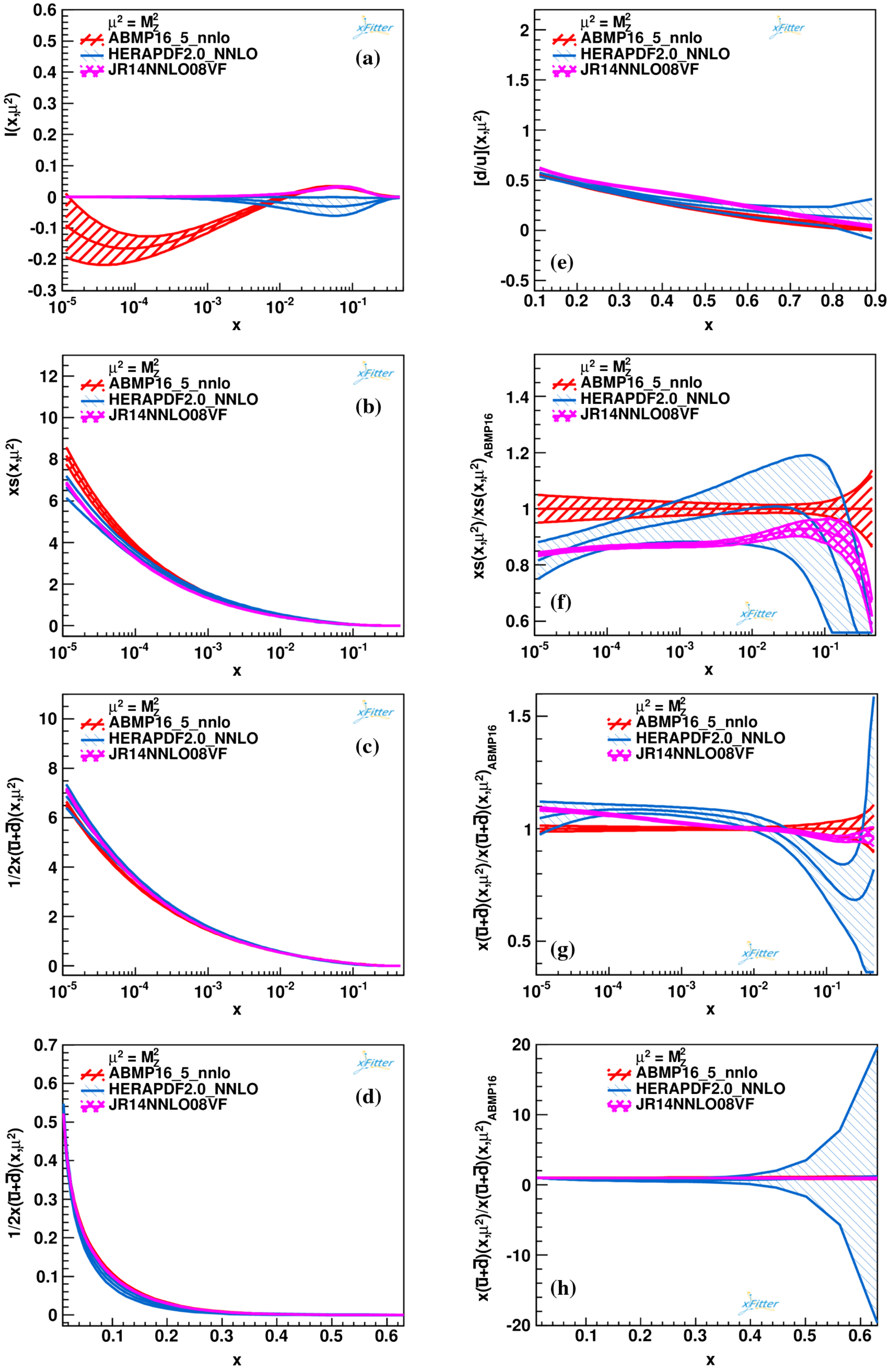

FIG. 25. The same as in Fig. 19 for the absolute values of the $n_f = 5$ flavor ABMP16 (right-tilted hatched), HERAPDF2.0 [4] (left-tilted hatched) and JR14 [8] (left-right tilted hatched) PDFs at the factorization scale $\mu^2 = M_Z^2$.

TABLE VIII. The knots of the twist-4 splines $S_{2,T}(x)$ in Eq. (23) obtained in the present analysis.

	$H_2^{\tau=4}(x)/\text{GeV}^2$	$H_T^{\tau=4}(x)/\text{GeV}^2$
$x = 0.0$	0.023 ± 0.019	-0.319 ± 0.126
$x = 0.1$	-0.032 ± 0.013	-0.134 ± 0.040
$x = 0.3$	-0.005 ± 0.009	-0.052 ± 0.030
$x = 0.5$	0.025 ± 0.006	0.071 ± 0.025
$x = 0.7$	0.051 ± 0.005	0.030 ± 0.012
$x = 0.9$	0.003 ± 0.004	0.003 ± 0.007
$x = 1$	0	0

reason the ABMP16 HT terms are different from the earlier ABM12 determination of the HT terms based on the HERA run I data, which where consistent with zero at small x [1]. For larger values $x \gtrsim 0.1$, both results, ABMP16 and ABM12 agree with each other.

The value of the small-x exponent $\alpha_T = 0.05 \pm 0.07$ found in the fit defines a shallow falloff of $H_T^{\tau=4}$ at $x \to 0$, see Fig. 26. However, its statistically significant deviation from zero persists down to $x \sim 10^{-5}$. At the same time, the fitted value of $H_2^{\tau=4}$ is comparable to zero at small x. Therefore, the constraint $\alpha_2 = 0$ is imposed. This results in a sizeable contribution of the HT terms to the structure function F_L at small x and Q^2, cf. Fig. 27. The excess in F_L due to the HT found in [121] is more essential than the one observed in our case. This might be explained by the particular parametrization of the HT terms assumed in Ref. [121] and discussed in Sec. II B 2, which implies a strong effect of the QCD evolution on the small-x HT terms. In our analysis, such an effect does not appear.

The interplay between the leading twist and the HT terms is essential for the determination of the PDFs. To illustrate this, we consider two variants of our analysis when no HT terms are taken into account and more stringent kinematic cuts are imposed on the inclusive DIS data as follows

$$Q^2 > 2.5\ \text{GeV}^2, \qquad W^2 > 12.5\ \text{GeV}^2, \tag{24}$$

and

$$Q^2 > 10\ \text{GeV}^2, \qquad W^2 > 12.5\ \text{GeV}^2, \tag{25}$$

where Q^2 is the momentum transferred squared and W denotes the invariant mass of the hadronic system, cf. Eq. (3). The gluon distributions obtained in these three fits are compared in Fig. 28. In the case of the cut in Eq. (24), the gluon PDF increases by 1σ compared to our nominal one. Moreover, the central value differs by up to 50% at $x < 0.5$. For the fit with the cut in Eq. (25) the difference is twice smaller. This means, that the HT contribution cannot be eliminated by the commonly used cut of $W^2 > 12.5\ \text{GeV}^2$ and that the HT terms are still substantial in the region of $Q^2 = 2.5 \div 10\ \text{GeV}^2$; see also Refs. [1,215].

D. The strong coupling constant

In the present analysis, the value of the strong coupling constant α_s is fitted simultaneously with the leading-twist PDFs and the twist-four terms. The DIS and $t\bar{t}$-production data sets play the most important role in this determination. To study the particular significance of these two samples we consider a variant of the present analysis without the t-quark data included. In this case, the value of

$$\alpha_s^{(n_f=5)}(M_Z) = 0.1145 \pm 0.0009 \tag{26}$$

at NNLO in QCD for the scheme with $n_f = 5$ light flavors is obtained. This value is basically defined by the data from

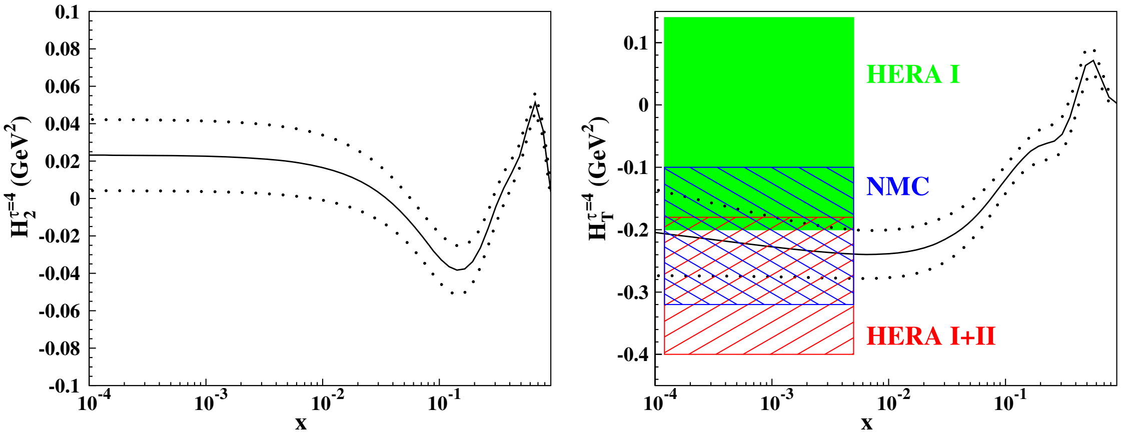

FIG. 26. The coefficients $H_2^{\tau=4}$ (left) and $H_T^{\tau=4}$ (right) in the higher twist terms of the inclusive DIS structure functions, cf. Eq. (6), as a function of x. Shown are the central values (solid) and the 1σ bands (dots). The boxes at $x \lesssim 5 \times 10^{-3}$ display the low-x asymptotic of $H_T^{\tau=4}$ preferred by the individual data sets indicated (right-tilted hatched: combined HERA run I + II [4], left-tilted hatched: NMC [60], shaded: combined HERA run I [213]).

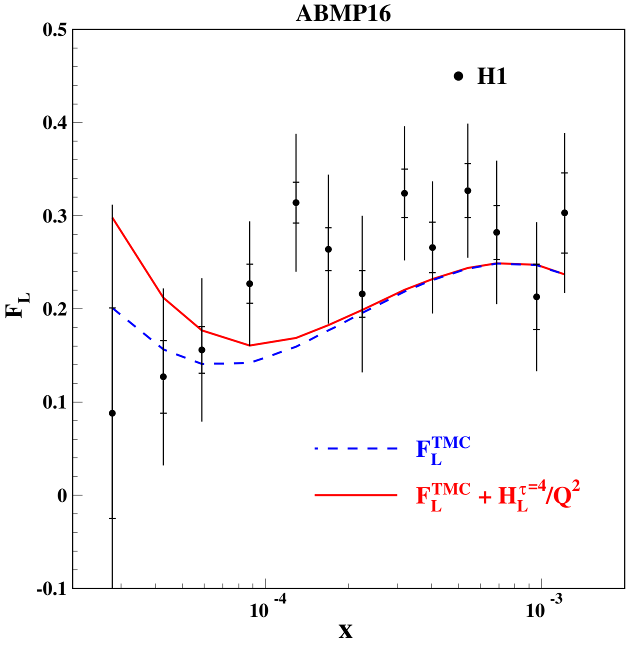

FIG. 27. The data on the longitudinal structure functions F_L as a function of x by the H1 Collaboration at HERA [214] compared to the predictions of our analysis at NNLO in QCD based on either including higher twist terms (solid) or setting them to zero (dashes), cf. Eq. (6).

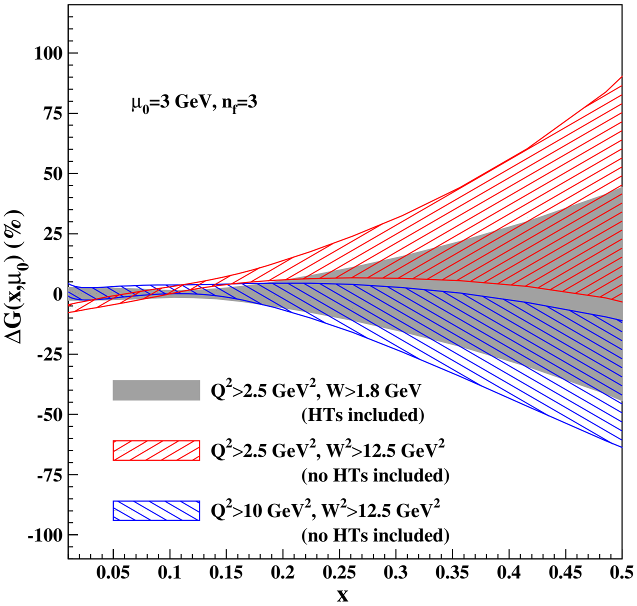

FIG. 28. The 1σ relative uncertainty in the $n_f = 3$ flavor gluon distribution at the starting scale of the QCD evolution $\mu_0 = 3$ GeV obtained in the present analysis with the HT terms taken into account and the cuts of $Q^2 > 2.5$ GeV^2 and $W > 1.8$ GeV imposed on the inclusive DIS data (shaded area). In comparison, two variants of the analysis with no HT taken into account and the cuts of $Q^2 > 2.5$ GeV^2 and $W^2 > 12.5$ GeV^2 (right-tilted hatched) and $Q^2 > 10$ GeV^2 and $W^2 > 12.5$ GeV^2 (left-tilted hatched) are shown.

the fixed-target SLAC, BCDMS, and NMC experiments and from the HERA collider. To separate the contribution of each of these four data sets to the average Eq. (26) we also perform variants of the fit when only one of them is included and all other DIS data sets are discarded. However, the HT terms discussed above in Sec. III C can be determined consistently only if the SLAC data included. Therefore, in the variants of the fit based on either the BCDMS, NMC, or the HERA data set the HT coefficients are fixed to those values which have been obtained in our nominal analysis. Only in the variant based on the SLAC data the HT terms are fitted.

In addition, we consider for all cases also the variants when the HT terms are set to zero in order to check the sensitivity of the extracted value of α_s to this contribution. The values of $\alpha_s^{(n_f=5)}(M_Z)$ which have been obtained in this way are displayed in Fig. 29 in chronological order of the experiment. The most recent HERA run I + II data prefer

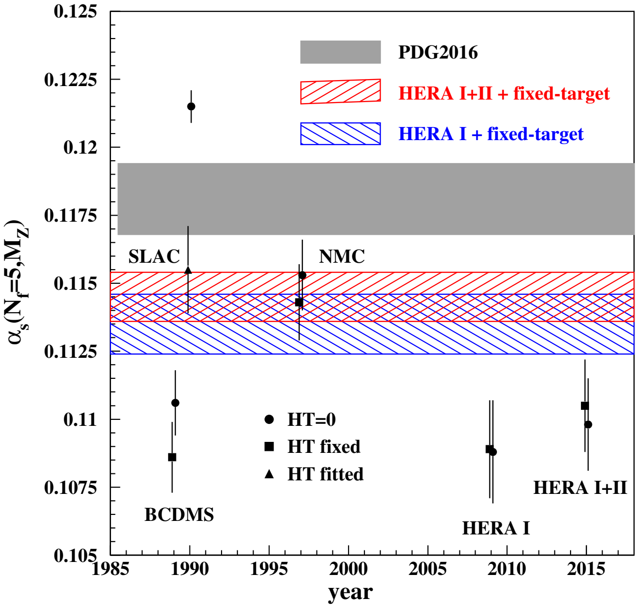

FIG. 29. The value of $\alpha_s^{(n_f=5)}(M_Z)$ in the $\overline{\mathrm{MS}}$ scheme for $n_f = 5$ at NNLO in QCD determined by the individual data sets as a function of the year of their publication. Data from SLAC [54,56,62] (proton), BCDMS [61], NMC [60] (proton), the HERA run I [213] as well as the HERA run I + II combination [4] are considered in three variants for the treatment of the higher twist terms defined in Eq. (6): (i) the higher twist terms are set to zero (circles); (ii) the higher twist terms are fixed to the values obtained in the ABMP16 fit from considering all data sets (squares); (iii) the higher twist terms are fitted to the individual data set under study (triangles). The bands for $\alpha_s^{(n_f=5)}(M_Z)$ obtained by using the combination of the SLAC, BCDMS and NMC samples together with those from the HERA run I (left-tilted hatched) and the run I + II combination (right-tilted hatched) as well as the 2016 PDG average [200] (shaded area) are presented for comparison.

the value of $\alpha_s^{(n_f=5)}(M_Z) = 0.1105 \pm 0.0017$. This is somewhat larger than the value preferred by the HERA run I data. However, it is significantly smaller than the 2016 PDG average [200]. It is worth noting that the HERA run I + II data are somewhat sensitive to the HT contribution, in contrast to those from HERA run I only. This is in line with the comparisons given in Fig. 26 and the discussion of Sec. III C. As a result of this trend the value of α_s extracted from the combination of the world DIS data used in the ABMP16 analysis increases by $\sim 1\sigma$ compared to our earlier determination in ABM12, which was based on the HERA run I data. However, the 2016 PDG average [200] is still by $\sim 2\sigma$ larger than our present determination based on the DIS data in Eq. (26). Only the $\alpha_s^{(n_f=5)}(M_Z)$ value derived from the SLAC data overlaps with the PDG error band. All other values are lower, in particular those from the BCDMS and HERA data.

The sensitivity of the DIS data to the treatment of the HT terms documented in Sec. III C also has an impact on the α_s determination. Indeed, for the variant of our analysis when the HT terms are not taken into account and the kinematic cuts in Eq. (24) are applied, the value

$$\alpha_s^{(n_f=5)}(M_Z) = 0.1167 \pm 0.0005 \tag{27}$$

is obtained at NNLO. This is larger than our nominal value in Eq. (26) by $\sim 3\sigma$. Imposing the more stringent cuts of Eq. (25) leads to the NNLO value of

$$\alpha_s^{(n_f=5)}(M_Z) = 0.1140 \pm 0.0009 \tag{28}$$

which restores the agreement with our nominal fit. This study demonstrates again the importance of the HT terms in the kinematic region $Q^2 = 2.5 \div 10\ \mathrm{GeV}^2$ which survive after applying the cuts of Eq. (24).

When the top-quark data listed in Tables III and IV are included, we find the value

$$\alpha_s^{(n_f=5)}(M_Z) = 0.1147 \pm 0.0008, \tag{29}$$

in the $n_f = 5$ flavor scheme at NNLO, which is not very different from the DIS one in Eq. (26), but has a slightly smaller statistical error. It is worth noting that the value of α_s extracted from the t-quark data strongly depends on the t-quark mass setting and the result in Eq. (29) is obtained by fitting m_t simultaneously with the PDFs and α_s, cf. Sec. III E.

Quite comparable values to the one we have obtained in the present NNLO analysis were obtained by the JR14 [8] with $\alpha_s^{(n_f=5)}(M_Z) = 0.1136 \pm 0.0004(\mathrm{stat})$ or $\alpha_s^{(n_f=5)}(M_Z) = 0.1162 \pm 0.0006(\mathrm{stat})$, depending on the PDF shape employed. Our value is also comparable to the one determined in earlier N^{3}LO analysis for nonsinglet DIS data [110], quoting $\alpha_s^{(n_f=5)}(M_Z) = 0.1141^{+0.0020}_{-0.0022}$.

Other groups, CTEQ, MSTW (MMHT), and NNPDF, have also determined the value of α_s in the PDF fits, see Ref. [216] for a recent survey. The NNLO values $\alpha_s^{(n_f=5)}(M_Z) = 0.1172 \pm 0.0013$ and $\alpha_s^{(n_f=5)}(M_Z) = 0.1174 \pm 0.0007$, obtained by the MSTW and NNPDF groups, respectively, despite looking similar, have a quite different origin, as has been shown in detail in Ref. [216]. The most essential issues appearing in the context of a comparison with the MSTW and NNPDF results concern the treatment of the higher twist terms discussed in Sec. III C, the nuclear corrections to the data on heavy-nuclei targets and the impact of missing NNLO corrections. A lower value $\alpha_s^{(n_f=5)}(M_Z) = 0.1150^{+0.0060}_{-0.0040}$ has been obtained by the CTEQ, yet with large errors, but well compatible with ours.

Finally, one may also compare with lattice simulations. The Alpha Collaboration quotes $\alpha_s^{(n_f=5)}(M_Z) = 0.1179 \pm 0.0011$ as a recent result [217] while other lattice results are summarized in Ref. [218].

E. Heavy-quark masses

In addition, to the PDF parameters listed in Table VII and to the strong coupling α_s the ABMP16 fit also determines the heavy-quark masses. In the $\overline{\mathrm{MS}}$ scheme, we obtain at NNLO in QCD the values

$$\begin{aligned} m_c(m_c) &= 1.252 \pm 0.018\ \mathrm{GeV}, \\ m_b(m_b) &= 3.84 \pm 0.12\ \mathrm{GeV}, \\ m_t(m_t) &= 160.9 \pm 1.1\ \mathrm{GeV}, \end{aligned} \tag{30}$$

where the scale μ_r has always been chosen identical to the numerical value of the masses. For the charm-quark mass often also the scale choice $\mu_r = 3$ GeV is used, for which one obtains

$$m_c(3\ \mathrm{GeV}) = 1.007 \pm 0.018\ \mathrm{GeV}. \tag{31}$$

The uncertainties quoted in Eq. (30) denote the 1σ confidence level as determined from the data listed in Sec. II A. Largely, these are the HERA data on DIS charm- [63] and bottom-quark production [15,16], cf. Table II. As the theory predictions for these DIS cross sections are not complete to NNLO yet, as described in Sec. II B, the charm- and bottom-quark masses in Eq. (30) carry an additional systematic model uncertainty due to the incomplete NNLO Wilson coefficients estimated as $\Delta m_c(m_c) \simeq 0.01$ GeV, cf. Fig. 1. Compared to previous analyses [1,219] this model uncertainty has been reduced by a factor of four thanks to the new theory improvements presented in Sec. II B. Thus, the current accuracy in the determination of m_c from DIS data is becoming

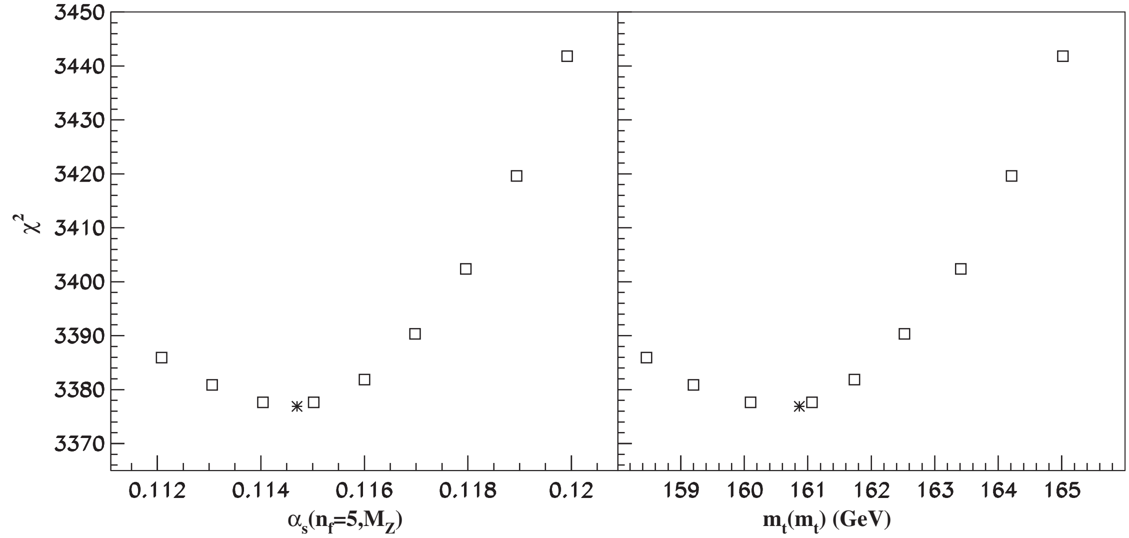

FIG. 30. The values of χ^2 obtained in the variants of present analysis with $\alpha_s^{(n_f=5)}(M_z)$ fixed (squares) versus $\alpha_s^{(n_f=5)}(M_z)$ (left) and $m_t(m_t)$ (right) in comparison with the best fit results (stars).

competitive with other methods entering the world average [200]. For the bottom mass, the use of approximate NNLO Wilson coefficients adds a model uncertainty $\Delta m_b(m_b) \simeq 0.1$ GeV to Eq. (30). On the other hand, the residual theory uncertainties from scale variations at NNLO are small, though. For the DIS heavy-quark cross sections considered in the present analysis, it amounts to $\Delta m_c(m_c) = \pm 0.025$ GeV for charm [108,219] and to $\Delta m_b(m_b) = \pm 0.09$ GeV for bottom [108].

For the top-quark mass we rely predominantly on the inclusive cross section of the top-quark pair production, cf. Table III, which is known completely to NNLO accuracy in QCD [184–187]. Data on single-top quark are used as well, cf. Table IV, but have a much larger uncertainty; see also [193]. The high precision data on top-quark pair production from the LHC taken at the different center-of-mass energies $\sqrt{s} = 5$, 7, 8, and 13 TeV lead to the small experimental uncertainty of $\Delta m_t(m_t) = \pm 1.1$ GeV in Eq. (30). This has to be compared to the effect of the scale variation on the extracted top-quark mass in the $\overline{\mathrm{MS}}$ scheme in the NNLO predictions of the total cross section, which can be quantified as $\Delta m_t(m_t) \simeq \pm 0.7$ GeV; see, e.g., [1].

The cross section data on top-quark hadro-production in Tables III and IV are, in fact, very sensitive to value of the mass m_t. In order to illustrate this sensitivity of the data, we present in Fig. 30 the χ^2 profiles versus the $\overline{\mathrm{MS}}$ mass $m_t(m_t)$ and the strong coupling $\alpha_s^{(n_f=5)}(M_Z)$ obtained in the scan fit with the value of $\alpha_s^{(n_f=5)}(M_Z)$ spanning the range of $0.112 \div 0.120$. The profiles nicely demonstrate a good consistency of the top-quark mass determination and also explain a correlation of the extracted value of $m_t(m_t)$ with α_s. This correlation is explicitly displayed in Fig. 31 with the overlap region of the two bands for $m_t(m_t)$ and α_s indicating the 1σ interval. Of course, the clear correlation shown is a direct consequence of the parametric dependence of the total cross section for the top-quark pair production on α_s and m_t. Of particular importance for m_t are also the correlations with other fitted parameters, mostly for the gluon distribution—a fact that has been addressed already in previous analyses [1]. With improved

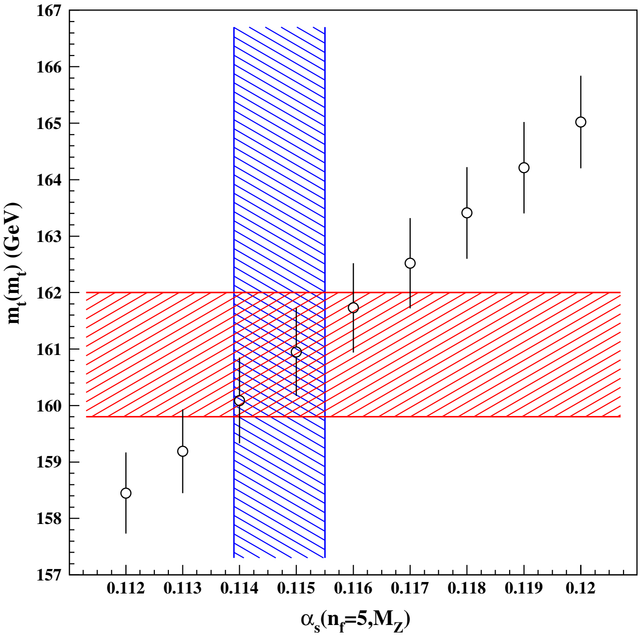

FIG. 31. The $\overline{\mathrm{MS}}$ value of the t-quark mass $m_t(m_t)$ obtained in the variants of present analysis with the value of $\alpha_s^{(n_f=5)}(M_Z)$ fixed in comparison with the 1σ bands for $m_t(m_t)$ and $\alpha_s^{(n_f=5)}(M_Z)$ obtained in our nominal fit (left-tilted and right-tilted hatch, respectively).

precision of data on single-top production in the t-channel, the impact of α_s on the m_t determination can be leveled, since that process is predominantly mediated by electroweak interactions and therefore sensitive to the light-flavor PDFs and the ratio of d/u [193].

The measured values of the charm and bottom masses in Eq. (30) can be confronted with the PDG values of 2016 [200]

$$m_c(m_c)|_{\mathrm{PDG}} = 1.27 \pm 0.03\ \mathrm{GeV},$$
$$m_b(m_b)|_{\mathrm{PDG}} = 4.18^{+0.04}_{-0.03}\ \mathrm{GeV}. \qquad (32)$$

For charm, there is perfect agreement of the PDG value with our fit result in Eq. (30) which has a comparable uncertainty. In the case of bottom, though, the fitted value in Eq. (30) carries a significantly larger error and comes out slightly lower than the PDG result in Eq. (32) and only agrees at the level of 1 to 2σ.

For the top-quark mass in the $\overline{\mathrm{MS}}$ scheme the PDG quotes

$$m_t(m_t)|_{\mathrm{PDG}} = 160.0^{+4.8}_{-4.3}\ \mathrm{GeV}, \qquad (33)$$

which is compatible with Eq. (30), though it is subject to very large uncertainties as Eq. (33) is only based on a single measurement performed at the Tevatron. Many other so-called direct mass measurements listed by the PDG cannot be interpreted in quantum field theory, as they lack a well defined renormalization scheme for the mass and need additional calibration of the extracted Monte-Carlo mass [220].

The on-shell scheme represents an alternative renormalization scheme for heavy-quark masses which is often used. For the purpose of comparison with that scheme we convert the bottom- and top-quark masses in Eq. (30) to the pole masses. At NNLO we obtain

$$m_b^{\mathrm{pole}} = 4.54 \pm 0.13\ \mathrm{GeV},$$
$$m_t^{\mathrm{pole}} = 170.4 \pm 1.2\ \mathrm{GeV}, \qquad (34)$$

using `RunDec` [221]. For the running charm quark mass the conversion of $m_c(\mu_r)$ to the pole mass definition at low scales $\mu_r \simeq 1.3$ GeV does not converge with the known relations up to four-loop order in perturbative QCD [222]. Using $\alpha_s^{(n_f=5)}(M_Z) = 0.1184$, for example, one obtains from the PDG central value in Eq. (32) $m_c^{\mathrm{pole}} = 1.47$ GeV at one loop, $m_c^{\mathrm{pole}} = 1.67$ GeV at two loops, $m_c^{\mathrm{pole}} = 1.93$ GeV at three loops, and $m_c^{\mathrm{pole}} = 2.39$ GeV at four loops [222].

The pole mass of the top-quark in Eq. (34) can also be compared with the PDG average, which quotes

$$m_t^{\mathrm{pole}}|_{\mathrm{PDG}} = 174.2 \pm 1.4\ \mathrm{GeV}. \qquad (35)$$

So there is a clear tension between the values of m_t^{pole} in Eqs. (34) and (35). The PDG average in Eq. (33) is based on three experimental analyses of LHC data on the inclusive cross section. However, these analyses disregard the correlations of the top-quark mass with α_s and the PDF parameters, especially the gluon PDF, in the theory predictions for the total cross section, as mentioned above and illustrated in Fig. 31. We remark, that the PDG value given in Eq. (33) for the $\overline{\mathrm{MS}}$ scheme result $m_t(m_t)$ is consistent with m_t^{pole} in Eq. (35) only within the large uncertainties of the former.

We briefly comment here on related studies, that have appeared in the literature. A determination of $m_c(m_c)$ from HERA data has been performed in Ref. [223] yielding $m_c(m_c) = 1.32 \pm 0.06$ GeV when fitting to DIS $c\bar{c}$-cross section predictions at NLO in QCD in a fixed flavor-scheme. Within the reported uncertainties, this is compatible with Eq. (30). Earlier, CT10 [224] had determined the charm-quark mass in the $\overline{\mathrm{MS}}$ scheme at NLO in a variable flavor-scheme, reporting a range $m_c(m_c) =$ 1.12–1.24 GeV depending on assumption in the fit. The ZEUS Collaboration has used its data [16] on DIS bottom-quark production to measure the bottom-quark mass at NLO in QCD and has reported $m_b(m_b) = 4.07 \pm 0.16$ GeV which is well compatible with Eq. (30) within uncertainties. LHC data on heavy-flavor hadro-production cross sections measured by LHCb have been shown to additionally constrain PDF parameters [225] and those data can provide input for future improvements of the m_b determination.

Finally, we comment on the treatment of heavy-quark masses in published PDF fits of other groups. With the exception of the JR14 [8] fit, which implements the $\overline{\mathrm{MS}}$ scheme for m_c, the available NNLO fits of other groups all use the on-shell scheme. In addition, the value of m_c is not fitted, but fixed beforehand, thereby disregarding any essential correlation, e.g., of m_c with the gluon PDF. In detail, the available NNLO fits use $m_c^{\mathrm{pole}} = 1.3$ GeV in case of CT14 [7], $m_c^{\mathrm{pole}} = 1.43$ GeV in case of HERAPDF2.0 [4], $m_c^{\mathrm{pole}} = 1.4$ GeV in case of MMHT14 [9], and $m_c^{\mathrm{pole}} = 1.275$ GeV in case of NNPDF3.0 [10], covering a range of values significantly larger than the uncertainties obtained, e.g., in Eq. (30). Some groups have performed dedicated studies of the charm and, sometimes, also bottom-quark mass dependence in their analysis, although not always within their latest fit; see e.g., CT10 [224], NNPDF2.1 [226] or MMHT14 [227].

The values for m_c^{pole} as used by CT14 [7], MMHT14 [9] or NNPDF3.0 [10] are systematically too low compared to precision determinations of $m_c(m_c)$ based on the rigorous application of quantum field theory as in Eq. (30) and the world average Eq. (32) once the latter $m_c(m_c)$ values are converted to the on-shell scheme at a given order in perturbation theory, as discussed below Eq. (34). Due to

TABLE IX. Second moment of valence quark distributions at NNLO at $\mu^2 = 4$ GeV^2 with their uncertainties. For ABM11, ABM12 and ABMP16 the sets with $n_f = 3$ flavors have been used.

	$\langle xu_v(x)\rangle$	$\langle xd_v(x)\rangle$	$\langle x[u_v - d_v](x)\rangle$	$\langle xV(x)\rangle$
ABM11 [71]	0.2966 ± 0.0039	0.1172 ± 0.0050	0.1794 ± 0.0041	0.1652 ± 0.0039
ABM12 [1]	0.2950 ± 0.0029	0.1212 ± 0.0016	0.1738 ± 0.0025	0.1617 ± 0.0031
ABMP16 (this work)	0.2911 ± 0.0024	0.1100 ± 0.0031	0.1811 ± 0.0032	0.1674 ± 0.0037
CT14 [7][a]	$0.2887^{+0.0074}_{-0.0073}$	$0.1180^{+0.0053}_{-0.0041}$	$0.1707^{+0.0078}_{-0.0092}$	$0.1579^{+0.0095}_{-0.0117}$
MMHT14 [9]	$0.2852^{+0.0052}_{-0.0034}$	$0.1202^{+0.0030}_{-0.0031}$	$0.1650^{+0.0047}_{-0.0034}$	$0.1509^{+0.0053}_{-0.0039}$
NNPDF3.0 [10]	0.2833 ± 0.0042	0.1183 ± 0.0049	0.1650 ± 0.0054	0.1553 ± 0.0037

[a] The PDF uncertainties of CT14 denote the 90% confidence level and need rescaling with a factor of 1.645 for comparison with the 68% confidence level uncertainties quoted for all other results.

the evident correlations of the heavy-quark masses and other PDF parameters, as documented for the fits CT10 [224], NNPDF2.1 [226] or MMHT14 [227], such low values of $m_c^{\rm pole}$ lead to bias in phenomenology predictions even at LHC scales, in particular, for the benchmark processes such as Higgs boson production in gluon-gluon fusion [11].

IV. APPLICATIONS

A. Moments of PDFs and lattice results

The values for the second moment of the quark PDFs at the factorization scale $\mu^2 = 4$ GeV^2 for ABM11 [71], ABM12 [1] and ABMP16 as well as for CT14 [7], MMHT14 [9] and NNPDF3.0 [10] are provided in Table IX. The quantity $\langle xu_v(x)\rangle$ for the up-quark valence PDF is rather stable as it is mostly influenced by the data normalization. The moments of distributions involving down-quark PDFs show a spread of the central values, though, which is much larger than the bands covering the 1σ uncertainty of the respective analysis. In particular, isospin asymmetries such as $x[u_v - d_v](x)$ or $xV(x)$ defined as

$$\langle xV(\mu^2)\rangle = \int_0^1 dxx\{[u(x,\mu^2) + \bar{u}_s(x,\mu^2)] - [d(x,\mu^2) + \bar{d}_s(x,\mu^2)]\} \qquad (36)$$

with $q \equiv q_v + q_s$ and $q = u$, d are quite different among the various analyses.

At this point, we emphasize that the ABMP16 fit uses the widest set of Drell-Yan measurements from the LHC and Tevatron, which provide unique constraints in the low-x region and allow for a model-independent shape of the isospin asymmetry $x[\bar{d} - \bar{u}](x)$. Comparing the ABM12 [1] and ABMP16 fits, the shifts in the moments proportional to down-quark PDFs in Table IX are reflected in a smaller value of ABMP16 for the cross section ratio $\sigma_{W^+}/\sigma_{W^-}$ for the production of $W^\pm$-bosons in the fiducial volume, shown in Fig. 13. In addition, also single-top quark production constrains the ratio d/u and the nice agreement of the ABMP16 fit with those data is demonstrated in Fig. 17.

The nonsinglet distribution $xV(x)$ is also particularly suited for comparison to lattice simulations. The results on $\langle xV(\mu^2)\rangle$ at the scale $\mu^2 = 4$ GeV^2 obtained with the ABMP16, CT14 [7], MMHT14 [9] and NNPDF3.0 [10] PDFs are compared with recent lattice computations as a function of the pion mass squared, m_π^2, in Fig. 32. The lattice measurements of Refs. [228–231] use set-ups with $(n_f = 2)$ and $(n_f = 2+1+1)$ for the number of flavors and low pion masses in the range $m_\pi = 133$ MeV to 329 MeV, very close to the physical point of $m_\pi = 138$ MeV. There is a clear trend in the lattice results towards smaller values of $\langle xV(\mu^2)\rangle$ as the pion mass approaches the physical value. For the lattice result taken at the lowest value in m_π the compatibility with the determination from experimental data by ABMP16 is at the level of 2σ. The PDFs of CT14, MMHT14 and NNPDF3.0, however, give significantly lower values in Table IX, so that the differences are at the level of 3 to 4σ, and compatibility is marginal. As stressed above, experimental data clearly favors larger values of $\langle xV(\mu^2)\rangle$.

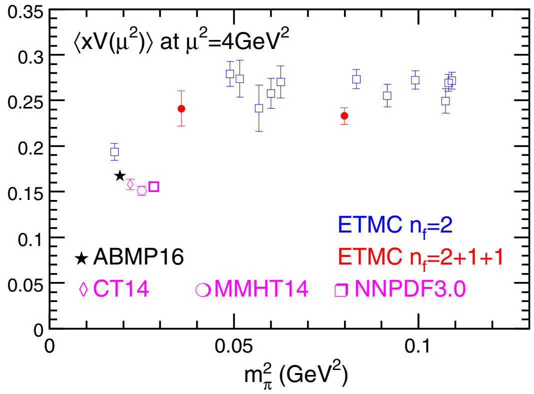

FIG. 32. Lattice computations of Refs. [228–231] for the second moment of the nonsinglet distribution $xV(\mu^2)$ at the scale $\mu^2 = 4$ GeV^2 as a function of the pion mass squared, m_π^2, including the uncertainties of the respective measurement compared to the results of ABMP16, CT14, MMHT14 and NNPDF3.0 PDFs given in Table IX. The results for CT14, MMHT14 and NNPDF3.0 have been shifted in Δm_π with respect to ABMP16 for display purposes.

In summary, Fig. 32 demonstrates nicely, that future high precision lattice measurements in QCD with ($n_f = 2+1+1$) flavors performed around the physical pion mass can potentially provide valuable constraints on the down-quark PDF and, most importantly, on the iso-spin asymmetry $x[\bar{d} - \bar{u}](x)$.

B. Benchmark cross sections at the LHC

Next, we proceed with cross section predictions for the Higgs boson production in the gluon-gluon-fusion and hadro-production of the top-quark pairs at the LHC in order to benchmark the ABMP16 PDFs.

The gluon-gluon fusion process is the dominant production mechanism for the SM Higgs boson at the LHC and the QCD radiative corrections to the inclusive cross section are particularly large at NLO; see e.g., Ref. [232]. This has motivated systematic theory improvements in the effective theory to NNLO [233–235] and even to N^{3}LO accuracy [236,237], by taking the limit of a large top-quark mass ($m_t \to \infty$) and integrating out the top-quark loop, while keeping the full m_t dependence in the Born cross section. The recent N^{3}LO results [236,237] demonstrate an apparent, if slow, convergence of the perturbative expansion. The sensitivity to the choice of the renormalization and factorization scales μ_r and μ_f is greatly reduced and amounts to 3% at N^{3}LO, which is also supported by estimates of the four-loop corrections [238].

In this situation, with perturbative QCD predictions of unprecedented accuracy for the hard-scattering process being available, the largest remaining sources of uncertainties are the input value for the strong coupling constant α_s and the PDFs. Indeed, the spread in the inclusive cross sections $\sigma(H)^{\rm NNLO}$ of SM Higgs boson production at the LHC at NNLO [233–235] predicted by the PDF sets CJ15 [6], CT14 [7], HERAPDF2.0 [4], JR14 [8], MMHT14 [9], and NNPDF3.0 [10] amounts to 13% as documented in Ref. [11]. This is significantly larger than the PDF uncertainties quoted by the individual sets and dominates by far over the residual scale uncertainty of the N^{3}LO QCD corrections. A detailed comparison of those PDFs carried out in Ref. [11] has illustrated how these differences arise as a consequence of specific theory assumptions such as tuned values of m_c or varying values of $\alpha_s^{(n_f=5)}(M_Z)$ used in the individual fits.

In Table X, we present the results on $\sigma(H)^{\rm NNLO}$ for the LHC at $\sqrt{s} = 13$ TeV in the effective theory (i.e., in the limit of $m_t \gg m_H$) with parameter choices $m_H = 125.0$ GeV for the SM Higgs boson mass, scales $\mu_r = \mu_f = m_H$, and using the PDF sets ABM12 [1], ABMP15 [3] and ABMP16. The value $m_t^{\rm pole} = 172.5$ GeV in Table X has been chosen for compatibility with the recent benchmark study in [11]. The quoted uncertainties are given at the 1σ confidence level and the results for $\sigma(H)^{\rm NNLO}$ employ either the nominal value of the strong coupling constant $\alpha_s^{(n_f=5)}(M_Z)$ at NNLO, or fixed values of $\alpha_s^{(n_f=5)}(M_Z) = 0.115$ and $\alpha_s^{(n_f=5)}(M_Z) = 0.118$, while keeping the correlation with the PDF parameters.

We also quote $\sigma(H)^{\rm NNLO}$ with uncertainties obtained with the set PDF4LHC15 [239] which has been obtained as some average of CT14, MMHT14 and NNPDF3.0 using the same fixed value of $\alpha_s^{(n_f=5)}(M_Z) = 0.1180$ at NLO and at NNLO independent of the order of perturbation theory and, thereby, disregarding correlations. This set has been employed in the recent study [240] of the LHC Higgs Cross Section Working Group which quotes a combined PDF and α_s uncertainty in the inclusive cross section as small as 3.2%. In view of the bias incurred with a fixed value of $\alpha_s^{(n_f=5)}(M_Z) = 0.118$ and the benchmark studies of [11], this uncertainty is underestimated.

The cross section for hadro-production of top-quark pairs at the LHC is another benchmark process. As described in Sec. II A, the present analysis is based on the large sample of the top-quark pair and for single-top quark production data (cf. Tables III and IV and Figs. 16 and 17).

In Table XI, we present results for the inclusive cross section $\sigma(t\bar{t})^{\rm NNLO}$ for top-quark pair production with the theory description detailed in Sec. II B, i.e., NNLO accuracy in QCD [184–187] using `Hathor` [189]. We apply the PDF sets ABM12 [1], ABMP15 [3] and ABMP16 with the top-quark mass in the $\overline{\rm MS}$ scheme, $m_t(m_t) = 160.9$ GeV, and scales $\mu_r = \mu_f = m_t(m_t)$ for various center-of-mass energies of the LHC, $\sqrt{s} = 5$, 7,

TABLE X. Cross section for the Higgs boson production from the gluon fusion at NNLO in QCD (computed in the effective theory) with the PDF and α_s uncertainties at $\sqrt{s} = 13$ TeV for $m_H = 125.0$ GeV for $\mu_r = \mu_f = m_H$. The columns list the value of α_s for each PDF set and the cross sections values obtained with both the nominal PDF set and the choices for α_s indicated.

PDF sets	$\alpha_s^{(n_f=5)}(M_Z)$	$\sigma(H)^{\rm NNLO}$ [pb] nominal α_s	$\sigma(H)^{\rm NNLO}$ [pb] $\alpha_s^{(n_f=5)}(M_Z) = 0.115$	$\sigma(H)^{\rm NNLO}$ [pb] $\alpha_s^{(n_f=5)}(M_Z) = 0.118$
ABM12 [1]	0.1132 ± 0.0011	39.80 ± 0.84	41.62 ± 0.87	44.70 ± 0.91
ABMP15 [3]	0.1132 ± 0.0011	39.46 ± 0.77	41.30 ± 0.79	44.36 ± 0.83
ABMP16 (this work)	0.1147 ± 0.0009	40.20 ± 0.63	40.50 ± 0.64	43.50 ± 0.67
PDF4LHC15 [239]	0.1180 (fixed)	42.42 ± 0.78	39.49 ± 0.73	42.42 ± 0.78

TABLE XI. Cross section for the top-quark pair production at NNLO in QCD with the PDF uncertainties for the top-quark mass $m_t(m_t) = 160.9$ GeV in the $\overline{\text{MS}}$ scheme and $\mu_r = \mu_f = m_t(m_t)$ at various center-of-mass energies of the LHC.

PDF sets	$\sigma(t\bar{t})^{\text{NNLO}}$ [pb] at $\sqrt{s} = 5$ TeV	$\sigma(t\bar{t})^{\text{NNLO}}$ [pb] at $\sqrt{s} = 7$ TeV	$\sigma(t\bar{t})^{\text{NNLO}}$ [pb] at $\sqrt{s} = 8$ TeV	$\sigma(t\bar{t})^{\text{NNLO}}$ [pb] at $\sqrt{s} = 13$ TeV
ABM12 [1]	56.03 ± 2.76	156.8 ± 6.4	228.6 ± 8.6	793.9 ± 22.1
ABMP15 [3]	56.79 ± 2.98	157.4 ± 6.9	229.0 ± 9.3	791.0 ± 23.7
ABMP16 (this work)	63.66 ± 1.60	171.8 ± 3.4	247.5 ± 4.6	831.4 ± 14.5

8, and 13 TeV. The uncertainties quoted represent the combined symmetric 1σ uncertainty $\Delta\sigma(\text{PDF} + \alpha_s)$ arising from the variation of the PDF parameters and of α_s in 28 PDF sets for ABM12 or ABMP15, and $\Delta\sigma(\text{PDF} + \alpha_s + m_t)$ originating from 29 sets including also the variation of m_t in case of the ABMP16 PDFs.

The ABMP16 value of α_s has shifted upwards by about 1σ as compared to the ABM12 and ABMP15 one, i.e., $\alpha_s^{(n_f=5)}(M_Z) = 0.1147$ for the former and $\alpha_s^{(n_f=5)}(M_Z) = 0.1132$ for the later, cf. the discussion in Sec. III D. Correspondingly, the cross section predictions in Table XI display a systematic trend in upward shifts at the level of 1 to 2σ in the associated uncertainties. Note also, that the overall cross section uncertainty $\Delta\sigma(\text{PDF} + \alpha_s + m_t)$ for ABMP16 is significantly reduced compared to previous fits thanks to the high precision data in Table III.

C. Stability of the electroweak vacuum

Recent high-precision measurements of the Higgs boson mass m_H quote

$$m_H = 125.09 \pm 0.24 \text{ GeV} \tag{37}$$

as a very accurate average [241]. Due to an intriguing coincidence of the value for m_H in Eq. (37) and the measured masses of all other SM particles, the Higgs potential can possibly develop a second minimum at field values as large as the Planck scale $M_{\text{Pl}} \simeq 10^{19}$ GeV in addition to the one we live in, which corresponds to the vacuum expectation value $v = 246$ GeV. If realized in Nature, this would imply stability of the SM up to the high scales where unification with gravity is expected. On the contrary, the occurrence of an instability of the electroweak vacuum at some large scales above the terascale but below M_{Pl} indicates the breakdown of the SM and invokes the necessity for new physics. Thus, it is important to test the running of the Higgs boson self-coupling λ in the SM up to large scales with the help of renormalization group analyses currently available to three-loop accuracy [242–244] supplemented by the necessary matching conditions at the two-loop level [12,13,245].

The evolution of the renormalization group equations from scales $\mathcal{O}(100)$ GeV to M_{Pl} critically depends on the input values for the SM parameters, in particular the top-quark mass and the strong coupling constant α_s. Having determined both of them simultaneously including correlations, cf. Sec. III E, we are in a position to update previous work [246] by investigating consequences of such a correlation for the study of the Higgs potential at large scales. The condition for the vacuum stability to hold at M_{Pl} can be formulated as a lower bound on the mass of the Higgs boson as follows [247]

$$m_H = 129.6 \text{ GeV} + 1.8 \times \left(\frac{m_t^{\text{pole}} - 173.34 \text{ GeV}}{0.9}\right) - 0.5 \times \left(\frac{\alpha_s^{(n_f=5)}(M_Z) - 0.1184}{0.0007}\right) \text{ GeV} \pm 0.3 \text{ GeV}, \tag{38}$$

where m_t and α_s are to be taken in the on-shell and $\overline{\text{MS}}$ schemes, respectively, and the uncertainty of ± 0.3 GeV appears due to missing higher-order corrections. A similar condition based on a manifestly gauge-independent approach including two-loop matching and three-loop renormalization group evolution has been reported in Ref. [248].

In Fig. 33, we display the value of m_H according to Eq. (38) evaluated as a function of $\alpha_s^{(n_f=5)}(M_Z)$. The corresponding values of the pole mass for the top-quark m_t^{pole} are derived from the values for $m_t(m_t)$ in the $\overline{\text{MS}}$ scheme which have been obtained in the variants of our analysis with the values of $\alpha_s^{(n_f=5)}(M_Z)$ scanned in the range of $0.112 \div 0.120$. In doing so, the uncertainties in the fitted values for m_t and the correlation between m_t and α_s have been taken into account, cf. Fig. 31. The error band on m_H derived in this way overlaps with the one obtained from a direct measurement of m_H for the value of $\alpha_s^{(n_f=5)}(M_Z)$ close to our determination in Eq. (29). This implies, that the values of m_t and α_s obtained in our analysis are consistent with the condition of vacuum stability at M_{Pl}.

In a complementary way, this is illustrated in Fig. 34 showing the running of the Higgs boson self-coupling $\lambda(\mu_r)$ in full three-loop accuracy and with α_s and m_t obtained in our analysis as the input parameters as well as the 2016 PDG values [200] for the other SM masses and couplings.

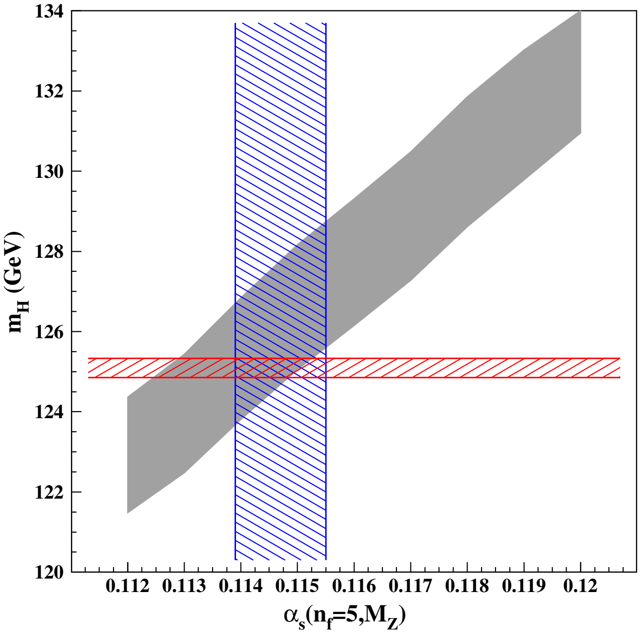

FIG. 33. The value of Higgs-boson mass m_H computed according to the condition in Eq. (38) for vacuum stability at $M_{\rm Pl}$ using the values of m_t with their uncertainties obtained in the present analysis by scanning $\alpha_s^{(n_f=5)}(M_Z)$ in the range of $0.112 \div 0.120$ and disregarding the theoretical uncertainty of ±0.3 GeV (gray band). For comparison the 1σ bands for $\alpha_s^{(n_f=5)}(M_Z)$ from the nominal fit and the value of m_H in Eq. (37) (left-tilted and right-tilted hatch, respectively) are shown.

The computation has been performed with the code `mr`, which implements matching and running of the SM parameters [249]. Clearly, a vanishing Higgs self-coupling $\lambda = 0$ at $M_{\rm Pl}$ remains a scenario which is compatible with the current values of α_s, m_t and m_H within their 1σ uncertainties. In addition, as follows from our analysis the value of $\lambda(\mu_r)$ remains strictly positive up to renormalization scales $\mu_r \sim \mathcal{O}(10^{12}\ \text{GeV})$, so that no new physics needs to be invoked in order to stabilize the electroweak vacuum.

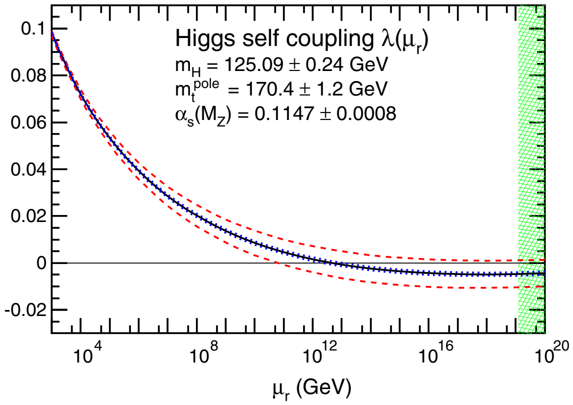

FIG. 34. The renormalization group evolution of the Higgs boson self-coupling λ as a function of scale μ_r. The dashed (red) lines denote the combined 1σ uncertainty for $\alpha_s^{(n_f=5)}(M_Z)$ and $m_t^{\rm pole}$ and the dotted (blue) lines the 1σ uncertainty in the value of m_H in Eq. (37). The range of scales $\mu_r \geq M_{\rm Pl}$ is indicated by the hatched (green) band on the right.

D. LHAPDF library

The PDFs obtained in the present analysis are provided in the form of grids accessible with the `LHAPDF` library (version 6) [14] and available for download under http://projects.hepforge.org/lhapdf. The PDFs for a fixed number of flavors, $n_f = 3$, 4 and 5, at NNLO

`ABMP16_3_nnlo(0+29)`,

`ABMP16_4_nnlo(0+29)`,

`ABMP16_5_nnlo(0+29)`,

consist of the central fit (set 0) and additional 29 sets for the combined symmetric uncertainties on the PDF parameters and on the values of α_s and the heavy-quark masses.[5] The quoted PDF uncertainties are calculated in the standard manner and correspond to the $\pm 1\sigma$-variation. The PDF uncertainty $\Delta\sigma_{\rm PDF}$ for a given cross section σ_0 is then computed according to

$$\Delta\sigma_{\rm PDF} = \sqrt{\sum_{k=1}^{n_{\rm PDF}} (\sigma_0 - \sigma_k)^2}, \tag{39}$$

where σ_k is obtained by using the k-th PDF set and $n_{\rm PDF} = 29$.

The PDF set for $n_f = 3$, `ABMP16_3_nnlo`, with three light-quark flavors is valid at all perturbative scales $\mu^2 \gtrsim 1\ \text{GeV}^2$. In contrast, PDFs with a fixed number of flavors, $n_f = 4$ or 5, are only meaningful at scales $\mu^2 \gg m_c^2$ and $\mu^2 \gg m_b^2$, respectively. Therefore, minimal cuts in $\mu^2 \geq 3\ \text{GeV}^2$ for the grid `ABMP16_4_nnlo` and $\mu^2 \geq 20\ \text{GeV}^2$ for `ABMP16_5_nnlo` have been imposed and the PDF grids are not available below these cuts. Note, however, that by default the `LHAPDF` library (version 6) [14] extrapolates the PDFs also to kinematics outside those covered by the grid in x and μ^2. Therefore, the grids `ABMP16_4_nnlo` and `ABMP16_5_nnlo` at low values of μ^2 should be used with a particular care.

We also remark, that the PDF sets for $n_f = 3$, 4 and 5 flavors at NNLO use the strong coupling α_s correspondingly, i.e., the couplings are taken in the scheme $\alpha_s^{(n_f=3)}$, $\alpha_s^{(n_f=4)}$ and $\alpha_s^{(n_f=5)}$ and need to be related by the standard decoupling relations in QCD. Since the heavy-quark masses $m_c(m_c)$, $m_b(m_b)$ and $m_t(m_t)$ determined in our

---

[5] Corresponding data grids for the `LHAPDF` library (version 5) [250] are available from the authors upon request.

analysis are correlated with the PDF parameters they are different for each of the 29 PDF sets. Therefore, a self-consistent prediction of PDF uncertainties on the cross sections involving heavy quarks should be computed by varying the respective heavy-quark masses simultaneously with the PDFs in the loop Eq. (39). The corresponding heavy-quark mass values can be easily retrieved within the `LHAPDF` library framework. The values of $\alpha_s^{(n_f=5)}(M_Z)$ and the heavy-quark masses encoded in the ABMP16 grids are listed in Table XII for reference. In addition, we also provide the bottom- and the top-quark pole masses, $m_b^{\rm pole}$ and $m_t^{\rm pole}$, obtained using `RunDec` [221] to be employed in corresponding computations with the on-shell scheme. Specifically, for the central ABMP16 set the values $m_b^{\rm pole} = 4.537$ GeV and $m_t^{\rm pole} = 170.37$ GeV should be used.

TABLE XII. Values of $\alpha_s^{(n_f=5)}(M_Z)$ and heavy-quark masses $m_c(m_c)$, $m_b(m_b)$ and $m_t(m_t)$ in the $\overline{\rm MS}$ scheme obtained for the individual PDF sets of ABMP16. For bottom and top, also the values for pole masses $m_b^{\rm pole}$ and $m_t^{\rm pole}$ in the on-shell scheme are given.

PDF set	$\alpha_s^{(n_f=5)}(M_Z)$	$m_c(m_c)$ [GeV]	$m_b(m_b)$ [GeV]	$m_b^{\rm pole}$ [GeV]	$m_t(m_t)$ [GeV]	$m_t^{\rm pole}$ [GeV]
0	**0.11471**	**1.252**	**3.838**	**4.537**	**160.86**	**170.37**
1	0.11471	1.252	3.839	4.538	160.86	170.37
2	0.11472	1.251	3.838	4.537	160.86	170.37
3	0.11471	1.252	3.839	4.538	160.86	170.37
4	0.11468	1.252	3.839	4.537	160.86	170.37
5	0.11463	1.252	3.839	4.536	160.86	170.36
6	0.11468	1.252	3.839	4.537	160.86	170.37
7	0.11471	1.251	3.839	4.538	160.86	170.37
8	0.11456	1.252	3.839	4.535	160.86	170.35
9	0.11510	1.252	3.838	4.545	160.86	170.41
10	0.11453	1.251	3.839	4.534	160.86	170.35
11	0.11472	1.250	3.838	4.537	160.86	170.37
12	0.11468	1.250	3.839	4.537	160.86	170.37
13	0.11469	1.267	3.838	4.536	160.86	170.37
14	0.11478	1.250	3.838	4.538	160.86	170.38
15	0.11487	1.249	3.838	4.540	160.86	170.38
16	0.11453	1.254	3.840	4.535	160.86	170.35
17	0.11477	1.252	3.961	4.671	160.86	170.37
18	0.11469	1.252	3.861	4.561	160.86	170.37
19	0.11460	1.252	3.846	4.543	160.87	170.37
20	0.11481	1.251	3.835	4.536	160.85	170.37
21	0.11471	1.252	3.848	4.548	160.89	170.40
22	0.11483	1.254	3.827	4.527	160.80	170.32
23	0.11467	1.252	3.837	4.535	160.81	170.31
24	0.11492	1.250	3.835	4.538	161.34	170.89
25	0.11461	1.252	3.844	4.541	160.57	170.05
26	0.11522	1.252	3.836	4.545	161.51	171.10
27	0.11486	1.251	3.831	4.532	161.04	170.57
28	0.11466	1.252	3.840	4.538	160.86	170.36
29	0.11497	1.248	3.827	4.530	161.47	171.03

Finally, for detailed studies of the parametric dependence of LHC observables on the strong coupling constant α_s, we provide the $n_f = 5$ flavor NNLO PDF grids with the central value of $\alpha_s^{(n_f=5)}(M_Z)$ fixed. In total, there are nine sets covering the range $\alpha_s^{(n_f=5)}(M_Z) = 0.112 \div 0.120$ with a spacing of 0.001. These sets are denoted

`ABMP16als112_5_nnlo(0+29)`,
`ABMP16als113_5_nnlo(0+29)`,
`ABMP16als114_5_nnlo(0+29)`,
`ABMP16als115_5_nnlo(0+29)`,
`ABMP16als116_5_nnlo(0+29)`,
`ABMP16als117_5_nnlo(0+29)`,
`ABMP16als118_5_nnlo(0+29)`,
`ABMP16als119_5_nnlo(0+29)`,
`ABMP16als120_5_nnlo(0+29)`,

with the value of $\alpha_s^{(n_f=5)}(M_Z)$ fixed as indicated in the file names and additional 29 sets for the combined symmetric uncertainties.[6]

V. CONCLUSIONS

The new ABMP16 PDFs presented have been determined from a global fit to the most recent experimental data on the basis of theory predictions at NNLO in perturbative QCD. Essential ingredients of the ABMP16 analysis are the inclusion of the final HERA DIS combination data from run I + II, new data sets from the fixed-target DIS experiments CHORUS and NOMAD, the recent LHC and Tevatron DY production data as well as an exhaustive sample of data for the top-quark hadro-production. The new combined DIS data from run I + II at HERA and the fixed-target experiments CHORUS and NOMAD in combination with the precise DY data from Tevatron and the LHC allow for a very accurate determination of the valence quark distributions and the flavor separation of the up- and down-quarks in a wide range of parton momentum fractions, $x \simeq 10^{-4}$ to 0.9. The accuracy of the down-quark distribution from these data is found to be comparable with the one from the DIS deuteron data, used previously for the ABM12 PDFs. Therefore the latter have been discarded from the present analysis avoiding additional uncertainties related to modeling of nuclear effects in deuterium targets. Moreover, the addition of the recent charm di-muon production data from NOMAD and CHORUS leads to an improved accuracy of the strange quark content in the

---

[6] For the purpose of technical consistency the value of α_s in these grids is still considered as a formal parameter, however, with greatly suppressed uncertainty.

proton compared to the earlier ABM12 analysis. The moments of light-quark PDFs obtained with all these improvements are found to be in very good agreement with recent lattice measurements at the physical pion mass.

The DIS heavy-quark production data and the Tevatron and LHC data on the inclusive single-top and top-quark pair production have been used to determine the heavy-quark masses which are considered as free parameters in the present analysis and fitted simultaneously with the PDFs and the strong coupling constant α_s to preserve all correlations between those parameters. Specifically, we determine the heavy-quark masses $m_c(m_c)$, $m_b(m_b)$ and $m_t(m_t)$, in the $\overline{\mathrm{MS}}$ scheme providing better perturbative stability both for the DIS and hadronic heavy-quark production.

The theory predictions for the hard-scattering processes in the ABMP16 analysis maintain NNLO accuracy in QCD and employ the fixed-flavor number scheme, which has been shown to provide an excellent description of the existing DIS data. In addition, the theory framework features a number of new improvements. It contains new approximations for the NNLO Wilson coefficients in the description of the DIS heavy-quark production as well as advances in predictions of single-top production in the s-channel to approximate NNLO accuracy. The ABMP16 analysis is also based on a refined treatment of higher twist contributions to the power corrections in DIS which extends to small values of x. In particular, it has been clearly demonstrated that higher twist terms in DIS are required for the kinematic coverage of the data analyzed. Moreover, higher twist terms cannot be entirely eliminated by the cut on hadronic invariant mass $W^2 \gtrsim 12\ \mathrm{GeV}^2$ in DIS proposed in the literature.

As a result of the new theory improvements and newly added data in the current analysis, an updated value of the strong coupling constant α_s has been determined in the $\overline{\mathrm{MS}}$ scheme for $n_f = 5$ at NNLO in QCD accuracy. It yields a value of $\alpha_s^{(n_f=5)}(M_Z) = 0.1147 \pm 0.0008$, which represents a shift upwards in the central value by 1σ compared to the previous ABM12 analysis due to the impact of the new combined HERA run I + II data. For the heavy-quark masses we find at NNLO in the $\overline{\mathrm{MS}}$ scheme $m_c(m_c) = 1.252 \pm 0.018$ GeV, $m_b(m_b) = 3.84 \pm 0.12$ GeV and $m_t(m_t) = 160.9 \pm 1.1$ GeV, respectively. This corresponds to a pole mass $m_t^{\mathrm{pole}} = 170.4 \pm 1.2$ GeV for the top-quark. Furthermore, a renormalization group analysis of the SM couplings accurate to three-loop order shows, that the obtained values of α_s and m_t^{pole} employed with account of their correlations are compatible with the requirement of a stable electroweak vacuum up to the Planck scale $\mathcal{O}(10^{19}\ \mathrm{GeV})$, thereby diminishing the need to introduce new physics.

In summary, the new ABMP16 analysis and the corresponding PDFs pave the way for precision predictions at the LHC in run II, so that future precision measurements can be confronted with theory computations at highest accuracy. With no doubt, this will offer the chance for further improvements in the description of the parton content of the proton. At the same time, benchmark comparisons with other PDF sets published in the literature will allow to test and, possibly, to eliminate the remaining underlying model assumptions and tunes in those fits. This will, finally, consolidate the understanding of PDFs and QCD at high scales.

ACKNOWLEDGMENTS

We are grateful to Daniel Britzger, Maria Vittoria Garzelli, Karl Jansen, Uta Klein, Mikhaylo Lisovyi, Frank Petriello, Andrey Pikelner, Klaus Rabbertz and Andreas Vogt for useful discussions. This work has been supported by Bundesministerium für Bildung und Forschung (Contract No. 05H15GUCC1) and by the European Commission through PITN-GA-2012-316704 (*HIGGSTOOLS*).

APPENDIX A: HEAVY-QUARK DIS COEFFICIENT FUNCTIONS

Here, we provide details on the construction of the NNLO approximations of the gluon and pure-singlet heavy-quark coefficient functions, $c_{2,g}^{(2,0)}$ and $c_{2,q}^{(2,0)}$, presented in Sec. II B. The ansatz of Ref. [97] combines the results from the various kinematic regions, i.e., those near threshold $s \simeq 4m^2$, at high energies $s \gg 4m^2$ and for large $Q^2 \gg m^2$. Following Ref. [97], we use the ansatz for the NNLO coefficient functions,

$$\begin{aligned} c_{2,i}^{(2,0),A} &= \delta_{ig}(c_{2,g}^{(2,0)\mathrm{thr}}) + (1 - f(\xi))\beta c_{2,i}^{(2,0)\mathrm{asy},A} \\ &\quad + f(\xi)\beta^3\left(-c_{2,i}^{(2,0)\mathrm{LLx}}\frac{\ln\eta}{\ln x} + c_{2,i}^{(2,0)\mathrm{NLL},A}\frac{\eta^\gamma}{C+\eta^\gamma}\right), \end{aligned} \tag{A1}$$

and

$$\begin{aligned} c_{2,i}^{(2,0),B} &= \delta_{ig}(c_{2,g}^{(2,0)\mathrm{thr}} + f(\xi)2c_{2,g}^{(2,0)\mathrm{const}}) \\ &\quad + (1 - f(\xi))\beta^3 c_{2,i}^{(2,0)\mathrm{asy},B} \\ &\quad + f(\xi)\beta^3\left(-c_{2,g}^{(2,0)\mathrm{LLx}}\frac{\ln\eta}{\ln x} + c_{2,g}^{(2,0)\mathrm{NLL},B}\frac{\eta^\delta}{D+\eta^\delta}\right), \end{aligned} \tag{A2}$$

where $\beta = \sqrt{1 - 4m^2/s}$ and explicit expressions can be found in Ref. [97]. In short, the threshold contributions $c_{2,g}^{(2,0)\mathrm{thr}}$ and $c_{2,g}^{(2,0)\mathrm{const}}$ for the gluon coefficient function are given by the scale-independent terms in Eqs. (3.18) and (3.19) of Ref. [97]. The asymptotic results for the quark and gluon coefficient functions $c_{2,i}^{(2,0)\mathrm{asy}}$ at large $Q^2 \gg m^2$ are given by the scale-independent terms of Eqs. (B.8) and (B.10) of Ref. [97] where it is understood that in the case of the gluon coefficient functions $c_{2,g}^{(2,0)}$ the results for $a_{Qg,A}^{(3)0}$ and $a_{Qg,B}^{(3)0}$ in Eqs. (15) and (16) are used to account for an uncertainty band due to the heavy-quark OME A_{Qg} while for the pure-singlet heavy-quark coefficient functions $c_{2,q}^{(2,0)}$ the exact result for $a_{Qq,\mathrm{ps}}^{(3)0}$ of Ref. [115] is to be used in all cases.

The function $f(\xi) = (1 + e^{2(\xi-4)})^{-1}$ joins the asymptotic expressions for the large-ξ limit with the low-ξ region and provides a smooth transition between these two regimes. Here $c_{2,g}^{(2)\mathrm{LLx}}$ is the leading contribution given in Eq. (3.39) of Ref. [97]; $c_{2,q}^{(2)\mathrm{LLx}}$ is given by the same expression rescaled by C_F/C_A according to Eq. (14). Division of the factor $\ln x$ and substitution $\ln x \to -\ln \eta$ ensures the correct slope in η at all values of ξ, cf. Eq. (8).

The next-to-leading large-η terms denoted by $c_{2,i}^{(2)\mathrm{NLL}}$ are currently unknown in the low-ξ region, but we can derive constraints in the low-ξ region at high-η

$$c_{2,g}^{(2,0)\mathrm{NLL},A}(\xi) = 0.01\left(\frac{\ln \xi}{\ln 5}\right)^4 - 0.29, \qquad \text{(A3)}$$

$$c_{2,g}^{(2,0)\mathrm{NLL},B}(\xi) = 0.05\left(\frac{\ln \xi}{\ln 5}\right)^2 - 0.37, \qquad \text{(A4)}$$

as well as

$$c_{2,q}^{(2,0)\mathrm{NLL},A}(\xi) = 0.0045\left(\frac{\ln \xi}{\ln 5}\right)^4 - 0.1275, \qquad \text{(A5)}$$

$$c_{2,q}^{(2,0)\mathrm{NLL},B}(\xi) = 0.0175\left(\frac{\ln \xi}{\ln 5}\right)^2 - 0.1475. \qquad \text{(A6)}$$

These extrapolations are shown in Fig. 2 Finally, the matching is performed with the factors $\eta^\gamma/(C + \eta^\gamma)$ and $\eta^\delta/(D + \eta^\delta)$, respectively, where the suppression parameters γ, C and δ, D take the values

$$\gamma = 1.0, \quad C = 20.0, \text{ and } \delta = 0.8, \quad D = 10.7, \qquad \text{(A7)}$$

as determined in Ref. [97].

The new approximations to the NNLO Wilson coefficients in Eqs. (A1) and (A2) are available for numerical evaluation in the code `OPENQCDRAD` (version 2.0) [107].

APPENDIX B: CORRELATIONS

In Tables XIII–XV, we present the covariance matrix for the correlations of the fit parameters of ABMP16 discussed in Sec. III B, cf. Table VII and Eqs. (29) and (30) for the strong coupling α_s and the heavy-quark masses. Note, that in Eq. (29) we quote $\alpha_s^{(n_f=5)}(M_Z)$, whereas below the correlations are given for $\alpha_s^{(n_f=3)}(\mu_0)$ with $\mu_0 = 1.5$ GeV.

TABLE XIII. Correlation matrix of the fitted parameters for the PDFs, the strong coupling and the heavy-quark masses. Note, that $\alpha_s^{(n_f=3)}(\mu_0)$ is evaluated at the scale $\mu_0 = 1.5$ GeV.

	a_u	b_u	$\gamma_{1,u}$	$\gamma_{2,u}$	$\gamma_{3,u}$	a_d	b_d	$\gamma_{1,d}$	$\gamma_{2,d}$	$\gamma_{3,d}$
a_u	1.0	0.7617	0.9372	−0.5078	0.4839	0.4069	0.3591	0.4344	−0.3475	0.0001
b_u	0.7617	1.0	0.6124	−0.1533	−0.0346	0.3596	0.2958	0.3748	−0.2748	0.0001
$\gamma_{1,u}$	0.9372	0.6124	1.0	−0.7526	0.7154	0.2231	0.2441	0.2812	−0.2606	0.0001
$\gamma_{2,u}$	−0.5078	−0.1533	−0.7526	1.0	−0.9409	0.2779	0.2276	0.2266	−0.1860	0.0
$\gamma_{3,u}$	0.4839	−0.0346	0.7154	−0.9409	1.0	−0.1738	−0.1829	−0.1327	0.1488	0.0
a_d	0.4069	0.3596	0.2231	0.2779	−0.1738	1.0	0.7209	0.9697	−0.6529	0.0001
b_d	0.3591	0.2958	0.2441	0.2276	−0.1829	0.7209	1.0	0.7681	−0.9786	−0.0001
$\gamma_{1,d}$	0.4344	0.3748	0.2812	0.2266	−0.1327	0.9697	0.7681	1.0	−0.7454	0.0002
$\gamma_{2,d}$	−0.3475	−0.2748	−0.2606	−0.1860	0.1488	−0.6529	−0.9786	−0.7454	1.0	−0.0002
$\gamma_{3,d}$	0.0001	0.0001	0.0001	0.0	0.0	0.0001	−0.0001	0.0002	−0.0002	1.0
a_{us}	−0.0683	−0.0081	−0.2094	0.3881	−0.3206	0.2266	0.1502	0.2000	−0.1293	0.0
b_{us}	−0.3508	−0.3089	−0.3462	0.0906	−0.0537	−0.1045	−0.2000	−0.2241	0.2798	0.0
$\gamma_{-1,us}$	0.2296	0.1387	0.3367	−0.4043	0.3474	−0.1171	−0.1127	−0.0810	0.0767	0.0
$\gamma_{1,us}$	−0.4853	−0.4119	−0.3844	−0.0365	0.0064	−0.4380	−0.3592	−0.4957	0.3771	−0.0001
A_{us}	0.0506	0.0807	−0.0949	0.3198	−0.2560	0.2527	0.1648	0.2350	−0.1509	0.0
a_{ds}	−0.0759	−0.0443	−0.0951	0.0263	−0.0382	−0.2565	−0.2541	−0.2666	0.2380	0.0

(Table continued)

TABLE XIII. *(Continued)*

	a_u	b_u	$\gamma_{1,u}$	$\gamma_{2,u}$	$\gamma_{3,u}$	a_d	b_d	$\gamma_{1,d}$	$\gamma_{2,d}$	$\gamma_{3,d}$
b_{bs}	0.0452	−0.0197	0.0345	−0.0589	0.0683	−0.2084	0.0190	−0.1841	−0.0522	0.0
$\gamma_{1,ds}$	−0.0492	−0.0809	0.0101	−0.1791	0.1309	−0.5576	−0.2029	−0.4584	0.0946	0.0
A_{ds}	−0.1980	−0.1262	−0.2349	0.1526	−0.1428	−0.1113	−0.2167	−0.1739	0.2407	0.0
a_{ss}	−0.2034	−0.1285	−0.2362	0.2328	−0.2080	0.0960	0.1596	0.0661	−0.1054	0.0
b_{ss}	−0.1186	−0.0480	−0.1532	0.1549	−0.1536	0.0486	0.1508	0.0267	−0.1161	0.0
A_{ss}	−0.1013	−0.0411	−0.1458	0.1802	−0.1625	0.1216	0.1678	0.0924	−0.1196	0.0
a_g	0.0046	−0.0374	0.1109	−0.1934	0.1653	−0.0288	−0.0122	0.0053	0.0059	0.0
b_g	0.2662	0.3141	0.1579	−0.0050	−0.0207	0.0973	0.0870	0.0646	−0.0666	0.0
$\gamma_{1,g}$	0.2008	0.2274	0.0706	0.0876	−0.0835	0.0919	0.0574	0.0493	−0.0364	0.0
$\alpha_s^{(n_f=3)}(\mu_0)$	0.1083	−0.0607	0.0848	−0.0250	0.0765	0.0763	−0.0306	0.0725	0.0243	0.0
$m_c(m_c)$	−0.0006	0.0170	−0.0104	0.0206	−0.0201	−0.0123	−0.0161	−0.0114	0.0108	0.0
$m_b(m_b)$	0.0661	0.0554	0.0605	−0.0367	0.0287	−0.0116	0.0029	−0.0074	−0.0051	0.0
$m_t(m_t)$	−0.1339	−0.2170	−0.0816	0.0081	0.0250	−0.0616	−0.0813	−0.0491	0.0736	0.0

TABLE XIV. Table XIII continued.

	a_{us}	b_{us}	$\gamma_{-1,us}$	$\gamma_{1,us}$	A_{us}	a_{ds}	b_{bs}	$\gamma_{1,ds}$	A_{ds}	a_{ss}
a_u	−0.0683	−0.3508	0.2296	−0.4853	0.0506	−0.0759	0.0452	−0.0492	−0.1980	−0.2034
b_u	−0.0081	−0.3089	0.1387	−0.4119	0.0807	−0.0443	−0.0197	−0.0809	−0.1262	−0.1285
$\gamma_{1,u}$	−0.2094	−0.3462	0.3367	−0.3844	−0.0949	−0.0951	0.0345	0.0101	−0.2349	−0.2362
$\gamma_{2,u}$	0.3881	0.0906	−0.4043	−0.0365	0.3198	0.0263	−0.0589	−0.1791	0.1526	0.2328
$\gamma_{3,u}$	−0.3206	−0.0537	0.3474	0.0064	−0.2560	−0.0382	0.0683	0.1309	−0.1428	−0.2080
a_d	0.2266	−0.1045	−0.1171	−0.4380	0.2527	−0.2565	−0.2084	−0.5576	−0.1113	0.0960
b_d	0.1502	−0.2000	−0.1127	−0.3592	0.1648	−0.2541	0.0190	−0.2029	−0.2167	0.1596
$\gamma_{1,d}$	0.2000	−0.2241	−0.0810	−0.4957	0.2350	−0.2666	−0.1841	−0.4584	−0.1739	0.0661
$\gamma_{2,d}$	−0.1293	0.2798	0.0767	0.3771	−0.1509	0.2380	−0.0522	0.0946	0.2407	−0.1054
$\gamma_{3,d}$	0.0	0.0	0.0	−0.0001	0.0	0.0	0.0	0.0	0.0	0.0
a_{us}	1.0	−0.3156	−0.8947	−0.5310	0.9719	0.2849	0.0241	−0.0470	0.2983	0.4131
b_{us}	−0.3156	1.0	0.1372	0.8258	−0.3995	0.0467	−0.0221	−0.1190	0.1856	0.0291
$\gamma_{-1,us}$	−0.8947	0.1372	1.0	0.2611	−0.7829	−0.1695	0.0156	0.0501	−0.2117	−0.7191
$\gamma_{1,us}$	−0.5310	0.8258	0.2611	1.0	−0.6479	0.0086	0.0076	0.1460	0.0781	−0.0010
A_{us}	0.9719	−0.3995	−0.7829	−0.6479	1.0	0.2983	0.0515	−0.0404	0.3055	0.2811
a_{ds}	0.2849	0.0467	−0.1695	0.0086	0.2983	1.0	−0.1608	0.0719	0.9152	−0.2941
b_{bs}	0.0241	−0.0221	0.0156	0.0076	0.0515	−0.1608	1.0	0.7834	−0.3022	−0.0390
$\gamma_{1,ds}$	−0.0470	−0.1190	0.0501	0.1460	−0.0404	0.0719	0.7834	1.0	−0.1838	−0.1373
A_{ds}	0.2983	0.1856	−0.2117	0.0781	0.3055	0.9152	−0.3022	−0.1838	1.0	−0.1833
a_{ss}	0.4131	0.0291	−0.7191	−0.0010	0.2811	−0.2941	−0.0390	−0.1373	−0.1833	1.0
b_{ss}	0.2197	0.0643	−0.4479	0.1286	0.1193	−0.1579	−0.0260	0.0169	−0.0896	0.6522
A_{ss}	0.3627	0.0261	−0.6319	0.0102	0.2412	−0.2688	−0.0180	−0.0960	−0.1797	0.9280
a_g	−0.2570	0.0001	0.2196	0.0039	−0.2493	−0.2190	−0.0454	−0.1031	−0.2571	0.0626
b_g	−0.1419	0.1266	0.0694	0.2648	−0.1715	−0.0515	0.0917	0.2130	−0.0469	−0.0092
$\gamma_{1,g}$	−0.0241	0.0332	−0.0226	0.1296	−0.0489	−0.0137	0.0503	0.1409	0.0022	−0.0279
$\alpha_s^{(n_f=3)}(\mu_0)$	0.0954	−0.2866	−0.0341	−0.3493	0.1110	−0.0604	−0.1265	−0.1811	−0.1330	−0.0841
$m_c(m_c)$	0.0704	−0.0093	−0.0033	−0.0462	0.1182	0.0849	0.0547	0.0413	0.1193	−0.0728
$m_b(m_b)$	−0.0183	−0.0132	0.0044	0.0209	−0.0298	−0.0006	0.0332	0.0695	−0.0432	−0.0159
$m_t(m_t)$	0.0641	−0.1841	−0.0408	−0.2635	0.0755	−0.0573	−0.1067	−0.2003	−0.0869	0.0169

TABLE XV. Table XIII continued.

	b_{ss}	A_{ss}	a_g	b_g	$\gamma_{1,g}$	$\alpha_s^{(n_f=3)}(\mu_0)$	$m_c(m_c)$	$m_b(m_b)$	$m_t(m_t)$
a_u	−0.1186	−0.1013	0.0046	0.2662	0.2008	0.1083	−0.0006	0.0661	−0.1339
b_u	−0.0480	−0.0411	−0.0374	0.3141	0.2274	−0.0607	0.0170	0.0554	−0.2170
$\gamma_{1,u}$	−0.1532	−0.1458	0.1109	0.1579	0.0706	0.0848	−0.0104	0.0605	−0.0816
$\gamma_{2,u}$	0.1549	0.1802	−0.1934	−0.0050	0.0876	−0.0250	0.0206	−0.0367	0.0081
$\gamma_{3,u}$	−0.1536	−0.1625	0.1653	−0.0207	−0.0835	0.0765	−0.0201	0.0287	0.0250
a_d	0.0486	0.1216	−0.0288	0.0973	0.0919	0.0763	−0.0123	−0.0116	−0.0616
b_d	0.1508	0.1678	−0.0122	0.0870	0.0574	−0.0306	−0.0161	0.0029	−0.0813
$\gamma_{1,d}$	0.0267	0.0924	0.0053	0.0646	0.0493	0.0725	−0.0114	−0.0074	−0.0491
$\gamma_{2,d}$	−0.1161	−0.1196	0.0059	−0.0666	−0.0364	0.0243	0.0108	−0.0051	0.0736
$\gamma_{3,d}$	0.0	0.0	0.0	0.0	0.0	0.0	0.0	0.0	0.0
a_{us}	0.2197	0.3627	−0.2570	−0.1419	−0.0241	0.0954	0.0704	−0.0183	0.0641
b_{us}	0.0643	0.0261	0.0001	0.1266	0.0332	−0.2866	−0.0093	−0.0132	−0.1841
$\gamma_{-1,us}$	−0.4479	−0.6319	0.2197	0.0694	−0.0226	−0.0341	−0.0034	0.0044	−0.0408
$\gamma_{1,us}$	0.1286	0.0102	0.0039	0.2648	0.1296	−0.3493	−0.0462	0.0209	−0.2635
A_{us}	0.1193	0.2412	−0.2493	−0.1715	−0.0489	0.1110	0.1182	−0.0298	0.0755
a_{ds}	−0.1579	−0.2688	−0.2190	−0.0515	−0.0137	−0.0604	0.0849	−0.0006	−0.0573
b_{bs}	−0.0260	−0.0180	−0.0454	0.0917	0.0503	−0.1265	0.0547	0.0332	−0.1067
$\gamma_{1,ds}$	0.0169	−0.0960	−0.1031	0.2130	0.1409	−0.1811	0.0413	0.0695	−0.2003
A_{ds}	−0.0896	−0.1797	−0.2571	−0.0469	0.0022	−0.1330	0.1193	−0.0432	−0.0869
a_{ss}	0.6522	0.9280	0.0626	−0.0092	−0.0279	−0.0841	−0.0728	−0.0159	0.0169
b_{ss}	1.0	0.6427	−0.0179	0.1967	0.1164	−0.2390	−0.0965	0.0169	−0.1675
A_{ss}	0.6427	1.0	−0.0211	0.1403	0.0997	−0.1385	0.0216	0.0072	−0.1109
a_g	−0.0179	−0.0211	1.0	−0.5279	−0.8046	0.1838	−0.2829	0.0076	0.3310
b_g	0.1967	0.1403	−0.5279	1.0	0.8837	−0.5124	0.1438	0.1255	−0.7275
$\gamma_{1,g}$	0.1164	0.0997	−0.8046	0.8837	1.0	−0.2511	0.1829	0.0814	−0.5180
$\alpha_s^{(n_f=3)}(\mu_0)$	−0.2390	−0.1385	0.1838	−0.5124	−0.2511	1.0	−0.1048	0.0423	0.6924
$m_c(m_c)$	−0.0965	0.0216	−0.2829	0.1438	0.1829	−0.1048	1.0	0.0328	−0.1577
$m_b(m_b)$	0.0169	0.0072	0.0076	0.1255	0.0814	0.0423	0.0328	1.0	−0.0900
$m_t(m_t)$	−0.1675	−0.1109	0.3310	−0.7275	−0.5180	0.6924	−0.1577	−0.0900	1.0

[1] S. Alekhin, J. Blümlein, and S. Moch, Phys. Rev. D **89**, 054028 (2014).

[2] S. Alekhin, J. Blümlein, L. Caminada, K. Lipka, K. Lohwasser, S. Moch, R. Petti, and R. Plačakytė, Phys. Rev. D **91**, 094002 (2015).

[3] S. Alekhin, J. Blümlein, S. Moch, and R. Placakyte, Phys. Rev. D **94**, 114038 (2016).

[4] H. Abramowicz *et al.* (H1 and ZEUS Collaborations), Eur. Phys. J. C **75**, 580 (2015).

[5] S. Alekhin, J. Blümlein, S. Klein, and S. Moch, Phys. Rev. D **81**, 014032 (2010).

[6] A. Accardi, L. T. Brady, W. Melnitchouk, J. F. Owens, and N. Sato, Phys. Rev. D **93**, 114017 (2016).

[7] S. Dulat, T.-J. Hou, J. Gao, M. Guzzi, J. Huston, P. Nadolsky, J. Pumplin, C. Schmidt, D. Stump, and C.-P. Yuan, Phys. Rev. D **93**, 033006 (2016).

[8] P. Jimenez-Delgado and E. Reya, Phys. Rev. D **89**, 074049 (2014).

[9] L. A. Harland-Lang, A. D. Martin, P. Motylinski, and R. S. Thorne, Eur. Phys. J. C **75**, 204 (2015).

[10] R. D. Ball *et al.* (NNPDF Collaboration), J. High Energy Phys. 04 (2015) 040.

[11] A. Accardi *et al.*, Eur. Phys. J. C **76**, 471 (2016).

[12] F. Bezrukov, M. Yu. Kalmykov, B. A. Kniehl, and M. Shaposhnikov, J. High Energy Phys. 10 (2012) 140.

[13] G. Degrassi, S. Di Vita, J. Elias-Miró, J. R. Espinosa, G. F. Giudice, G. Isidori, and A. Strumia, J. High Energy Phys. 08 (2012) 098.

[14] A. Buckley, J. Ferrando, S. Lloyd, K. Nordström, B. Page, M. Rüfenacht, M. Schönherr, and G. Watt, Eur. Phys. J. C **75**, 132 (2015).

[15] F. D. Aaron *et al.* (H1 Collaboration), Eur. Phys. J. C **65**, 89 (2010).

[16] H. Abramowicz *et al.* (ZEUS Collaboration), J. High Energy Phys. 09 (2014) 127.

[17] O. Samoylov *et al.* (NOMAD Collaboration), Nucl. Phys. **B876**, 339 (2013).

[18] A. Kayis-Topaksu *et al.* (CHORUS Collaboration), New J. Phys. **13**, 093002 (2011).

[19] R. Aaij *et al.* (LHCb Collaboration), J. High Energy Phys. 08 (2015) 039.

[20] R. Aaij *et al.* (LHCb Collaboration), J. High Energy Phys. 01 (2016) 155.

[21] R. Aaij *et al.* (LHCb Collaboration), J. High Energy Phys. 05 (2015) 109.

[22] V. M. Abazov *et al.* (D0 Collaboration), Phys. Rev. D **91**, 032007 (2015); **91**, 079901(E) (2015).

[23] V. M. Abazov *et al.* (D0 Collaboration), Phys. Rev. D **88**, 091102 (2013).

[24] S. Chatrchyan *et al.* (CMS Collaboration), Phys. Rev. D **90**, 032004 (2014).

[25] V. Khachatryan *et al.* (CMS Collaboration), Eur. Phys. J. C **76**, 469 (2016).

[26] G. Aad *et al.* (ATLAS Collaboration), Phys. Lett. B **759**, 601 (2016).

[27] G. Aad *et al.* (ATLAS Collaboration), Phys. Rev. D **90**, 112006 (2014).

[28] P. Tepel (ATLAS Collaboration), arXiv:1411.7627.

[29] M. Aaboud *et al.* (ATLAS Collaboration), J. High Energy Phys. 04 (2017) 086.

[30] S. Chatrchyan *et al.* (CMS Collaboration), J. High Energy Phys. 12 (2012) 035.

[31] V. Khachatryan *et al.* (CMS Collaboration), J. High Energy Phys. 06 (2014) 090.

[32] A. M. Sirunyan *et al.* (CMS Collaboration), arXiv: 1610.00678.

[33] G. Aad *et al.* (ATLAS Collaboration), Phys. Rev. D **91**, 052005 (2015).

[34] V. Khachatryan *et al.* (CMS Collaboration), J. High Energy Phys. 08 (2016) 029.

[35] V. Khachatryan *et al.* (CMS Collaboration), Phys. Rev. Lett. **116**, 052002 (2016).

[36] G. Aad *et al.* (ATLAS Collaboration), Eur. Phys. J. C **74**, 3109 (2014).

[37] M. Aaboud *et al.* (ATLAS Collaboration), Phys. Lett. B **761**, 136 (2016).

[38] V. Khachatryan *et al.* (CMS Collaboration), Eur. Phys. J. C **77**, 172 (2017).

[39] V. Khachatryan *et al.* (CMS Collaboration), Eur. Phys. J. C **77**, 15 (2017).

[40] G. Aad *et al.* (ATLAS Collaboration), Phys. Rev. D **91**, 112013 (2015).

[41] CMS Collaboration, CERN Report No. CMS-PAS-TOP-15-005, 2015 (unpublished).

[42] ATLAS Collaboration, CERN Report No. ATLAS-CONF-2012-131, 2012 (unpublished).

[43] G. Aad *et al.* (ATLAS Collaboration), Phys. Rev. D **92**, 072005 (2015).

[44] S. Chatrchyan *et al.* (CMS Collaboration), Phys. Rev. D **85**, 112007 (2012).

[45] V. Khachatryan *et al.* (CMS Collaboration), Eur. Phys. J. C **76**, 128 (2016).

[46] G. Aad *et al.* (ATLAS Collaboration), Eur. Phys. J. C **73**, 2328 (2013).

[47] S. Chatrchyan *et al.* (CMS Collaboration), Eur. Phys. J. C **73**, 2386 (2013).

[48] ATLAS Collaboration, CERN Report No. ATLAS-CONF-2012-031, 2012 (unpublished).

[49] S. Chatrchyan *et al.* (CMS Collaboration), J. High Energy Phys. 05 (2013) 065.

[50] CMS Collaboration, CERN Report No. CMS-PAS-TOP-16-013, 2016 (unpublished).

[51] V. Khachatryan *et al.* (CMS Collaboration), Phys. Lett. B **739**, 23 (2014).

[52] CMS Collaboration, CERN Report No. CMS-PAS-TOP-16-015, 2016 (unpublished).

[53] T. A. Aaltonen *et al.* (CDF and D0 Collaborations), Phys. Rev. Lett. **115**, 152003 (2015).

[54] A. Bodek *et al.*, Phys. Rev. D **20**, 1471 (1979).

[55] W. B. Atwood, E. D. Bloom, R. L. A. Cottrell, H. DeStaebler, M. Mestayer, C. Y. Prescott, L. S. Rochester, S. Stein, R. E. Taylor, and D. Trines, Phys. Lett. **64B**, 479 (1976).

[56] M. D. Mestayer, W. B. Atwood, E. D. Bloom, R. L. A. Cottrell, H. DeStaebler, C. Y. Prescott, L. S. Rochester, S. Stein, R. E. Taylor, and D. Trines, Phys. Rev. D **27**, 285 (1983).

[57] J. Gomez *et al.*, Phys. Rev. D **49**, 4348 (1994).

[58] S. Dasu *et al.*, Phys. Rev. D **49**, 5641 (1994).

[59] A. C. Benvenuti *et al.* (BCDMS Collaboration), Phys. Lett. B **237**, 592 (1990).

[60] M. Arneodo *et al.* (New Muon Collaboration), Nucl. Phys. **B483**, 3 (1997).

[61] A. C. Benvenuti *et al.* (BCDMS Collaboration), Phys. Lett. B **223**, 485 (1989).

[62] L. W. Whitlow *et al.*, Phys. Lett. B **250**, 193 (1990).

[63] H. Abramowicz *et al.* (ZEUS and H1 Collaborations), Eur. Phys. J. C **73**, 2311 (2013).

[64] M. Goncharov *et al.* (NuTeV Collaboration), Phys. Rev. D **64**, 112006 (2001).

[65] N. Ushida *et al.* (Fermilab E531 Collaboration), Phys. Lett. B **206**, 375 (1988).

[66] M. Aaboud *et al.* (ATLAS Collaboration), Eur. Phys. J. C **77**, 367 (2017).

[67] G. Aad *et al.* (ATLAS Collaboration), Phys. Rev. D **85**, 072004 (2012).

[68] G. Moreno *et al.*, Phys. Rev. D **43**, 2815 (1991).

[69] NuSea, R. S. Towell *et al.*, Phys. Rev. D **64**, 052002 (2001).

[70] V. M. Abazov *et al.* (D0 Collaboration), Phys. Rev. Lett. **112**, 151803 (2014); **114**, 049901(E) (2015).

[71] S. Alekhin, J. Blümlein, and S. Moch, Phys. Rev. D **86**, 054009 (2012).

[72] T. A. Aaltonen *et al.* (CDF and D0 Collaborations), Phys. Rev. D **89**, 072001 (2014).

[73] K. G. Wilson, Phys. Rev. **179**, 1499 (1969).
[74] W. Zimmermann, *Lectures on Elementary Particle Physics and Quantum Field Theory*, Brandeis Summer Institute Vol. 1 (MIT Press, Cambridge, MA, 1970), p. 395.
[75] R. A. Brandt and G. Preparata, Nucl. Phys. **B27**, 541 (1971).
[76] Y. Frishman, Ann. Phys. (N.Y.) **66**, 373 (1971).
[77] N. H. Christ, B. Hasslacher, and A. H. Mueller, Phys. Rev. D **6**, 3543 (1972).
[78] H. D. Politzer, Phys. Rep. **14**, 129 (1974).
[79] E. Reya, Phys. Rep. **69**, 195 (1981).
[80] S. Moch, J. A. M. Vermaseren, and A. Vogt, Nucl. Phys. **B688**, 101 (2004).
[81] A. Vogt, S. Moch, and J. A. M. Vermaseren, Nucl. Phys. **B691**, 129 (2004).
[82] P. A. Baikov, K. G. Chetyrkin, and J. H. Kühn, Nucl. Part. Phys. Proc. **261–262**, 3 (2015).
[83] V. N. Velizhanin, Nucl. Phys. **B860**, 288 (2012).
[84] V. N. Velizhanin, arXiv:1411.1331.
[85] B. Ruijl, T. Ueda, J. A. M. Vermaseren, J. Davies, and A. Vogt, Proc. Sci., LL2016 (**2016**) 071 [arXiv:1605.08408].
[86] J. Davies, A. Vogt, B. Ruijl, T. Ueda, and J. A. M. Vermaseren, Nucl. Phys. **B915**, 335 (2017).
[87] H. D. Politzer, Nucl. Phys. **B129**, 301 (1977).
[88] D. Amati, R. Petronzio, and G. Veneziano, Nucl. Phys. **B140**, 54 (1978).
[89] D. Amati, R. Petronzio, and G. Veneziano, Nucl. Phys. **B146**, 29 (1978).
[90] S. B. Libby and G. F. Sterman, Phys. Rev. D **18**, 3252 (1978).
[91] S. B. Libby and G. F. Sterman, Phys. Rev. D **18**, 4737 (1978).
[92] A. H. Mueller, Phys. Rev. D **18**, 3705 (1978).
[93] J. C. Collins and G. F. Sterman, Nucl. Phys. **B185**, 172 (1981).
[94] J. C. Collins, D. E. Soper, and G. F. Sterman, Nucl. Phys. **B261**, 104 (1985).
[95] G. T. Bodwin, Phys. Rev. D **31**, 2616 (1985); **34**, 3932(E) (1986).
[96] S. Moch, J. A. M. Vermaseren, and A. Vogt, Phys. Lett. B **606**, 123 (2005).
[97] H. Kawamura, N. A. Lo Presti, S. Moch, and A. Vogt, Nucl. Phys. **B864**, 399 (2012).
[98] J. A. M. Vermaseren, A. Vogt, and S. Moch, Nucl. Phys. **B724**, 3 (2005).
[99] S. Moch, J. A. M. Vermaseren, and A. Vogt, Nucl. Phys. **B813**, 220 (2009).
[100] T. Gottschalk, Phys. Rev. D **23**, 56 (1981).
[101] M. Glück, S. Kretzer, and E. Reya, Phys. Lett. B **380**, 171 (1996); **405**, 391(E) (1997).
[102] J. Blümlein, A. Hasselhuhn, P. Kovacikova, and S. Moch, Phys. Lett. B **700**, 294 (2011).
[103] M. Buza and W. L. van Neerven, Nucl. Phys. **B500**, 301 (1997).
[104] S. Moch (unpublished).
[105] J. Blümlein, A. Hasselhuhn, and T. Pfoh, Nucl. Phys. **B881**, 1 (2014).
[106] E. L. Berger, J. Gao, C. S. Li, Z. L. Liu, and H. X. Zhu, Phys. Rev. Lett. **116**, 212002 (2016).
[107] S. Alekhin, OPENQCDRAD, http://www-zeuthen.desy.de/~alekhin/OPENQCDRAD.
[108] S. Alekhin and S. Moch, Phys. Lett. B **699**, 345 (2011).
[109] A. D. Martin, R. G. Roberts, W. J. Stirling, and R. S. Thorne, Phys. Lett. B **531**, 216 (2002).
[110] J. Blümlein, H. Böttcher, and A. Guffanti, Nucl. Phys. **B774**, 182 (2007).
[111] D. Boer *et al.*, arXiv:1108.1713.
[112] J. L. A. Fernandez *et al.* (LHeC Study Group Collaboration), J. Phys. G **39**, 075001 (2012).
[113] H. Georgi and H. D. Politzer, Phys. Rev. D **9**, 416 (1974).
[114] J. Ablinger, J. Blümlein, S. Klein, C. Schneider, and F. Wißbrock, Nucl. Phys. **B844**, 26 (2011).
[115] J. Ablinger *et al.*, Nucl. Phys. **B890**, 48 (2014).
[116] J. Ablinger, J. Blümlein, A. De Freitas, A. Hasselhuhn, A. von Manteuffel, M. Round, C. Schneider, and F. Wißbrock, Nucl. Phys. **B882**, 263 (2014).
[117] A. Behring, J. Blümlein, A. De Freitas, A. Hasselhuhn, A. von Manteuffel, and C. Schneider, Phys. Rev. D **92**, 114005 (2015).
[118] A. Behring, I. Bierenbaum, J. Blümlein, A. De Freitas, S. Klein, and F. Wißbrock, Eur. Phys. J. C **74**, 3033 (2014).
[119] I. Bierenbaum, J. Blümlein, and S. Klein, Nucl. Phys. **B820**, 417 (2009).
[120] A. P. Bukhvostov, G. V. Frolov, L. N. Lipatov, and E. A. Kuraev, Nucl. Phys. **B258**, 601 (1985).
[121] I. Abt, A. M. Cooper-Sarkar, B. Foster, V. Myronenko, K. Wichmann, and M. Wing, Phys. Rev. D **94**, 034032 (2016).
[122] M. Osipenko, W. Melnitchouk, S. Simula, P. Bosted, V. Burkert, M. E. Christy, K. Griffioen, C. Keppel, and S. E. Kuhn, Phys. Lett. B **609**, 259 (2005).
[123] B. Geyer, M. Lazar, and D. Robaschik, Nucl. Phys. **B559**, 339 (1999).
[124] B. Geyer and M. Lazar, Nucl. Phys. **B581**, 341 (2000).
[125] S. Gottlieb, Ph.D. thesis, Princeton University, 1978.
[126] S. A. Gottlieb, Nucl. Phys. **B139**, 125 (1978).
[127] C. S. Lam and M. A. Walton, Can. J. Phys. **63**, 1042 (1985).
[128] H. D. Politzer, Nucl. Phys. **B172**, 349 (1980).
[129] M. Okawa, Nucl. Phys. **B172**, 481 (1980).
[130] M. Okawa, Nucl. Phys. **B187**, 71 (1981).
[131] S. Wada, Nucl. Phys. **B202**, 201 (1982).
[132] S. Wada, Phys. Lett. **119B**, 427 (1982).
[133] S. P. Luttrell, S. Wada, and B. R. Webber, Nucl. Phys. **B188**, 219 (1981).
[134] S. P. Luttrell and S. Wada, Nucl. Phys. **B197**, 290 (1982); **B206**, 497(E) (1982).
[135] E. V. Shuryak and A. I. Vainshtein, Phys. Lett. **105B**, 65 (1981).
[136] E. V. Shuryak and A. I. Vainshtein, Nucl. Phys. **B199**, 451 (1982).
[137] E. V. Shuryak and A. I. Vainshtein, Nucl. Phys. **B201**, 141 (1982).
[138] R. L. Jaffe and M. Soldate, Phys. Lett. **105B**, 467 (1981).
[139] R. L. Jaffe and M. Soldate, Phys. Rev. D **26**, 49 (1982).
[140] R. L. Jaffe, Nucl. Phys. **B229**, 205 (1983).
[141] R. K. Ellis, W. Furmanski, and R. Petronzio, Nucl. Phys. **B207**, 1 (1982).

[142] R. K. Ellis, W. Furmanski, and R. Petronzio, Nucl. Phys. **B212**, 29 (1983).
[143] A. P. Bukhvostov and G. V. Frolov, Yad. Fiz. **45**, 1136 (1987).
[144] J.-W. Qiu, Phys. Rev. D **42**, 30 (1990).
[145] J. Bartels, C. Bontus, and H. Spiesberger, arXiv:hep-ph/9908411.
[146] V. Braun, R. J. Fries, N. Mahnke, and E. Stein, Nucl. Phys. **B589**, 381 (2000); **B607**, 433(E) (2001).
[147] V. M. Braun, A. N. Manashov, and J. Rohrwild, Nucl. Phys. **B807**, 89 (2009).
[148] V. M. Braun, A. N. Manashov, and J. Rohrwild, Nucl. Phys. **B826**, 235 (2010).
[149] M. J. Glatzmaier, S. Mantry, and M. J. Ramsey-Musolf, Phys. Rev. C **88**, 025202 (2013).
[150] V. M. Braun and A. V. Kolesnichenko, Nucl. Phys. **B283**, 723 (1987).
[151] I. I. Balitsky, V. M. Braun, and A. V. Kolesnichenko, Pis'ma Zh. Eksp. Teor. Fiz. **50**, 54 (1989) [JETP Lett. **50**, 61 (1989)].
[152] I. I. Balitsky, V. M. Braun, and A. V. Kolesnichenko, Phys. Lett. B **242**, 245 (1990); **318**, 648(E) (1993).
[153] M. Dasgupta and B. R. Webber, Phys. Lett. B **382**, 273 (1996).
[154] M. Beneke, Phys. Rep. **317**, 1 (1999).
[155] M. Beneke and V. M. Braun, arXiv:hep-ph/0010208.
[156] J. Blümlein and H. Böttcher, Phys. Lett. B **662**, 336 (2008).
[157] J. Blümlein and H. Böttcher, arXiv:1207.3170.
[158] F. Eisele, M. Glück, E. Hoffmann, and E. Reya, Phys. Rev. D **26**, 41 (1982).
[159] K. Varvell *et al.* (BEBC WA59 Collaboration), Z. Phys. C **36**, 1 (1987).
[160] M. Virchaux and A. Milsztajn, Phys. Lett. B **274**, 221 (1992).
[161] A. L. Kataev, A. V. Kotikov, G. Parente, and A. V. Sidorov, Phys. Lett. B **417**, 374 (1998).
[162] S. I. Alekhin and A. L. Kataev, Phys. Lett. B **452**, 402 (1999).
[163] M. Botje, Eur. Phys. J. C **14**, 285 (2000).
[164] S. I. Alekhin, Phys. Rev. D **63**, 094022 (2001).
[165] S. I. Alekhin, S. A. Kulagin, and S. Liuti, Phys. Rev. D **69**, 114009 (2004).
[166] S. Alekhin, S. A. Kulagin, and R. Petti, AIP Conf. Proc. **967**, 215 (2007).
[167] S. Moch, J. A. M. Vermaseren, and A. Vogt, Nucl. Phys. **B726**, 317 (2005).
[168] V. Ravindran, Nucl. Phys. **B752**, 173 (2006).
[169] S. Riemersma, J. Smith, and W. L. van Neerven, Phys. Lett. B **347**, 143 (1995).
[170] E. Laenen, S. Riemersma, J. Smith, and W. L. van Neerven, Nucl. Phys. **B392**, 162 (1993).
[171] B. W. Harris and J. Smith, Nucl. Phys. **B452**, 109 (1995).
[172] E. Laenen and S. Moch, Phys. Rev. D **59**, 034027 (1999).
[173] S. Catani, M. Ciafaloni, and F. Hautmann, Nucl. Phys. **B366**, 135 (1991).
[174] I. Bierenbaum, J. Blümlein, S. Klein, and C. Schneider, Nucl. Phys. **B803**, 1 (2008).
[175] I. Bierenbaum, J. Blümlein, and S. Klein, Phys. Lett. B **672**, 401 (2009).
[176] E. B. Zijlstra and W. L. van Neerven, Nucl. Phys. **B383**, 525 (1992).
[177] S. Moch and J. A. M. Vermaseren, Nucl. Phys. **B573**, 853 (2000).
[178] J. Blümlein, A. Hasselhuhn, S. Klein, and C. Schneider, Nucl. Phys. **B866**, 196 (2013).
[179] W. L. van Neerven and A. Vogt, Phys. Lett. B **490**, 111 (2000).
[180] A. Behring, J. Blümlein, G. Falcioni, A. De Freitas, A. von Manteuffel, and C. Schneider, Phys. Rev. D **94**, 114006 (2016).
[181] Y. Li and F. Petriello, Phys. Rev. D **86**, 094034 (2012).
[182] R. Gavin, Y. Li, F. Petriello, and S. Quackenbush, Comput. Phys. Commun. **184**, 209 (2013).
[183] M. Buza, Y. Matiounine, J. Smith, and W. L. van Neerven, Eur. Phys. J. C **1**, 301 (1998).
[184] P. Bärnreuther, M. Czakon, and A. Mitov, Phys. Rev. Lett. **109**, 132001 (2012).
[185] M. Czakon and A. Mitov, J. High Energy Phys. 12 (2012) 054.
[186] M. Czakon and A. Mitov, J. High Energy Phys. 01 (2013) 080.
[187] M. Czakon, P. Fiedler, and A. Mitov, Phys. Rev. Lett. **110**, 252004 (2013).
[188] U. Langenfeld, S. Moch, and P. Uwer, Phys. Rev. D **80**, 054009 (2009).
[189] M. Aliev, H. Lacker, U. Langenfeld, S. Moch, P. Uwer, and M. Wiedermann, Comput. Phys. Commun. **182**, 1034 (2011).
[190] M. Dowling and S. Moch, Eur. Phys. J. C **74**, 3167 (2014).
[191] M. Brucherseifer, F. Caola, and K. Melnikov, Phys. Lett. B **736**, 58 (2014).
[192] E. L. Berger, J. Gao, C. P. Yuan, and H. X. Zhu, Phys. Rev. D **94**, 071501 (2016).
[193] S. Alekhin, S. Moch, and S. Thier, Phys. Lett. B **763**, 341 (2016).
[194] M. C. Smith and S. Willenbrock, Phys. Rev. D **54**, 6696 (1996).
[195] B. W. Harris, E. Laenen, L. Phaf, Z. Sullivan, and S. Weinzierl, Phys. Rev. D **66**, 054024 (2002).
[196] N. Kidonakis, Phys. Rev. D **74**, 114012 (2006).
[197] N. Kidonakis, Phys. Rev. D **75**, 071501 (2007).
[198] N. Kidonakis, Phys. Rev. D **81**, 054028 (2010).
[199] P. Kant, O. M. Kind, T. Kintscher, T. Lohse, T. Martini, S. Mölbitz, P. Rieck, and P. Uwer, Comput. Phys. Commun. **191**, 74 (2015).
[200] C. Patrignani *et al.* (Particle Data Group Collaboration), Chin. Phys. C **40**, 100001 (2016).
[201] S. Camarda *et al.* (HERAFitter developers' Team Collaboration), Eur. Phys. J. C **75**, 458 (2015).
[202] R. Aaij *et al.* (LHCb Collaboration), J. High Energy Phys. 10 (2016) 030.
[203] R. Aaij *et al.* (LHCb Collaboration), J. High Energy Phys. 09 (2016) 136.
[204] S. Catani and M. Grazzini, Phys. Rev. Lett. **98**, 222002 (2007).
[205] S. Catani, L. Cieri, G. Ferrera, D. de Florian, and M. Grazzini, Phys. Rev. Lett. **103**, 082001 (2009).
[206] S. Alekhin *et al.*, Eur. Phys. J. C **75**, 304 (2015).
[207] S. A. Kulagin and R. Petti, Nucl. Phys. **A765**, 126 (2006).
[208] S. A. Kulagin and R. Petti, Phys. Rev. D **76**, 094023 (2007).

[209] S. I. Alekhin, S. A. Kulagin, and R. Petti, arXiv:1609.08463.

[210] G. Aad *et al.* (ATLAS Collaboration), Phys. Rev. Lett. **109**, 012001 (2012).

[211] G. Aad *et al.* (ATLAS Collaboration), J. High Energy Phys. 05 (2014) 068.

[212] S. Chatrchyan *et al.* (CMS Collaboration), J. High Energy Phys. 02 (2014) 013.

[213] F. D. Aaron *et al.* (ZEUS and H1 Collaborations), J. High Energy Phys. 01 (2010) 109.

[214] F. D. Aaron *et al.* (H1 Collaboration), Eur. Phys. J. C **71**, 1579 (2011).

[215] S. Alekhin, J. Blümlein, and S. Moch, Eur. Phys. J. C **71**, 1723 (2011).

[216] S. Alekhin, J. Blümlein, and S. O. Moch, Mod. Phys. Lett. A **31**, 1630023 (2016).

[217] M. Bruno *et al.*, Proc. Sci., LATTICE2016 (**2016**) 197, arXiv:1701.03075.

[218] S. Aoki *et al.*, Eur. Phys. J. C **77**, 112 (2017).

[219] S. Alekhin, J. Blümlein, K. Daum, K. Lipka, and S. Moch, Phys. Lett. B **720**, 172 (2013).

[220] J. Kieseler, K. Lipka, and S. Moch, Phys. Rev. Lett. **116**, 162001 (2016).

[221] K. G. Chetyrkin, J. H. Kühn, and M. Steinhauser, Comput. Phys. Commun. **133**, 43 (2000).

[222] P. Marquard, A. V. Smirnov, V. A. Smirnov, and M. Steinhauser, Phys. Rev. Lett. **114**, 142002 (2015).

[223] V. Bertone *et al.* (xFitter Developers' Team Collaboration), J. High Energy Phys. 08 (2016) 050.

[224] J. Gao, M. Guzzi, and P. M. Nadolsky, Eur. Phys. J. C **73**, 2541 (2013).

[225] O. Zenaiev *et al.* (PROSA Collaboration), Eur. Phys. J. C **75**, 396 (2015).

[226] R. D. Ball, V. Bertone, F. Cerutti, L. D. Debbio, S. Forte, A. Guffanti, J. I. Latorre, J. Rojo, and M. Ubiali, Nucl. Phys. **B849**, 296 (2011).

[227] L. A. Harland-Lang, A. D. Martin, P. Motylinski, and R. S. Thorne, Eur. Phys. J. C **76**, 10 (2016).

[228] C. Alexandrou, J. Carbonell, M. Constantinou, P. A. Harraud, P. Guichon, K. Jansen, C. Kallidonis, T. Korzec, and M. Papinutto, Phys. Rev. D **83**, 114513 (2011).

[229] C. Alexandrou, M. Constantinou, S. Dinter, V. Drach, K. Jansen, C. Kallidonis, and G. Koutsou, Phys. Rev. D **88**, 014509 (2013).

[230] A. Abdel-Rehim *et al.*, Phys. Rev. D **92**, 114513 (2015); **93**, 039904(E) (2016).

[231] C. Alexandrou *et al.*, Proc. Sci., LATTICE2016 (**2016**) 153 [arXiv:1611.09163].

[232] M. Spira, A. Djouadi, D. Graudenz, and P. M. Zerwas, Nucl. Phys. **B453**, 17 (1995).

[233] R. V. Harlander and W. B. Kilgore, Phys. Rev. Lett. **88**, 201801 (2002).

[234] C. Anastasiou and K. Melnikov, Nucl. Phys. **B646**, 220 (2002).

[235] V. Ravindran, J. Smith, and W. L. van Neerven, Nucl. Phys. **B665**, 325 (2003).

[236] C. Anastasiou, C. Duhr, F. Dulat, F. Herzog, and B. Mistlberger, Phys. Rev. Lett. **114**, 212001 (2015).

[237] C. Anastasiou, C. Duhr, F. Dulat, E. Furlan, T. Gehrmann, F. Herzog, A. Lazopoulos, and B. Mistlberger, J. High Energy Phys. 05 (2016) 058.

[238] D. de Florian, J. Mazzitelli, S. Moch, and A. Vogt, J. High Energy Phys. 10 (2014) 176.

[239] J. Butterworth *et al.*, J. Phys. G **43**, 023001 (2016).

[240] D. de Florian *et al.* (LHC Higgs Cross Section Working Group Collaboration), arXiv:1610.07922.

[241] G. Aad *et al.* (ATLAS and CMS Collaborations), Phys. Rev. Lett. **114**, 191803 (2015).

[242] L. N. Mihaila, J. Salomon, and M. Steinhauser, Phys. Rev. Lett. **108**, 151602 (2012).

[243] A. V. Bednyakov, A. F. Pikelner, and V. N. Velizhanin, Nucl. Phys. **B875**, 552 (2013).

[244] K. G. Chetyrkin and M. F. Zoller, J. High Energy Phys. 04 (2013) 091; 09 (2013) 155(E).

[245] B. A. Kniehl, A. F. Pikelner, and O. L. Veretin, Nucl. Phys. **B896**, 19 (2015).

[246] S. Alekhin, A. Djouadi, and S. Moch, Phys. Lett. B **716**, 214 (2012).

[247] D. Buttazzo, G. Degrassi, P. P. Giardino, G. F. Giudice, F. Sala, A. Salvio, and A. Strumia, J. High Energy Phys. 12 (2013) 089.

[248] A. V. Bednyakov, B. A. Kniehl, A. F. Pikelner, and O. L. Veretin, Phys. Rev. Lett. **115**, 201802 (2015).

[249] B. A. Kniehl, A. F. Pikelner, and O. L. Veretin, Comput. Phys. Commun. **206**, 84 (2016).

[250] M. R. Whalley, D. Bourilkov, and R. C. Group, arXiv:hep-ph/0508110.